

# **Stony Brook University**



OFFICIAL COPY

**The official electronic file of this thesis or dissertation is maintained by the University Libraries on behalf of The Graduate School at Stony Brook University.**

**© All Rights Reserved by Author.**

**Simultaneous Energy Harvesting and Vibration Control of Tall  
Buildings using Electricity-Generating Tuned Mass Dampers**

A Dissertation Presented

by

**Xiudong Tang**

to

The Graduate School

in Partial Fulfillment of the

Requirements

for the Degree of

**Doctor of Philosophy**

in

**Mechanical Engineering**

Stony Brook University

**May 2013**

**Stony Brook University**

The Graduate School

**Xiudong Tang**

We, the dissertation committee for the above candidate for the  
Doctor of Philosophy degree, hereby recommend  
acceptance of this dissertation.

**Dr. Lei Zuo, – Dissertation Advisor**  
**Assistant Professor, Mechanical Engineering Department, Stony Brook University**

**Dr. Fu-Pen Chiang - Chairperson of Defense**  
**SUNY Distinguished Professor and Chair, Mechanical Engineering Department**  
**Stony Brook University**

**Dr. Jeffrey Ge**  
**Professor and Deputy Chair, Mechanical Engineering Department, Stony Brook University**

**Dr. John M. Kincaid**  
**Professor, Mechanical Engineering Department, Stony Brook University**

**Dr. John Murray**  
**Associate Professor, Department of Electrical & Computer Engineering**  
**Stony Brook University**

This dissertation is accepted by the Graduate School

Charles Taber  
Interim Dean of the Graduate School

Abstract of the Dissertation

**Simultaneous Energy Harvesting and Vibration Control of Tall Buildings using Electricity-  
Generating Tuned Mass Dampers**

by

**Xiudong Tang**

**Doctor of Philosophy**

in

**Mechanical Engineering**

Stony Brook University

**2013**

Abstract: Tall buildings, slender towers and long-span bridges are very susceptible to dynamic load from wind, and consequently vibrations are persistent in these civil structures during daily operation, which are serious concerns to both engineers and architects for the protection of the structure safety and occupant comfort. In order to mitigate the vibration, different approaches have been proposed, among which Tuned Mass Dampers (TMDs) are one of the most preferable and have been widely used in practice. Instead of dissipating the vibration energy into heat waste via the viscous damping element, we proposed an innovative structural vibration control method in this thesis, which can mitigate wind-induced vibrations of large civil structures, and harvest utility-scale energy at the same time by using electricity-generating TMDs. Moreover, several novel configurations TMDs are proposed in this thesis in order to improve the vibration mitigation and energy harvesting performances, namely, electromagnetic shunted TMD, where the auxiliary resonance is introduced by R-L-C circuit instead of mass-spring system; series TMDs, which can reduce the weight of the mass needed by 40-50% and the damping force requirement by 85% compared with classic TMDs, and the electromagnetic shunted series TMDs,

which can realize the effectiveness of series TMD without having large stroke. The parameters of these TMDs are also optimized in this thesis, either analytically or numerically with decentralized control method.

In addition, the dynamics and energy analysis of civil structures with different TMDs are carried out. The available power that can be harvested in typical civil structures is estimated, by the investigating the vibration perception criteria of human beings suggested by International Standard Organization (ISO) and the integrated modeling of wind dynamics and building-TMD systems. Different electromagnetic transducers for converting the vibration energy harvesting into electricity as well controlling the force of vibration mitigation are investigated. The transducers are optimized using finite element analysis for high power density. Besides, prototypes are built and characterized for the practical implementation. In order to harvest energy without harming the vibration mitigation performance, this thesis also investigated and compared several vibration control strategies, namely, semi-active, self-powered active, and passive-matching regenerative along with the relevant electric circuit implementations. The functions of the energy harvesting circuit on damping force control and power regulation, as well as the effectiveness of the control strategies are illustrated by simulation. Finally, a three-story building prototype with electricity-generating TMD composed of a rotational motor and rack-pinion mechanism is built for validation of the simulation results and experimental demonstration of the simultaneous vibration control and energy harvesting.

## Table of Contents

1	Chapter 1 Introduction .....	1
1.1	Background and Motivation .....	1
1.1.1	Energy Harvesting .....	1
1.1.2	Vibrations in Civil Structures .....	3
1.2	Objectives and Contributions of This Thesis .....	6
1.3	Thesis Organization .....	8
2	Chapter 2 Literature Review .....	10
2.1	Reviews of Vibration Mitigation Methods on Civil Structures.....	10
2.1.1	Structural and Aerodynamic Design.....	10
2.1.2	Distributed Dampers .....	11
2.1.3	Classic TMD .....	12
2.1.4	Active TMD .....	14
2.1.5	Semi-active TMD.....	15
2.2	Review of Vibration Energy Harvesting Technologies.....	16
2.2.1	Piezoelectric Transducers .....	17
2.2.2	Electromagnetic Transducers.....	21
2.3	Review on Regenerative Vibration Control .....	26
2.4	Summary.....	28
3	Chapter 3 Power Estimation and Wind Modeling .....	29
3.1	Power Estimation Based on Vibration Perception Criteria by ISO.....	29
3.1.1	Power Estimation .....	29
3.1.2	Economic Analysis .....	33
3.2	Wind Modeling.....	35
3.2.1	Wind Speed Modeling .....	36
3.2.2	Wind Force Modeling.....	37
3.3	Summary.....	39
4	Chapter 4 Optimization of Different TMDs for Vibration Control and Energy Harvesting..	40
4.1	Some Discussions on the Traditional Vibration Energy Harvester.....	40
4.1.1	Harmonic Excitation .....	40
4.1.2	Random Force Excitation .....	46
4.2	Electromagnetic Shunt TMDs .....	49
4.2.1	$H_2$ Optimal Solutions .....	52
4.2.2	$H_\infty$ Optimal Solutions .....	54
4.2.3	A Case Study and Sensitivity Analysis.....	60
4.3	Electricity-Generating TMD.....	63
4.3.1	Electricity-generating TMD.....	63
4.3.2	Parameters Optimization.....	64

4.4	Series TMDs .....	68
4.4.1	Description of Series TMDs .....	68
4.4.2	Review of Parameter Optimization with Decentralized Control Method.....	71
4.4.3	Results of $H_\infty$ Optimal Series TMDs .....	73
4.4.4	Results of $H_2$ Optimal Series TMDs.....	74
4.5	Electromagnetic Series TMDs.....	76
4.5.1	Description and Optimization of Electromagnetic Series TMD.....	76
4.5.2	A Case Study and Sensitivity Analysis.....	79
4.6	Summary.....	84
5	Chapter 5 Design and Optimization of Electroamgnetic Vibration Energy Harvester .....	87
5.1	Tubular Linear Energy Harvester .....	88
5.1.1	Optimization of a Tubular Linear Energy Harvester .....	88
5.1.2	New Configurations and Analysis .....	93
5.1.3	Experimental Characterization.....	96
5.2	Cubic Linear Energy Harvester .....	103
5.2.1	Concept and Design .....	103
5.2.2	Experimental Characterization of Linear Energy Harvesters .....	106
5.3	Harvester Using Rotation Motor and Rack-Pinion Mechanism.....	110
5.4	Summary.....	111
6	Chapter 6 Simultaneous Vibration Control and Energy Harvesting .....	113
6.1	Energy Harvesting Circuit.....	113
6.2	Vibration Control Algorithms .....	114
6.2.1	Active TMD and Series TMD using LQG control design.....	114
6.2.2	Regenerative-Passive .....	117
6.2.3	Semi-active TMD and Series TMD .....	119
6.2.4	Self-powered Active Vibration Control.....	123
6.2.5	Simulation and Experimental Results on a Three-story Building Prototype.....	131
6.3	Summary.....	140
7	Chapter7 Conclusions and Future Work .....	142
7.1	Conclusions .....	142
7.2	Future Work.....	143
	Publications Based On the Dissertations .....	145
	References.....	148

## List of Figures

Figure 1.1 Exponentially increasing research interest on vibration energy harvesting indicated by the numbers of relevant articles in engineering village (EI) and web of science (SCI). However, the majority focuses on micro-scales and obtains power on the order of 10 $\mu$ W-100mW. ....	2
Figure 1.2 Wind induced vibration of Tacoma Narrow Bridge in 1940 (Scott, 2001).....	3
Figure 1.3 Wind induced vibration causes the fall of window glass on Hancock Tower (Schwartz, 2001). ....	4
Figure 1.4 Size comparison of some civil structures with wind turbines. ....	4
Figure 1.5 Typical implementations of TMDs in structures: (a) 660 tons of metal ball (18' diameter) suspended in Taipei 101(Irwin, 2008), (b) 410 tons of concrete block (30'x30'x9') on the top of Citigroup tower( Courtesy of MTS Systems Corporation ). ....	5
Figure 1.6 Problem statement. ....	6
Figure 2.1 Frame without and with passive energy dissipation devices (Symans <i>et al.</i> , 2008). ..	12
Figure 2.2 A building with distributed dampers (fotos courtesy of SIE Corp.).....	12
Figure 2.3 660 metric tons TMD installed on top of Taipei 101. ....	13
Figure 2.4 94 tons TMD installed in the center of White-stone Bridge. ....	13
Figure 2.5 Modeling of buildings different TMDs (a). with passive TMD; (b). with active TMD;(c). with hybrid TMD; (d). with semi-active TMD, regenerative TMD or self-powered active TMD. ....	14
Figure 2.6 Building with active TMD. (a) Kyobashi Siewa Building (b) its active TMD unit (Kareem <i>et al.</i> , 1999).....	15
Figure 2.7 Typical components of a vibration energy harvesting system. ....	17
Figure 2.8 Two modes of piezoelectric materials when used for vibration energy harvesting. ...	18
Figure 2.9 Modeling of piezoelectric materials as energy harvesters: (a) voltage source; (b) current source. ....	19
Figure 2.10 Power generating floor: (a) piezoelectric energy harvesting stacks; (b) experiment in Tokyo Station's Marunouchi North Exit (East Japan Railway Company, 2008). ....	21
Figure 2.11 Linear electromagnetic harvester for regenerative suspensions (Zuo <i>et al.</i> , 2010)...	22
Figure 2.12The eddy current damper for structural vibration control (Palomera-Arias, 2005). ..	22
Figure 2.13 Regenerative backpack, harvesting 7.8 W power from walking, 7.8W (Rome <i>et al.</i> , 2005).....	23
Figure 2.14 Regenerative shock absorber using a ball-screw mechanisms (Kawamoto <i>et al.</i> , 2008).....	24
Figure 2.15 Large structural vibration energy harvester using ball-screw mechanism (Cassidy <i>et al.</i> , 2011). ....	24
Figure 2.16 Regenerative shock absorber using rack-pinion mechanism (Zuo <i>et al.</i> , 2010). ....	25
Figure 2.17 Regenerative shock absorber using motion rectifier. (a), prototype; (b), modeling (Li, <i>et al.</i> , 2012; Li and Zuo, 2013).....	26
Figure 2.18 Implementations of vibration control in vibration energy harvesting system: (a). using clipped control (Tang and Zuo, 2010c); (b) multi-objectives energy harvesting problem (Scruggs <i>et al.</i> , 2011). ....	27



Figure 3.1 Vibration perception criteria of human beings. Peak acceleration suggested by ISO 10137 (solid), RMS acceleration suggested by ISO6897 (dash line), North American practice (red words), and peak acceleration of bridges suggested by ISO 2632-2 (blue line). .....	30
Figure 3.2 Classic TMD.....	30
Figure 3.3 Power dissipated by one of the eight viscous damping devices in the TMD on Taipei 101 in wind-induced vibration (Haskett <i>et al.</i> , 2004). .....	32
Figure 3.4 A typical wind speed distribution in a period of three months measured in Boston area (RERL Wind Data).....	34
Figure 3.5 Peak acceleration of a structure at various wind speed (Denoon and Kwok, 1996). ..	34
Figure 3.6 Performance calculation based on the wind modeling, wind force spectrum and building dynamics. ....	35
Figure 3.7 Power spectrum comparison of simulated and measured wind speed (Ni <i>et al.</i> , 2011). .....	37
Figure 3.8 Mean wind speed and fluctuation along the height of the benchmark building (Ni <i>et al.</i> , 2011). ....	37
Figure 3.9 Normalized spectrum of along-wind fluctuating speed. (Ni <i>et al.</i> , 2011). ....	38
Figure 3.10 Normalized spectrum of across-wind force (Ni <i>et al.</i> , 2011). ....	39
Figure 4.1. Single DOF vibration energy harvester with harmonic force excitation.....	41
Figure 4.2 Dimensionless average harvesting power $P_{ave}$ at different excitation frequency $\alpha = \omega\omega_s$ and electrical damping ratio $\zeta_e$ , where the mechanical damping is $\zeta_m=1\%$ . The peak of $P_{ave}$ is 6.25 at the optimal condition ( $\alpha = 1$ and $\zeta_e = \zeta_m$ ). ....	43
Figure 4.3 Contours of dimensionless average harvesting power $P_{ave}$ at different excitation frequency $\alpha = \omega\omega_1$ and electrical damping ratio $\zeta_e$ , where the mechanical damping is $\zeta_m=1\%$ . (purple dashed curve shows the optimal electrical damping ratio; grey dashed-dot curve shows the optimal excitation frequency at a given electrical damping). ....	43
Figure 4.4 Harvesting power and displacement of the mass at different frequencies, when mechanical damping $\zeta_m=1\%$ . (a). dimensionless power; (b). normalized displacement. (Solid-black: Optimal $\zeta_e$ . dashed-red: $\zeta_e = \zeta_m = 1\%$ ). ....	45
Figure 4.5 Output power performance index at different ratio of $\zeta_e/\zeta_m$ ( $m_s=1$ ). ....	48
Figure 4.6 Frequency response of force to square root of the output power for single-mass vibration energy harvester, where the nominal parameters are, $m_s=1, k_s=1, \zeta_e = 5\%, \zeta_m = 0.5\%$ . (Black solid: nominal $k_s$ ; blue dot: $k_s$ decreased 10 times; red dashed: $k_s$ increased 10 times). ....	48
Figure 4.7 (a) classic TMD, (b) electromagnetic TMD or vibration energy harvester shunted with an $RLC$ circuit, (c) a traditional electromagnetic vibration harvester with an resistive charging circuit. ....	50
Figure 4.8 The frequency responses of the classic TMD of mass ratio 1% and electromagnetic shunt TMD of stiffness ratio 1% . ....	61
Figure 4.9 Sensitivity of vibration suppression of the $H_\infty$ optimal electromagnetic shunt TMD to the parameter changes of the primary systems.....	61
Figure 4.10 Sensitivity of vibration suppression of the $H_\infty$ optimal electromagnetic shunt TMD to the parameter changes of electrical resonant circuit. ....	62
Figure 4.11 Frequency responses of the energy harvesting power of electromagnetic TMD with resonant circuit and with restive load, where stiffness ratio $\mu k = 1\%$ , frequency tuning ratio $f = 0.95$ , damping $\zeta_e = 2\%$ . ....	62
Figure 4.12 (a). classic TMD, (b). electricity-generating TMD. ....	63

Figure 4.13 Three-element TMD.....	66
Figure 4.14 The frequency responses of the building with different TMDs of mass ratio $\mu = 1\%$ . .....	67
Figure 4.15 Sensitivity of vibration suppression of the optimal electricity-generating TMD to the parameter changes. ....	67
Figure 4.16 Building structure with series TMDs when subjected to wind load disturbance (Zuo, 2009).....	69
Figure 4.17 Building structure with parallel TMDs.....	69
Figure 4.18 Frequency responses of $H_2$ optimal series two TMDs with $m_1/(m_1+m_2)=0.909$ (thicker solid) $H_2$ optimal parallel two TMDs (dot) and parallel ten TMDs (thinner solid) $H_2$ optimal 2DOF TMD of (dash) and $H_2$ optimal classic TMD (dash-dot) where the total mass of absorbers is $0.05m_s$ for all the cases, and the primary system has no damping (Zuo, 2009). .....	70
Figure 4.19 Impulse responses of systems with $H_2$ optimal series two TMDs with $m_1/(m_1+m_2)=0.909$ (thicker solid) $H_2$ optimal parallel two TMDs (dot) and parallel ten TMDs (thinner solid) $H_2$ optimal 2DOF TMD of (dash) and $H_2$ optimal classic TMD (dash- dot) where the total mass of absorbers is $0.05m_s$ for all the cases, and the primary system has no damping (Zuo, 2009). ....	71
Figure 4.20 Casting the optimization to control problem (Zuo, 2009). ....	72
Figure 4.21 Frequency responses of structure with series and classic TMDs with parameters optimized by $H_\infty$ control method. ....	74
Figure 4.22 Frequency responses of structures with series and classic TMDs with parameters optimized by $H_2$ control method.....	76
Figure 4.23 (a) Double-mass series TMD, (b) the RMS stroke the double-mass series TMD is several times larger than the classic TMD or parallel TMDs (Ni <i>et al.</i> , 2011).....	76
Figure 4.24 The electromagnetic series TMD. ....	77
Figure 4.25 The modeling of electromagnetic shunt series TMD as a control problem, where the control force $u_1$ is generated by the spring $k_1$ , and the control force $u_2$ is produced by the electrical capacitor $C$ and the resistor $R$ . ....	78
Figure 4.26 The parameter optimization of the mechanical and electrical components in the framework of decentralized control. ....	78
Figure 4.27 The frequency responses of electromagnetic shunt series TMD for Taipei 101 Tower (red solid) in comparison with double-mass TMD (black dash-dot), classic TMD (purple dash), and system without TMD (green dot), where all parameters are optimized to minimize the $H_2$ norm from external force to the displacement of the primary system. ....	81
Figure 4.28 The frequency response of the electromagnetic series TMD optimized for vibration suppression (red solid) and optimized for energy harvesting (blue dash) for Taipei 101 Tower. ....	82
Figure 4.29 The linear power spectrum desntiy of harvested energy in electromagnetic series TMD system optimized for energy harvesting under white-noise force excitation (solid red) and optimized for vibration suppression (blue dash) in comparison with the classic TMD (purple dash-dot) and double-mass series TMD (black dot).....	83
Figure 4.30 Sensitivity of vibration suppression of the electromagnetic shunt series TMD for Taipei 101 to the changes of tuning parameters: stiffness $k_1$ (blue solid), capacitor $C$ (red dash), and electrical load $R$ (green dot) under unit white-noise force excitation $F_{ex}$ . ....	84

Figure 4.31 Sensitivity of energy harvesting of the electromagnetic shunt series TMD for Taipei 101 to the changes of tuning parameters: stiffness $k_1$ (blue solid), capacitor $C$ (red dash), and electrical load $R$ (green dot) under unit white-noise force excitation $F_{ex}$ .	84
Figure 5.1 Diagram of the linear electromagnetic vibration energy harvester.	88
Figure 5.2 Linear energy harvester dimensions and parameters.	89
Figure 5.3 Average value of the absolute magnetic flux density in radial direction $ B_r $ at different magnets thickness $\tau_{ma}$ and coil thickness in radial direction $\tau_{cr}$ , where OD of the harvester is preselected as 63.5mm (2.5 inches).	91
Figure 5.4 Power density at different magnets thickness $\tau_{ma}$ and coil thickness in radial direction $\tau_{cr}$ , where OD of the harvester is preselected as 63.5mm (2.5 inches).	91
Figure 5.5 Coil design: (a) Two phase coil; (b) Three phase coil; (c) Four phase coil.	92
Figure 5.6 Normalized power and number of coils phases.	93
Figure 5.7 The single-layer linear electromagnetic harvester with both axial and radial magnets.	94
Figure 5.8 The double-layer linear electromagnetic harvester: (a) overview; (b) with axial magnets and steel spacers; (c) with both axial and radial magnets.	94
Figure 5.9 FEA result of different configurations: (a) single layer with axial magnets, (b) single-layer with axial and radial magnets, (c) double-layer with axial magnets, (d) double-layer with axial and radial magnets.	95
Figure 5.10 Magnetic flux density (a) along the center line of air gap, (b) along the radial direction inside of the coil.	96
Figure 5.11 Linear energy harvester prototypes: (a) without steel casing (b) with steel casing.	97
Figure 5.12 Magnetic flux density measurement of the prototypes.	97
Figure 5.13 Experiment setup.	98
Figure 5.14 Model of the experiment set up.	98
Figure 5.15 Voltages and force generated when LET is open-circuit under 10HZ harmonic excitation of 2.54mm peak-to-peak amplitude.	99
Figure 5.16 Voltages and force generated when LET is shunt with 40 $\Omega$ electric load, under 10HZ harmonic force excitation of 2.54mm peak-to-peak amplitude.	99
Figure 5.17 Instant power when linear harvester is shunt with 40 $\Omega$ electric load.	100
Figure 5.18 Harvester with steel casing under 10Hz harmonic excitation with different amplitude: (a) RMS voltage; (b). RMS power.	101
Figure 5.19 Damping loop under harmonic excitation with different external resistors, namely open circuit (green curve), 100 $\Omega$ (red curve), 40 $\Omega$ (purple curve), 10 $\Omega$ (blue curve) and short circuit (black curve): (a)10HZ without casing, (b)10HZ with casing.	102
Figure 5.20 Design of a new type of electromagnetic vibration harvester: (a) assembly of coil array, (b) assembly of magnets, (c) top view of whole vibration energy harvester.	103
Figure 5.21 Finite element analysis of magnetic field, (a) Top view of magnetic flux loops. (b) Magnetic flux density $B_p$ distributed on the coil plate.	104
Figure 5.22 The coils are designed to follow the main eddy current loops.	106
Figure 5.23 Dimensions of the coil and magnets.	106
Figure 5.24 Measured (solid) and calculated (dashed) magnetic flux density $B_p$ along the center of the coil plate in the horizontal and vertical directions.	107
Figure 5.25 Time response of the vibration energy harvester under 10Hz excitation.	107
Figure 5.26 RMS voltage under 10Hz harmonic excitation with different amplitudes.	108

Figure 5.27 Damping loop under harmonic excitation with different external resistor, namely open circuit (green curve), 200 $\Omega$ (red curve), 70 $\Omega$ (purple curve), 20 $\Omega$ (blue curve) and short circuit (black curve): (a)5Hz, (b)10Hz, (b)15Hz.....	109
Figure 5.28 Copper plate of the eddy current damper.....	110
Figure 5.29 Damping loop under 5Hz harmonic excitation.....	110
Figure 5.30 regenerative TMD using a rotational brushed DC motor and rack-pinion mechanism.....	111
Figure 6.1 Typical power electronic circuit in vibration energy harvesting.....	114
Figure 6.2 Active series TMDs and active classic TMD.....	115
Figure 6.3 Frequency responses of structures with active series TMDs and active classic TMD.....	117
Figure 6.4 Force requirements of active TMD and series TMDs in the frequency domain to achieve comparable vibration suppressions.....	117
Figure 6.5 Block diagram of the semi-active series TMDs and classic TMD.....	120
Figure 6.6 Frequency responses of structures with semi-active series TMDs and classic TMD.....	120
Figure 6.7 Energy harvesting circuit with both vibration damping force control and power regulation capabilities.....	121
Figure 6.8 Feasible force region.....	122
Figure 6.9 Modified energy harvesting circuit with self-powered active control capability.....	123
Figure 6.10 Schematic of the self-powered active TMD system.....	123
Figure 6.11 Energy harvesting mode ( $e_m > 0$ ).....	124
Figure 6.12 Energy harvesting mode ( $e_m < 0$ ).....	125
Figure 6.13 Driving mode ( $f_m > 0$ ).....	126
Figure 6.14 Driving mode ( $f_m < 0$ ).....	126
Figure 6.15 Passive mode.....	127
Figure 6.16 Transient acceleration response under random excitation.....	128
Figure 6.17 Transient force response under random excitation. (Passive mode is a small segment marked in the harvesting mode in this figure when the relative velocity $ v_r $ is less than $Mk_e V_{Bi}/R_m$ .).....	129
Figure 6.18 Transient response under harmonic excitation.....	130
Figure 6.19 Frequency responses of transmissibility ratio.....	130
Figure 6.20 Power and energy transient response. The ideal case is the one doesn't consider the any power loss, while the practical take the efficiency of both harvesting and driving circuit into account.....	131
Figure 6.21 A 3-story building prototype with regenerative TMD: a), the whole view of the building; b), the 3-D drawing of the regenerative TMD, c), a close-up view of the TMD prototype.....	132
Figure 6.22 Measured frequency response of the 3-story building prototype without TMD.....	132
Figure 6.23 Current flow of the electromagnetic motor at different duty cycles.....	134
Figure 6.24. Power harvested by the motor (thinner lines) and stored in the battery (thicker lines) at different duty cycles.....	134
Figure 6.25 Efficiency of the energy harvesting circuit at different duty cycles.....	135
Figure 6.26 Frequency response of passive, electricity-generating and active TMDs.....	136
Figure 6.27 Power harvested by the motor in different control strategies.....	136
Figure 6.28 Measured frequency response of the prototype building.....	137

Figure 6.29 Measured instant electrical current that flows through the diode D1 to charge the battery.....	138
Figure 6.30 Measured transient acceleration response of the building. ....	139
Figure 6.31 Measured voltage on the $360\Omega$ resistor generated by the electromagnetic TMD... ..	139
Figure 6.32 Measured transient average current $i$ that charges the battery of the energy-generating TMD controlled by duty cycle. ....	140

## List of Tables

Table 3.1 Estimated harvestable energy in some structures using the existing TMDs.....	32
Table 3.2 Cost Estimation on the retrofit of the TMD in Taipei 101. ....	34
Table 4.1 Optimum parameters for vibration mitigation.....	60
Table 4.2 Optimal parameters with $H_2$ optimization for different TMDs. ....	68
Table 4.3 Parameters and performances of $H_\infty$ optimal TMDs.....	74
Table 4.4 Parameters and performances of $H_2$ optimal TMDs. ....	75
Table 4.5 Parameters of Taipei 101 tower and the $H_2$ optimal classic and double-mass series TMDs. ....	80
Table 4.6 Performances of optimal electromagnetic shunt series TMD in comparison with classic and double-mass series TMDs for Taipei 101* under unit white-noise force excitation $F_{ex}$ . ....	81
Table 4.7 Optimal parameters and performances of electromagnetic shunted series TMDs optimized for vibration control and for energy harvesting under unit white-noise excitation $F_{ex}$ . ....	82
Table 4.8 Optimal parameters of different TMD for vibration mitigation. ....	85
Table 5.1 Absolute value of average radial magnetic flux density $ B_r $ , power density and damping density in different configurations. ....	95
Table 5.2 Experiment result of linear energy harvesters under 10Hz excitation.....	100
Table 5.3 Damping achieved and with different external electrical load. ....	102
Table 5.4 Damping achieved and power harvested with different external restive load.....	109
Table 6.1 RMS acceleration of the building under random wind load excitation with the power spectral density of $S_0=4.0 \times 10^{14} \text{ N}^2\text{s}$ .....	128
Table 6.2 Parameters used for simulation.....	133

## Acknowledgments

I would like to express my sincere gratitude to everyone who has helped and supported me in this endeavor. Without them, I would not be able to accomplish this work.

First of all, I would like to give thanks to my advisor, Professor Zuo. It is my luck to have Professor Zuo as my advisor. He has been giving me valuable instructions and guidance, which helps me tremendously in the process of this project. His talent and encouragement amazed me and drove me to convey my enthusiasm to work on the project. His creativity and his attitude to work have influenced on my work and life as well.

I also would like to thank Professor Chiang, Professor Ge, Professor Kincaid and Professor Murray for serving on my thesis committee. Their comments, ideas and suggestions have been very insightful for my research and significantly improved the quality of my thesis.

I also gratefully acknowledge the funding support from National Science Foundation (NSF) CMMI#1031038 and New York State Energy Research and Development Authority (NYSERDA) through contract #15761.

Next, I propose my appreciation to my lab mates, Teng, Tao, Wanlu, Gopi, Peisheng, Minwei, Yilun, Wen and Jinwoo for providing help and encouragement, and my friends for their moral support. Especially, thanks to Teng Lin and Tao for their helps on making the linear energy harvester and wind modeling.

I would also like to give my deepest thanks to my family, especially my wife, Waiman Cheng. Their support and devotion make my life easier and better.

# **Chapter 1**

## **Introduction**

In this chapter, the background and motivation of this thesis will be introduced. The objectives as well as the contributions of this thesis will be presented. The thesis organization is also outlined at the end of this chapter.

### **2.1 Background and Motivation**

#### **2.1.1 Energy Harvesting**

With the global energy crisis and environment concerns, many technologies in energy harvesting have been developed. The solar, wind, geothermal and hydraulic power plants or farms are such examples. Green structures are also a growing and exciting trend around the world. For example, solar cell tiles have replaced the aged mosaic tiles in the 387 feet CIS Tower in Manchester, UK, and are feeding the electricity grid at an average rate of 21 KW since November 2005 (CIS “Solar Tower” Case Study, 2013). Three 29 feet 225KW wind turbines have already started to work since April 2008 on the bridge connections of the 787 feet Bahrain WTC twin towers in Kingdom of Bahrain (Bahrain World Trade Center, 2013). Solar panels and three 29 feet wind turbines will be installed in the 1312 feet Dubai’s Lighthouse (United Arab Emirates), which will reduce the energy consumption by 65% (DIFC, 2013).



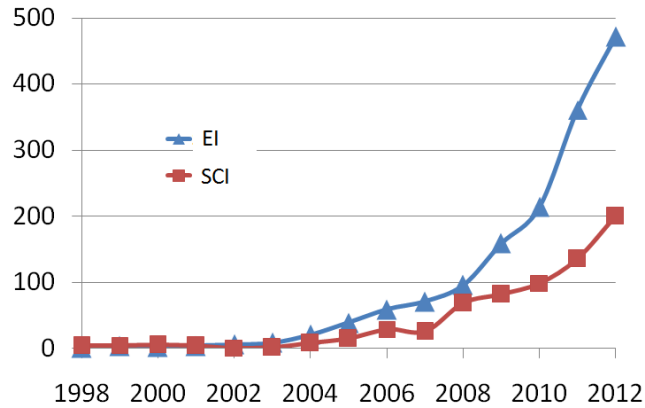


Figure 2.1 Exponentially increasing research interest on vibration energy harvesting indicated by the numbers of relevant articles in engineering village (EI) and web of science (SCI). However, the majority focuses on micro-scales and obtains power on the order of  $10\mu\text{W}$ - $100\text{mW}$ .

Meanwhile, the vibration is becoming a good alternative energy source and receives increasingly attention in recent years, since it exists everywhere, such as vibration of floors and walls, machines, pumps, vehicle chassis, railway train or tracks, human motions, and *etc.* The research has resulted in a wealth of literature and some promising applications such as low-power electronics and self-powered wireless sensors (Chalasan and Conrad, 2008). Hundreds of articles have appeared in the past six years (Figure 1.1), including over ten review articles, such as (Sodano and Inman, 2004; Collins, 2006; Galhardi *et al.*, 2008; Paradiso and Starner, 2005; Park *et al.*, 2008; Saadon and Sidek 2011; Kim *et al.*, 2011). So far, the review articles and the majorities of the research on vibration energy harvesting focus on the small scale ( $<100\text{mW}$ ). In real world, the vibrations can be very large, for example, the vibrations of buildings or bridges, vehicle systems, even human motions. Harvesting large amount of vibration energy promises more meaningful applications. Though relative few, there are still some interesting initiatives in the research laboratories and industry on harvesting vibration energy on the order of Watts or even more. Recently two articles in Science by Rome *et al.* (2005) and Donelan *et al.* (2008) showed that 5-7 Watts of vibration power can be harvested from walking using geared electromagnetic motors. In early 2008, a power-generating floor composed of piezoelectric arrays has been tested at a subway station in Tokyo (East Japan Railway Company, 2008), which was able to harvest 2.8 Watt-hour energy per day. Some researchers have looked into the energy harvesting in vehicle suspensions, and 10-90 Watts of vibration energy harvesting has been

demonstrated (Nakano *et al.*, 2003; Gupta *et al.*, 2006; Kawamoto *et al.*, 2007 and 2008; Zuo *et al.*, 2011; Li, *et al.*, 2012).

### 2.1.2 Vibrations in Civil Structures

In the other hand, vibration has been a serious concern since the early days when tall buildings were built for the first time. These civil structures are subjected to huge dynamic loadings from winds, earthquakes, water waves, traffics, human motions and *etc.* Large vibration amplitudes can damage the structures or the secondary components, and cause discomfort to its human occupants, whose symptoms range from anxiety, fear to dizziness, headaches, and nausea (Kareem *et al.*, 1999). For example, the Tacoma Narrow Bridge collapsed due to wind-induced vibration four months after its opening in 1940 (Scott, 2001), as shown in Figure 1.2. In 1972 wind-induced vibration also caused more than 65 panels of window glass, weighing 500 pounds each, to fall and crash on the sidewalks hundreds of feet below the Hancock Tower in Boston (Schwartz, 2001). Figure 1.3 shows the picture taken after the incident where the missing glasses can be clearly seen. After so many catastrophic incidents with huge economic loss, property damage, and even loss of human lives, vibration and the associated wind engineering became essential for the design and analysis of these structures. It has been noted that in many of the structural designs the local load is governed by the seismic stress and the overall motion is governed by the wind load (Kareem *et al.*, 1999). Figure 1.4 compares the sizes of some tall buildings with 100KW-1.5MW wind turbines, which can give us a sense on how large the force and wind power are acting on the tall buildings.

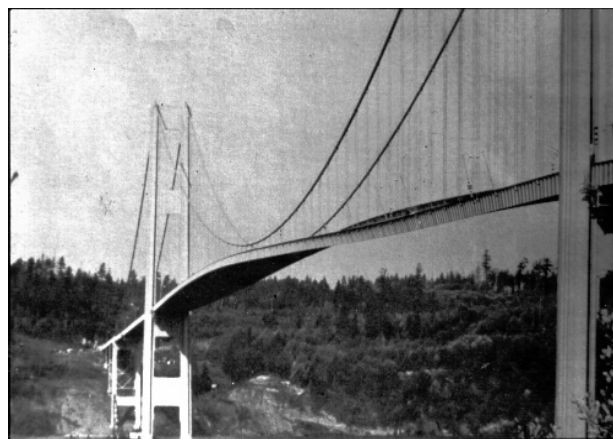


Figure 2.2 Wind induced vibration of Tacoma Narrow Bridge in 1940 (Scott, 2001).



Figure 2.3 Wind induced vibration causes the fall of window glass on Hancock Tower (Schwartz, 2001).

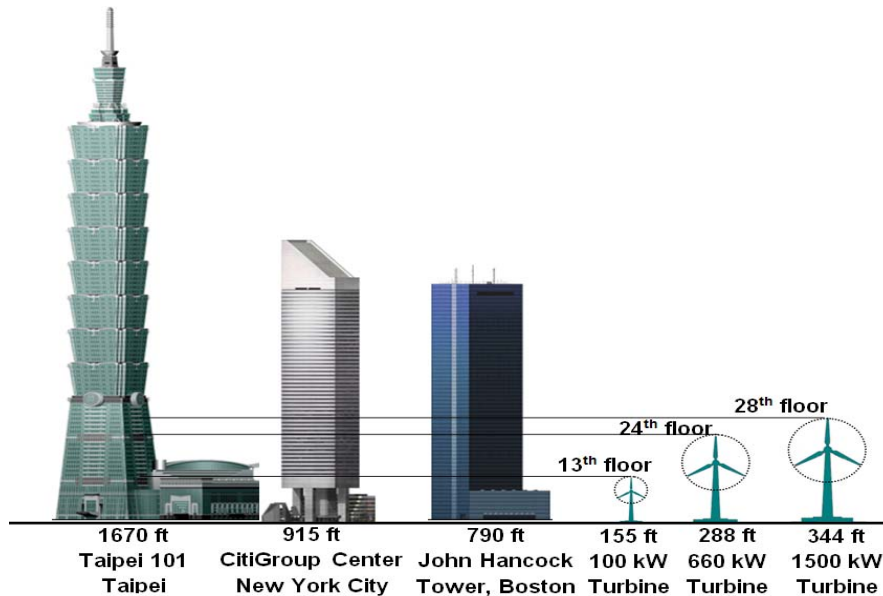


Figure 2.4 Size comparison of some civil structures with wind turbines.

With the race towards new height of the buildings and new length of long-span bridges, vibration control becomes more important and challenging. Details of the structure vibration suppression can be seen in the comprehensive reviews by Soong and Spencer (2002), Kareem *et al.* (1999), Housner *et al.* (1997), and many others (Spencer and Sain, 1997; Tanaka *et al.*, 2003). Generally speaking, there are three types of vibration suppression methods: structure design (Ali and Moon, 2007), vibration isolation (Morgan and Mahin, 2006), and vibration damping. Modern buildings are constructed with steel or concrete, which have very low inherent damping. Typically the damping ratios are 0.5%-1% and the vibration amplitude at the resonant frequency can be 50-100

times larger than the static deformation (quality factor is 50-100). Hence, supplemental damping becomes the most important strategy to control the vibration. The damping devices include viscous fluid dampers, viscoelastic dampers, metallic yield dissipaters, friction dampers, and tuned mass damper (TMDs). Among all these energy dissipaters, the TMD and its variants (tuned liquid damper, *etc.*) become increasingly popular and compose the greatest percentage of the supplemental damping systems currently in use (Kareem *et al.*, 1999; Soong and Spencer, 2002; Housner *et al.*, 1997).

The TMD, which is composed of a mass up to several hundreds or thousand tons connected to the civil structure with spring and viscous dissipative devices, has been installed in many buildings around the world, for example, Citigroup Tower in New York (410 tons TMD, installed in 1978), John Hancock Tower in Boston(600 tons TMD, 1977), Trump World Tower in New York (600 tons, 2001), Chicago Spire 10 (1300 tons, in construction), Taipei 101 Tower (660 tons, 2004), Crystal Tower in Japan (540 tons, 1990), Chifley Tower in Sydney(400 tons, 1993), Bronx-Whitestone Bridge in New York (94 tons, 1988), and many others (Kwok and Samali, 1995; Sun *et al.*, 1995). These TMDs can reduce the vibration response of the structures by 40%-60% via energy dissipation. They are typically either suspended with pendulums (including multi-stage pendulums or inverted pendulums) or supported by bearings (mechanical, hydraulic, or rubber) with mechanical guides on the top of the roof or the top floor. Figure 1.5 shows such two typical implementations in practice.

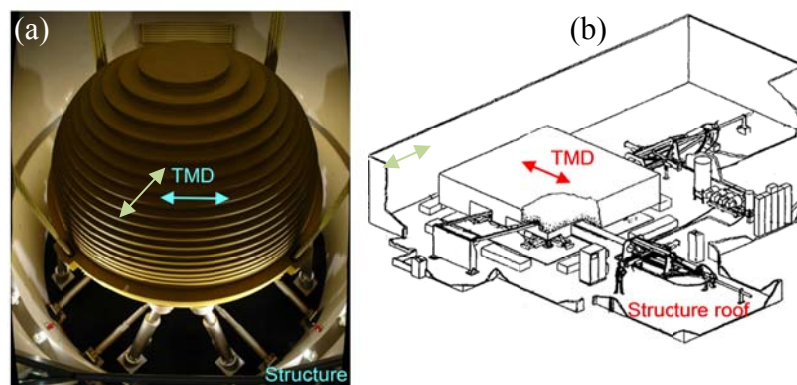


Figure 2.5 Typical implementations of TMDs in structures: (a) 660 tons of metal ball (18' diameter) suspended in Taipei 101(Irwin, 2008), (b) 410 tons of concrete block (30'x30'x9') on the top of Citigroup tower( Courtesy of MTS Systems Corporation ).

## 2.2 Objectives and Contributions of This Thesis

Traditionally, the vibration energy of the civil structures is dissipated into heat waste by the supplemental damping, and the energy dissipation rate is so large that sometimes forced liquid cooling or a heat resistant design must be utilized. An interesting question is raised: can we mitigate the vibration by converting the vibration energy into useful electricity? The problem statement can be illustrated by Figure 1.6. Throughout the literature search in 2008, I found that all the current vibration energy harvesting researches focus only on small scales, which have successful but very limited applications such as wireless sensors (Paradiso and Starner, 2005) and structure health monitoring (Park *et al.*, 2008). Some researchers (Nakano *et al.*, 2003; Gupta *et al.*, 2006; Kawamoto *et al.*, 2007 and 2008), have looked into energy harvesting from vehicle vibration and obtained tens of Watt, which is already considered to be very “large”.

Figure 2.6 Problem statement.

As a consequence, several critical questions, among others, remain unanswered:

- 1) Can we harvest the vibration energy and mitigate the vibration at the same time?
- 2) If possible, how much power is actually available for harvesting? How do we efficiently harvest the structure vibration energy? The vibration frequency of large structures is very low (0.1-0.5Hz), and the efficiency of the harvesters is particularly challenging.
- 3) Can we effectively and robustly control the structure vibration with by proposing TMDs with new configurations and small-mass?
- 4) How can we take advantage of the harvested power for better vibration control?

Hence, the overall objective of the thesis is to establish an innovative structural vibration control technology to effectively mitigate wind-induced vibrations of civil structures, and at the same time efficiently harvest large-scale vibration energy using electricity-generating TMDs. Specifically, I proposed to use the existing TMDs or series TMDs and electromagnetic transducers as the vibration control and energy harvesting devices, to enhance the power efficiency by optimizing the electromagnetic transducers and new power electronics, and to achieve better vibration suppression by utilizing and optimizing new configurations of TMDs, self-powered active, semi-active vibration control and passive-matching regenerative algorithms. Instead of dissipating the vibration energy into heat waste in the traditional way, the proposed research in this thesis will convert the vibration energy into electricity, and use it for better vibration control or feed the energy into the power grid. The analysis shows that the harvestable vibration energy from certain skyscraper is up to 10-300 KW, which mean that this technology can lead to the first industrial-scale wind turbines without wind blades.

The detail research accomplished in this thesis includes:

- 1) Dynamics and modeling of structures with classic TMD, series TMD, electromagnetic shunted TMD and electromagnetic shunted series TMD, which includes the modeling of wind and structures. Additionally, a mathematical model is created to analyze the vibration dynamics and assess kinetic vibration energy of building under dynamic wind loading with different TMDs. Besides, the newly proposed electromagnetic shunted TMD and electromagnetic shunted series TMD, where the resonant is introduced by R-L-C resonant circuit were optimized for both vibration mitigation and energy harvesting.
- 2) Designed and optimized electromagnetic transducers with high power density using electromagnetic finite element analysis. The electromagnetic transducers are also characterized to in order to analyze the effect on the structural dynamics.
- 3) Developed advanced vibration control algorithms, which include semi-active vibration control with controllable damping, self-powered active vibration control, passive-matching regenerative algorithms and the corresponding implementation with energy harvesting circuits.

- 4) System integration and demonstration. A three-story building prototype with regenerative TMD is developed and the simultaneous vibration control and energy harvesting is demonstrated experimentally.

The research in this thesis has several scientific merits. (1). the research is interdisciplinary since it blends concepts of mechanical engineering and structural engineering with power system and electrical engineering concepts. It will bridge several disparate areas and create new knowledge in the interdisciplinary area. (2). it has the potential to revolutionize the approach of structural vibration mitigation from energy dissipation to electricity generation. Energy dissipation, including TMDs and other vibration damping devices, has been the dominant method to mitigate structural vibration in the past half century. The electricity-generating TMDs will pave an innovative way for vibration control without external power source, thus increase the safety, reliability, and self-sustainability of the structures. The novel configuration and implementation of series TMDs can reduce the mass requirement of the TMD by 40-50%, decrease the force requirement by 85%, and significantly increase the effectiveness and robustness. (3). the research in this thesis will also advance the vibration energy harvesting technology by an order of 1000, for the first time, to 50-100KW, creating a meaningful approach to alternative, sustainable, and eco-friendly energy. Energy harvesting from vibration was explored ten years ago, and has attracted significant attention recently. The results of the thesis will lead to the first industrial-scale green energy generator from wind-induced vibration, and thus enable many practical applications like self-sustainable actuation, sensing, and structural health monitoring.

## **2.3 Thesis Organization**

Chapter 2 reviews the current civil structures vibration mitigation technology, as well as some relevant work on vibration energy harvesting and regenerative vibration control. In Chapter 3, the power that is available for harvesting in different civil structures is estimated. The impacts on economics and environment are also discussed. The performance of different TMDs for vibration control and energy harvesting are investigated in Chapter 4, as well as the parameter optimization of proposed electromagnetic TMD, series TMD and electromagnetic TMD using analytical and decentralized control method. Chapter 5 presents the design and optimization of the vibration energy harvesters, where two types of vibration energy harvesters are developed and compared. The harvesters are also characterized experimentally in order to analyze the effect

on the structural dynamics. Chapter 6 presents the regenerative vibration control methods of civil structures using electricity-generating TMDs, where different vibration control algorithms and energy harvesting circuits are proposed and investigated. Finally, Chapter 7 draws the conclusions and points out the future research direction.



## **Chapter 2**

### **Literature Review**

In this chapter, different methods on mitigating the vibration of civil structures as well as technologies on vibration energy harvesting are reviewed. In addition, the current research on regenerative vibration control is also summarized in this chapter. The review of the vibration mitigation technology focuses more on the method using TMDs.

#### **3.1 Reviews of Vibration Mitigation Methods on Civil Structures**

Large civil structures such as tall buildings, long-span bridges, and tall towers are very susceptible to the dynamic loadings of wind, earthquake, traffic, and human motions, thus large vibration exists in these civil structures. Many methods have been developed to mitigate the vibrations in order to keep the structure safety and occupant comfort, ranging from structural and aerodynamics design to the utilization auxiliary damping devices. In this chapter, I will review several different methods on mitigating the wind-induced vibrations of civil structures.

##### **3.1.1 Structural and Aerodynamic Design**

Structural design is a passive method to mitigate the wind induced vibration. There are two ways to implement this method, namely, by increasing the building mass to reduce air/building mass ratio, and by increasing stiffness or natural frequency to reduce non-dimensional wind speed

(Kareem *et al.*, 1999). These two implementations are actually correlated. Increasing the building mass will also decrease the natural frequency. However, it is not always realistic to increase the building mass in practice, because it will result in amplification of the seismic inertia force, which means it is good for mitigating wind-induced vibration, but not optimal for reducing vibration induced by seismic motion (Kareem *et al.*, 1999). Besides, increasing the building mass will incur more material costs. However, the appropriate selection of an efficient structural system can still provide an effective way to reduce the structural vibration.

Aerodynamic design is also a passive method to mitigate the wind induced vibration, which improves aerodynamic properties of the civil structures to reduce wind force coefficient. The wind-induced vibration is essentially caused by the interaction between the wind and building surface. Therefore the shape of the building surface plays significant role in the wind-induced vibration. The aerodynamic modifications of a building's cross-sectional shape or the variation of its cross-section can reduce building's vibration. It has also been observed that the openings, especially near the top of tall buildings can significantly reduce the vortex shedding-induced forces, hence the crosswind dynamic response and vibration of the buildings (Dutton and Isyumov, 1990). However, careful studies, including simulation and wind-tunnel test must be conducted in order to modify the aerodynamic design of civil structures and avoid adverse effects.

### **3.1.2 Distributed Dampers**

Installing passive distributed dampers in the frame of the tall buildings is also a popular method to dissipate the vibration energy into heat waste, hence reduce the wind-induced or seismic motion induced vibration of the tall buildings, the simple illustration of the methodology is shown in Figure 2.1. Figure 2.2 shows one example of building with distributed dampers installed (Wallace F. Bennett Federal Building). As pointed by Symans *et al.*, (2008), the introduction of these distributed energy dissipation devices into the frame of the tall buildings will also result many analysis and design issues that must be consider by the engineers, because the behavior of the dampers will influent the performance of the structures to which it is attached. More detailed information of the state-of-art can be found by the extensive review paper written by Symans *et al.*, (2008).

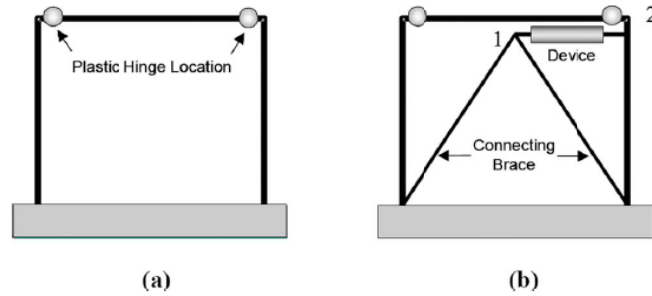


Figure 3.1 Frame without and with passive energy dissipation devices (Symans *et al.*, 2008).

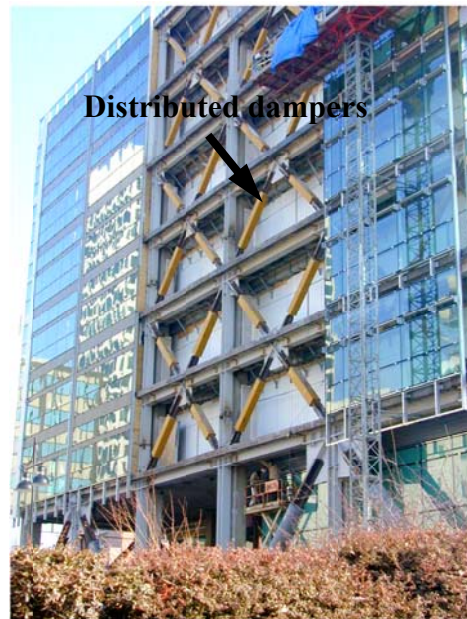


Figure 3.2 A building with distributed dampers (Photos courtesy of SIE Corp.).

### 3.1.3 Classic TMD

Tuned mass damper (TMD) has been widely used in practice as discussed in Chapter 1. The original TMD, which was invented by Frahm (1911), only consists of an auxiliary mass and a spring connected to the primary system to mitigate vibration in a very narrow frequency range near the resonance. Den Hartog (1947) increased the working frequency range by introducing an additional energy dissipating element and optimizing the parameters. It is usually installed at the location with maximum motion, generally near the top of the building or in the center of long-span of bridge. For example, Figure 2.3 shows the passive TMD installed on the top of Taipei 101 and Figure 2.4 shows the passive TMD installed in the center of White-Stone Bridges. Since over 90% of the vibration energy is contributed by the first vibration mode (Ni *et al.*, 2011), a

reasonable assumption can be made that all the mode higher than one can be neglected when modeling. Hence, the building with passive TMD can be simply modeled as a two degree-of-freedom (DOF) system as shown in Figure 2.5 (a).

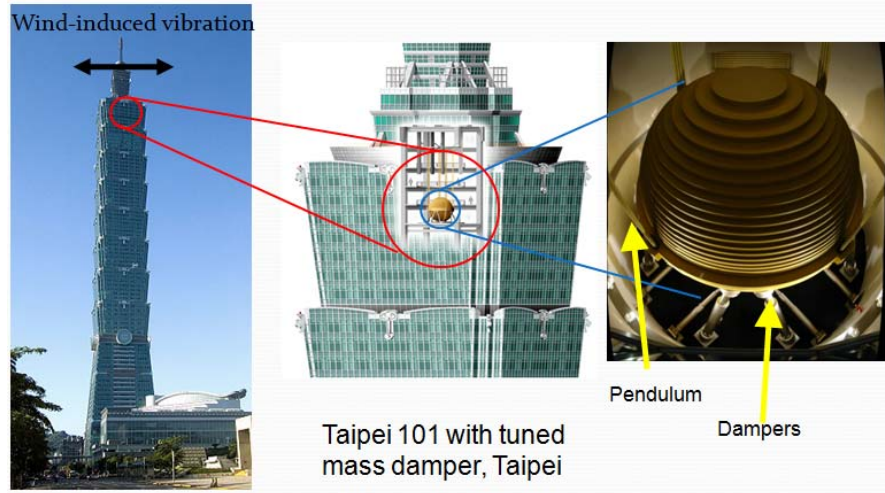


Figure 3.3 660 metric tons TMD installed on top of Taipei 101.



Figure 3.4 94 tons TMD installed in the center of White-stone Bridge.

A major concern of TMDs in structural vibration mitigation is their robustness: when the parameters of the primary structures change by a small amount, the performance of TMDs will be greatly defected. For example, if the stiffness or mass is differed by 10%, the frequency peak can increase by 50%. It is so called off-tuning problem, which has been investigated by researchers (Kerschen *et al.*, 2007; Setareh *et al.*, 2006). Another shortcoming is that the effectiveness is limited by the mass ratio, and many TMDs weight several hundred tons. For

comparison, the weight of TMDs in New York Citigroup, Taipei 101, and Chicago Spire towers are as much as that of 300-900 cars. Such huge mass requires large space in buildings and costs millions of dollars to construct.

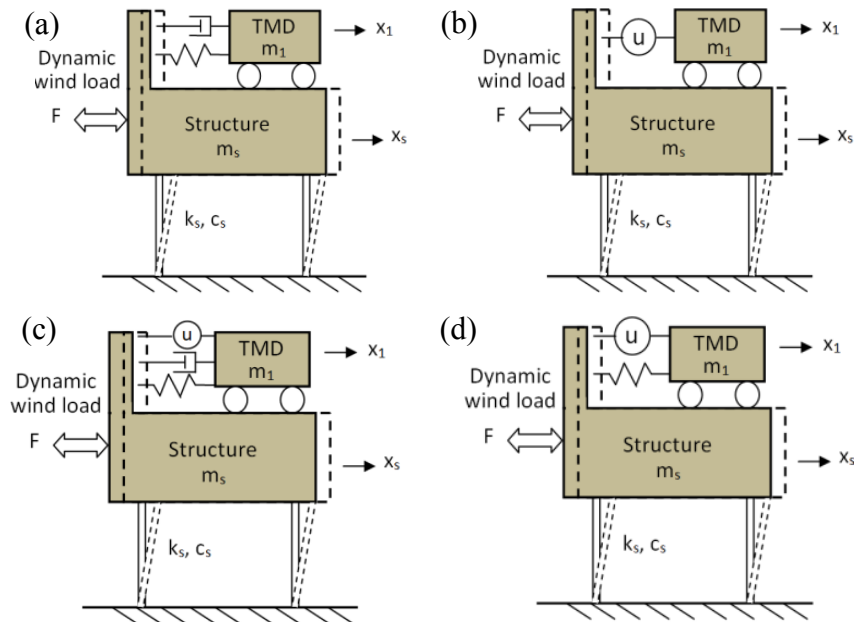


Figure 3.5 Modeling of buildings different TMDs (a). with passive TMD; (b). with active TMD;(c). with hybrid TMD; (d). with semi-active TMD, regenerative TMD or self-powered active TMD.

### 3.1.4 Active TMD

To further mitigate the vibration, TMDs using active control have been proposed by researchers, where actuators are installed between the seismic mass and structure to provide active force, as shown in Figure 2.5(b). Active TMDs were first successfully implemented in an 11-story building by Kajima Corp (Japan) 20 years ago (Koshika *et al.*, 1992), as shown in Figure 2.6. The active TMD can mitigate the vibration both induced by earthquakes and strong winds, and it has been proven that the active TMDs can provide better vibration mitigation performance than the passive ones, at the cost of large amount energy consumption (Koshika *et al.*, 1992). Reliable power source is a serious concern, especially in hazards when the accessibility to external power cannot be guaranteed. Active TMDs also require very large actuation force, for example, the active TMD installed in Applause Tower in Japan (1992) needs two hydraulic actuators of five

tons of thrust (Higashin and Aizawa, 1993). The requirements of large actuation forces and reliable power source are the reasons why no active TMDs are in full-scale implementation in the USA. Therefore, more effective, robust, smaller-bulk, and powerless strategies are of the most interest for structural vibration control. Hybrid active TMD is composed of passive TMD and one additional actuator in parallel with the damping element. The modeling of it is shown in Figure 2.5 (c). It can reduce the power consumption and increase the robustness in the event of power failure (Fujino *et al.*, 1996; Tomoo and Keiji, 1998). They have been installed in several buildings since 1993 with reduced energy requirements and increased reliability, for example, Nishikicho Building (Fujino *et al.*, 1996), Hotel Ocean (Tomoo and Keiji, 1998), *etc.*



Figure 3.6 Building with active TMD. (a) Kyobashi Siewa Building (b) its active TMD unit (Kareem *et al.*, 1999)

### 3.1.5 Semi-active TMD

Realizing both the limitations of passive and active TMDs, researchers proposed semi-active TMDs to provide better vibration mitigation performance than the passive one without requiring large external power source for active TMDs. The viscous damping element is replaced with Magneto Rheological (MR) or variable orifice dampers, as shown in Figure 2.5 (d). Semi-active control has been investigated in vibration control of buildings with TMDs (Hrovat *et al.*, 1983; Dyke *et al.*, 1996; Pinkaew and Fujino, 2001; Lewandowski and Grazymislawska, 2003; Chey *et al.*, 2010) and vehicle suspension systems (Karnopp, 1995; Savaresi *et al.*, 2010).

The two main types of semi-active dampers used in the structural vibration control are variable orifice dampers and MR dampers. The variable orifice dampers usually have solenoid-valve which controls the size of the effective orifice thus changes the damping coefficient the dampers can provide. Variable orifice dampers can provide high speed and accurate flow control.

MR dampers use the property of MR fluid to achieve variable damping. When the magnetic fields are applied, their behavior changes from that of a low-viscosity fluid to more of a semi-solid, visco-plastic behavior. The particles in MR fluid are free to move in unmagnified state. However, they are quickly aligned in certain geometry when the magnetic field is applied, thus the fluid becomes more viscous and higher damping force achieved. The viscosity of fluid depends on the applied magnetic fields. The stronger the magnetic field is applied, the higher the viscosity the fluid has. Moreover, the magnetic field is adjusted by the current. Therefore, the reaction time for adjusting different damping force becomes significantly short which is on the order of millisecond. It should be noted that controlling the semi-active damper does not consume significant power, which is one of the significant advantages of semi-active dampers.

However, considering that the semi-active control force is essentially a passive force, meaning that the vibration energy is being dissipated through the devices. Instead of being dissipated into heat waste, the energy can be converted into electricity through electromagnetic transducers, resulting regenerative semi-active TMDs, which can also be modeled as a two DOF in Figure 2.5(d). The semi-active control algorithms will be implemented with energy harvesting function using electromagnetic transducers in this thesis.

### **3.2 Review of Vibration Energy Harvesting Technologies**

A typical vibration energy harvesting system consists of a mechanical system excited by external force, or motion; a transducer which converts the vibration energy into electric energy; mechanisms for the purpose of motion transmission and magnification; power electronic circuits and energy storage elements; energy management and control strategies, as shown in Figure 2.7. Traditionally, the vibration energy is dissipated into heat waste by the damping elements of the systems. Rather than dissipating the vibration energy into heat waste by the damping elements, the transducers in vibration energy harvesting system can convert the mechanical energy into electric energy. Various transducers have been investigated for the vibration energy harvesting,

including piezoelectric materials (Sodano and Inman, 2004; Galhardi *et al.*, 2008; Saadon and Sidek 2011; Kim *et al.*, 2011), linear and rotation electromagnetic motors (Rome *et al.*, 2005), electrostatic generators (Mitcheson *et al.*, 2004), and dielectric generators (Kornbluh *et al.*, 2002). Among these transducers, the piezoelectric materials and electromagnetic machines have more potential for large-scale vibration energy harvesting. In some situations where the vibration mitigation of the primary structure is concerned, piezoelectric materials and electromagnetic motors can also serve as actuators simultaneously for the purpose of active or regenerative vibration control, thus the power flow is bidirectional, as shown in Figure 2.7.

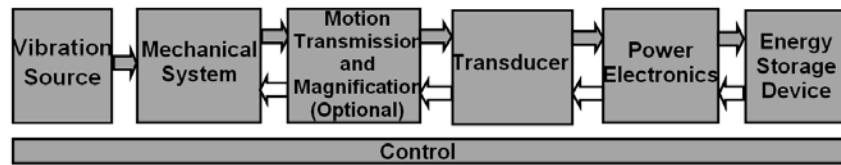


Figure 3.7 Typical components of a vibration energy harvesting system.

Although piezoelectric materials and electromagnetic motors have both been used in vibration energy harvesting, they have different features. Piezoelectric material is a force or stress induced transducer, while electromagnetic motor is a velocity induced transducer. Hence, piezoelectric material is more suitable for vibration with large force and small deformation (due to limited strain range). Electromagnetic motor is preferred in situations where vibration has large velocity or amplitude. So far, electromagnetic motors have been found more often as the transducers for large scale energy harvesting. They have been used to harvest energy from vehicle suspension and buildings. On the other hand, piezoelectric materials have larger energy density (Chen *et al.*, 2006) and are more suitable for the applications where the space or weight is a concern. In also should be noted, electromagnetic motor usually produces a low voltage while piezoelectric materials normally generate a very high voltage, so they have different requirements on power electronic circuits.

### 3.2.1 Piezoelectric Transducers

Piezoelectric material is one of most-widely-used smart materials. It can be deformed when certain voltage is applied on the surface, and it can generate voltage or charges on its surface when a force or pressure is exerted on it. While the first characteristic has been used for actuator applications, such as piezoelectric stacks or benders, the second characteristic can be used for



sensor applications, such as, accelerometers, microphones, load cells (Mirzaeifar *et al.*, 2008), or to harvest energy from vibration. The governing electromechanical equations for piezoelectric materials can be expressed by Equation (2.1):

$$\begin{bmatrix} S_p \\ D_p \end{bmatrix} = \begin{bmatrix} s_p & d \\ d & \varepsilon \end{bmatrix} \begin{bmatrix} \sigma \\ E \end{bmatrix} \quad (3.1)$$

where  $S_p$  and  $\sigma$  are strain and stress respectively;  $s_p$  is compliance;  $D_p$  is electric displacement (charge per unit area);  $E$  is electric field (volts per unit length);  $d$  is piezoelectric coefficient, and  $\varepsilon$  is dielectric constant.

When used as energy harvester, the piezoelectric material can work either in 31 or 33 mode as shown in Figure 2.8, where  $t_p$  is the thickness of piezoelectric materials or the distance between electrodes in the polarization direction,  $A_p$  is the area of conductive electrodes. The 31 mode is usually seen in piezoelectric film, where the electric field is perpendicular to the direction of mechanical strain; the 33 mode often appears as piezoelectric stacks where both electric field and strain are in the poling direction. When working as energy harvester, the piezoelectric transducer can be modeled as an AC voltage source with a capacitor in series, as shown in Figure 2.9(a). Based on Thevenin's and Norton's Theorem, it can be also modeled as an AC current source with a capacitor in parallel, as shown in Figure 2.9(b).

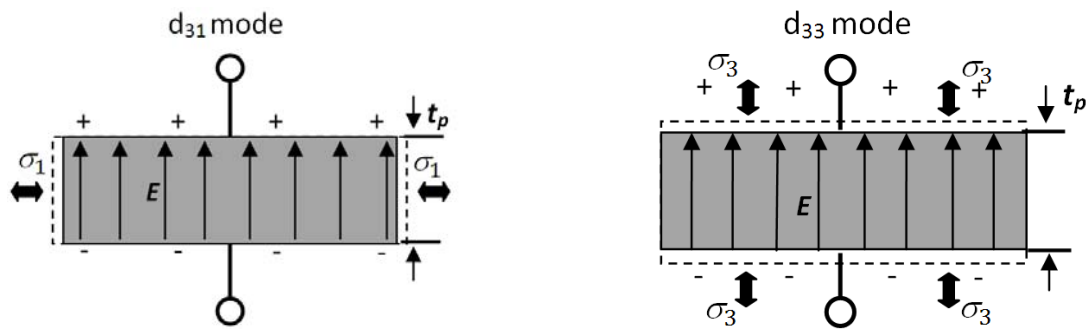


Figure 3.8 Two modes of piezoelectric materials when used for vibration energy harvesting.

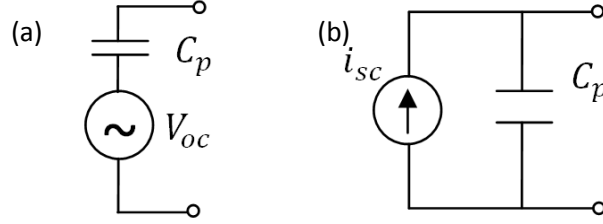


Figure 3.9 Modeling of piezoelectric materials as energy harvesters: (a) voltage source; (b) current source.

When the piezoelectric material is open-circuit, there will be no charge displacement and  $D_p$  is equal to zero. From the relation between electric field and strain in Equation (2.1), the open circuit voltage generated  $V_{oc}$  by the piezoelectric material can be expressed by Equation (2.2).

$$V_{oc} = -E \cdot t_p = -\frac{d \cdot \sigma \cdot t_p}{\varepsilon} = -g \cdot \sigma \cdot t_p \quad (3.2)$$

where  $g$  is the voltage constant, and related with the piezoelectric coefficient  $d$  by Equation (2.3)

$$d = \varepsilon \cdot g \quad (3.3)$$

For the second modeling, the short-circuited current can be obtained by shoring the electrodes of piezoelectric material. In this case,  $E$  is zero, and the electric displacement can be obtained from equation (2.1) as

$$D_p = d \cdot \sigma \quad (3.4)$$

Hence the short circuit current  $i_{sc}$  is obtained as Equation (2.5), which is in proportion to the derivative of the stress:

$$i_{sc} = \dot{D}_p \cdot A_p = d \cdot \dot{\sigma} \cdot A_p \quad (3.5)$$

Or a short circuit electric charge proportional to the stress.

$$Q_{sc} = d \cdot \sigma \cdot A_p \quad (3.6)$$

Many types of piezoelectric materials with different properties can be used as the transducers (Galhardi *et al.*, 2008). The most popular piezoelectric materials are Lead Zirconate Titanate (PZT) ceramic and Polyvinylidene fluoride (PVDF) polymer. PZT ceramic has large electromechanical coupling factors, typically  $k_{31}=0.34$  and  $k_{33}=0.69$  ( $k_{31}$  is the factor for electric

field in direction 3 and longitudinal vibrations in direction 1;  $k_{33}$  is the factor for electric field in direction 3 and longitudinal vibrations in direction 3), which means it is able to convert 34% and 69% of mechanical energy in the piezoelectric material into electrical energy. PVDF is more flexible and sensitive (Shenck and Paradiso, 2001; Starner and Paradiso, 2004), however, the electromechanical converting coefficient is much smaller,  $k_{31}=0.12$  and  $k_{33}=0.15$ . Single crystal piezoelectric materials have also been used for its high energy density, high energy converting efficiency and large operational temperature range (Badel *et al.*, 2006). In general, the piezoelectric materials have relatively small strain, which prevents their direct application in large-amplitude vibrations. On the other hand, this is also one of the advantages of piezoelectric materials, in situations where small deformation is preferred, for example, energy harvesting from human walk (Shenck and Paradiso, 2001; Starner and Paradiso, 2004), where large deformation may have effect on walking gait and cause discomfort to the walker.

Since one piezoelectric ceramic wafer can only generate limited energy due to small deformation, the output power and the efficiency could be improved by stacking them together or group them into arrays. Research & Development Center of JR East Group (East Japan Railway Company, 2008) developed a piezoelectric arrays based power-generating floor, which has been tested at Tokyo Station's Marunouchi North Exit (Figure 2.10). This power-generating floor could harvest 10,000 Watt-seconds per day, which can lighten a 100W bulb for about 80 minutes, which means, it can harvest average power of 5.6W in 24 hours. However, after the third week of the experimental period (a total of 800,000 people passing), production of electricity decreased due to a degradation in durability. Also using stack configuration, Antaki *et al.* (1995) developed a regenerative shoes using piezoelectric ceramic, for the power supply of artificial organs. By arranging the piezoelectric materials in stack and applying force magnification mechanism, an average of 0.85W energy is claimed during the normal walk of a 75kg human, without causing much discomfort to the walking gait.

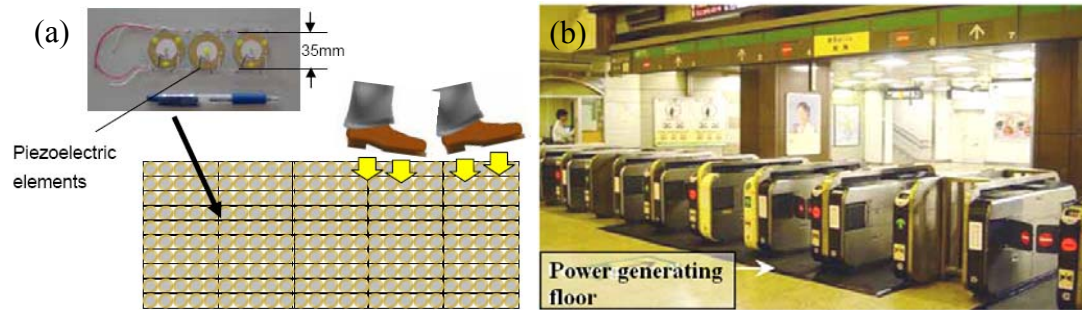


Figure 3.10 Power generating floor: (a) piezoelectric energy harvesting stacks; (b) experiment in Tokyo Station's Marunouchi North Exit (East Japan Railway Company, 2008).

### 3.2.2 Electromagnetic Transducers

Besides of piezoelectric materials, electromagnetic motors are also often used in vibration energy harvesting, especially when the vibration magnitude is large. Electromagnetic motor can act as an actuator and a harvester at the same time and is capable of bi-directional power flow. Actually, electromagnetic motors have already been more-often-used in large scale vibration energy harvesting. Energy recovery from vehicle suspension is such example. Instead of dissipating the vibration energy of the vehicle into heat waste using shock absorbers, the energy can be harvested meanwhile reducing the vibration (Boldea and Nasar, 1997; Nakano *et al.*, 2003; Gupta *et al.*, 2006; Zuo *et al.*, 2011; Li, *et al.*, 2012; Tang *et al.*, 2013). In thesis, the electromagnetic transducers are used for converting the vibration energy into electricity.

#### 3.2.2.1 Direct drive linear electromagnetic machine

This section reviews the current linear electromangetic machine used in large-scale vibration energy harvesting and structural vibration control. Zuo *et al.* (2010) developed a linear energy harvester prototype and showed an average of 16W power can be achieved by one harvester at suspension velocity of 0.25m/s, using axial magnets and spacers. A high magnetic conductive steel casing which moves together with the magnets assembly without introducing eddy current effect, is added to further increase the magnetic flux density, as shown in Figure 2.11.

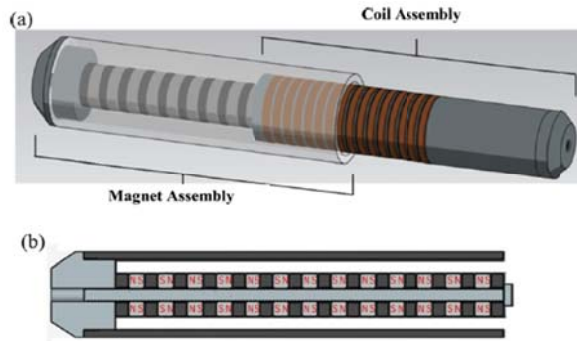


Figure 3.11 Linear electromagnetic harvester for regenerative suspensions (Zuo *et al.*, 2010).

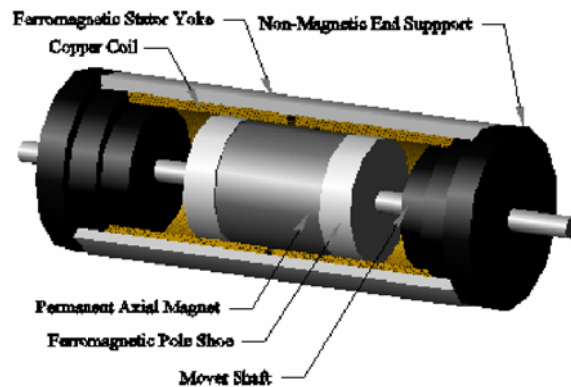


Figure 3.12 The eddy current damper for structural vibration control (Palomera-Arias, 2005).

Bose Corporation (Rani, 2005) spent over twenty years to develop a unique active controlled vehicle suspension system with high-speed linear electromagnetic motor, which can significantly improve the passengers' comfort and the maneuverability of the vehicle. Together with regenerative switching power amplifiers of bidirectional power flow ability, the linear electromagnetic motors are also used to recover part of vibration energy, thus, a reduction of the power consumption in the active control by 33% has been claimed (Rani, 2005). In addition, several researchers also developed linear electromagnetic eddy current dampers, (Palomera-Arias, 2005; Ebrahimi *et al.*, 2008; Zuo *et al.*, 2011b). Figure 2.12 shows the eddy current damper proposed by Palomera-Arias (2005) for structural vibration reduction. Though energy harvesting is not explored in the literature of eddy-current dampers, some idea therein can be extended for the linear electromagnetic harvester design.

### 3.2.2.2 Rotation electromagnetic machine

Although linear electromagnetic motors have the advantage of being easily and reliably integrated into most existing vibration systems without the requirement for transmission mechanism, their efficiency is relative low and their size is still large, because of the relative low vibration velocity. Hence, rotation electromagnetic motors, including DC and AC permanent-magnet motors, are adopted in vibration energy harvesting. Appropriate transmissions are needed to convert the linear motion into rotation.

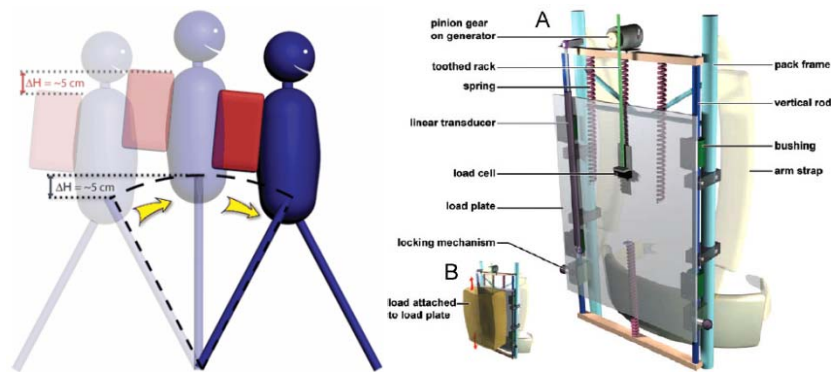


Figure 3.13 Regenerative backpack, harvesting 7.8 W power from walking, 7.8W (Rome *et al.*, 2005).

Using the rotation motor as a generator, Rome *et al.* (2005) developed a backpack driven energy harvesting system (Figure 2.13), which can generate up to 7.4W power with little extra metabolic energy. This device also harvests the energy from normal walking and it is much more efficient compared with the energy harvesting shoes (Shenck and Paradiso, 2001) or the backpack (Granstrom, 2007) based on piezoelectric transducers as I mentioned before. Electromagnetic motor is also used in vibration energy harvesting from building structures (Scruggs 1999 and 2004, Tang and Zuo 2011). For example, Scruggs (1999 and 2004) analyzed the possibility of developing this kind of regenerative actuator and presented a Regenerative Force Actuation (RFA) Network consisting of multiple actuators distributed throughout a structural system to reduce the vibration of the structure, where some actuators can harvest the mechanical energy from the vibration while others re-inject a portion of that energy back into the structure at other location to reduce the vibration.

When used in vibration energy harvesting, rotation electromagnetic generators are usually more compact than the linear motors. However, it requires mechanism to transfer the linear motion of

vibration into rotation motion. Several mechanisms have been proposed and some prototypes have been built to obtain harvesters with rotation electromagnetic motors, including links, screws, rack pinions, and fluids. It should be noted that adding these mechanisms will introduce extra dynamics into existing system, which should be taken into account in the system design and analysis.

Traditionally Ball screw is used to transform the rotation motion of the electromagnetic motor into linear motion, resulting in linear actuator. In energy harvesting from vibration, researchers use it inversely. Kawamoto *et al.* (2008) proposed an electro-mechanical actuator consisting of rotation electromagnetic motor and ball-screw mechanism, as shown in Figure 2.14. A prototype is also built. The ball-screw transfers the linear motion into rotation then drives the electromagnetic motor. Also using ball-screw mechanism, Zheng *et al.* (2007) conducted a full-vehicle experiment to test the vibration performance and feasibility for energy harvesting. Similar mechanisms based on ball-screw can be found in passive vibration control of vehicle suspension (Suda, 2000 and 2006). Applying of ball-screw mechanism to the system will also introduce extra dynamics, which hasn't fully been investigated by researchers. Cassidy *et al.* (2011) designed an electromagnetic transducer with ball-screw mechanism for energy harvesting from large-scale civil structures, for which the power levels can be above 100W for excitation frequencies below 1Hz, as shown in Figure 2.15.

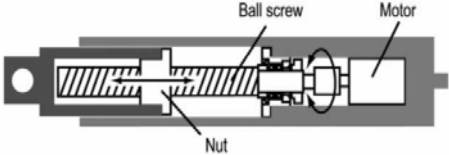


Figure 3.14 Regenerative shock absorber using a ball-screw mechanisms (Kawamoto *et al.*, 2008).

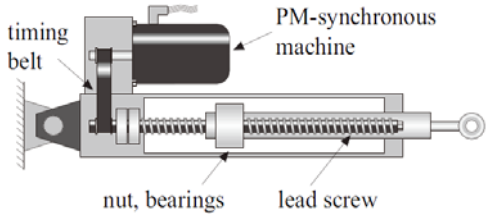


Figure 3.15 Large structural vibration energy harvester using ball-screw mechanism (Cassidy *et al.*, 2011).

Rack and pinion and relevant modified systems, also have potential in linear to rotation motion transformation. It is used in (Rome *et al.*, 2005) to transfer the vertical movement of the mass into the rotation. In practical application, the gear backlash between the rack and pinion is always not negligible, posing uncertain factor to the dynamics. Zuo *et al.* (2010) designed a regenerative vehicle shock absorber with rack-pinion mechanism, as shown in Figure 2.16. Together with bevel gears, the mechanism makes the regenerative shock absorber compact and is retrofittable to the conventional vehicles. Later on, they refined the design and introduced so-called “motion rectifier”, where two pairs of roll-clutches are used. It can convert the bidirectional motion into unidirectional rotation of the motor, resulting in higher efficiency and durability (Li, *et al.*, 2012; Li and Zuo, 2013), as shown in Figure 2.17. It should be noted that the concept of “mechanical motion rectifier” is first proposed by Wang *et al.* (2012) for energy harvesting from railways. Choi *et al.* (2009) used the rack and pinion mechanism to transfer the linear motion of the shock absorber of a vehicle into rotation to drive the generator. An integrated electrorheological (ER) shock absorber, the typical energy consumption of which is 20W, is controlled and driven only using the harvested energy.

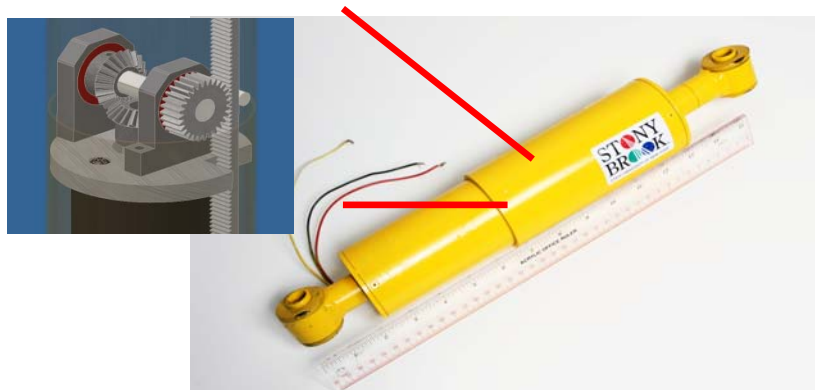


Figure 3.16 Regenerative shock absorber using rack-pinion mechanism (Zuo *et al.*, 2010).



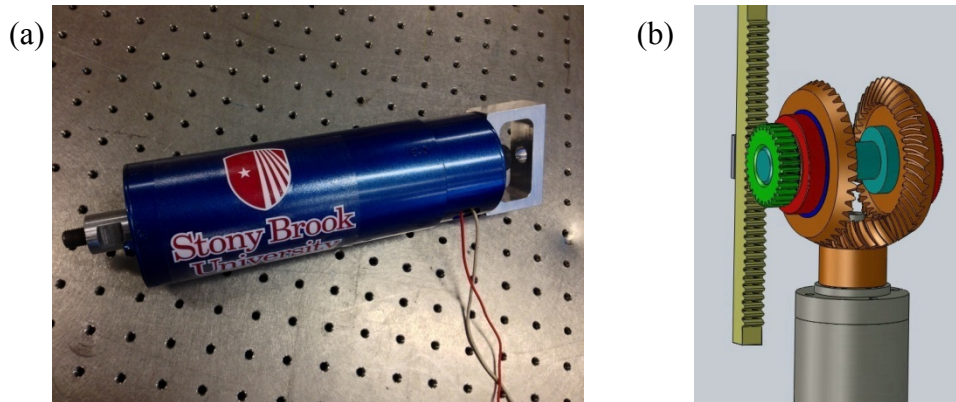


Figure 3.17 Regenerative shock absorber using motion rectifier. (a), prototype; (b), modeling (Li, *et al.*, 2012; Li and Zuo, 2013).

### 3.3 Review on Regenerative Vibration Control

Regenerative vibration control is usually seen in regenerative vehicle suspensions (Suda *et al.*, 1998; Nakano *et al.*, 2003) and regenerative building vibration control (Scruggs, 2004, 2007, 2010). Basically, the concept is to control the vibration while harvesting the kinetic energy. There are several different control algorithms developed in the regenerative vehicle suspensions. However, there is very little relevant work on the regenerative building vibration control, except for on Scruggs' regenerative force actuation networks (Scruggs, 2004, 2007, 2010).

Quite different from small scale vibration energy harvesting, in the large-scale vibration energy harvesting, the vibration performances of the primary structures are always concerned. The researchers often try to make dual usage of the existing vibration control mechanism for energy harvesting. Hence, the vibration energy should be extracted while providing better vibration mitigation of the primary structure, or at least maintaining the vibration suppression of the primary structure. Researchers have looked into different control algorithms to control the relevant circuits in order to mitigate the vibration. There are two typical implementations of the control algorithms: one is designing the full active control algorithm and subsequently put the constraints of the circuit to the feedback force. The methodology can be shown by the diagram in Figure 2.18(a); the other one is to include the constraints due to the energy harvesting circuit when designing the controller. The controller using this method may be formed as a bilinear matrix inequality (BMI) or linear matrix inequality (LMI) problems (Scruggs, 2007, 2010). In addition, many performance objectives can be considered in the same framework (Scruggs *et al.*,

2012). Giorgetti *et al.*(2006) proposed another method for the semi-active suspension control, where the quarter-car model and the constraints of the semi-active control is modeled into a hybrid dynamical systems and Modeling Predictive Control (MPC) is used for the controlled design. It is found that the explicit MPC control law is the same as the clipped LQG control when the predictive horizon is equal to one and MPC control can provide better performance than the clipped LQG control if it has more predictive horizon. Similar observation was also found by Huang *et al.* (2011).

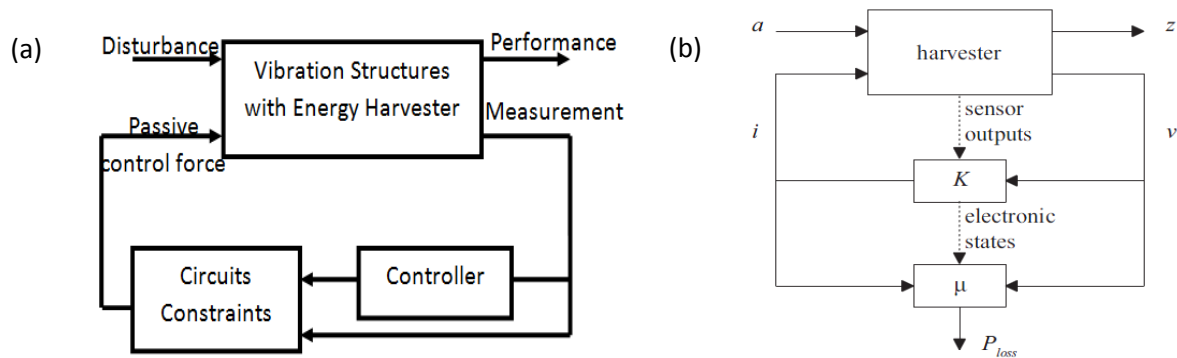


Figure 3.18 Implementations of vibration control in vibration energy harvesting system: (a). using clipped control (Tang and Zuo, 2010c); (b) multi-objectives energy harvesting problem (Scruggs *et al.*, 2011).

On the other hand, instead of harvesting and storing the energy, the harvested electricity is further used to implement active vibration control, resulting self-powered active vibration control (Nakano *et al.*, 2003; Nakano and Suda, 2004). Although little energy for external usage is obtained, the vibration of the primary structure is suppressed significantly. For example, Scruggs and Lindner (1999) investigated the feasibility of self-powered active control on harvesting energy from buildings using simple velocity and displacement feedback algorithm. Tang and Zuo (2010c) confirmed the feasibility with LQG control. The regular rectifier can be used in semi-active control. In active vibration control with energy harvesting, where the power flow is bidirectional, switch based control is usually used (Nakano and Suda, 2004). For example, Nakano *et al.* (2003) analyzed the possibility of self-powered active vibration control using linear electromagnetic motor and concluded that active vibration control without consuming external energy can be achieved under suitable conditions derived from energy balance analysis. Their experiment verified that the vibration mitigation performance of the self-powered active

control is significantly improved over the passive vibration mitigation approaches. Instead of storing the electricity in capacitors, Jolly and Margolis (1997) stored the energy temporarily in inductor and by alternately storing and releasing the energy controlled by switches, realizing a self-powered active control system. Similarly, Zheng *et al.* (2008) analyzed the performance and energy by dividing the whole system into two operation modes controlled by switches, namely electrical motor mode and regenerative braking mode. In electrical motor mode, the optimal ride comfort is obtained by active control; in regenerative braking mode, the system can harvest energy from the vibration and improve the ride comfort performance at the same time.

### **3.4 Summary**

In this chapter, the technologies on mitigating the vibration of civil structures are reviewed, especially the method using TMD or its variants. The modeling of different TMDs, namely the classic TMD, active TMD and semi-active TMD are introduced. Noticing the semi-active control force is essentially a passive force, which means the vibration energy is being dissipated through damping devices, I have proposed the simultaneous energy harvesting and vibration control using the existing TMD. I also reviewed the current research on vibration energy harvesting technology, most of which focuses on small-scale. Through the literature review on the transducers, I found that the electromagnetic transducers are more suitable for vibration energy harvesting from civil structure with TMD, because the relative displacement between the civil structure and TMD is large. I also reviewed the research on regenerative vibration control, most of which are on the control of regenerative suspension, including two implementations of the control algorithms, one of which is designing the full active control algorithm and subsequently put the constraints to the feedback force, the other of which is to include the constraints due to when designing the controller.

## Chapter 3

# Power Estimation and Wind Modeling

In this chapter, the power that is available to be harvested in different civil structures is estimated, using the vibration perception criteria of human beings suggested by ISO. The economic and cost analysis will be briefly discussed. The modeling of wind dynamics and building dynamics are also studied in this chapter.

### 4.1 Power Estimation Based on Vibration Perception Criteria by ISO

#### 4.1.1 Power Estimation

The actual motion of the buildings and towers due to wind induced vibration is mainly narrow bandwidth random vibration around the first bending frequency in two horizontal directions, or around the torsional vibration frequency along its vertical axis (Kareem *et al.*, 1999). In this section, I will estimate how much kinetic power is currently being dissipated, or is harvestable, by existing TMDs in some typical civil structures.

For modern buildings with light weight materials and better flexibility, the fundamental frequencies are usually very low (0.1Hz-0.5Hz), and it is more challenging to maintain the human comfort than to ensure sufficient structural strength (Kareem *et al.*, 1999). The International Standard Organization (ISO) 10137 (2007) suggests limiting criteria for human comfort affected by wind loads based on peak accelerations of residential and office buildings caused by wind speeds with a return period of one year, as shown in Figure 3.1. The limit of

root-mean-square (RMS) values of acceleration has also been used, and the green lines in Figure 3.1 show such thresholds suggested by ISO Standard 6897 (ISO, 1984) based on a 5 year recurrence interval. Typical North American practice is to use 0.1-0.15  $\text{m/s}^2$  peak horizontal acceleration for residential buildings and 0.2-0.25  $\text{m/s}^2$  for office buildings, based on a 10 year recurrence interval (Kareem *et al.*, 1999).

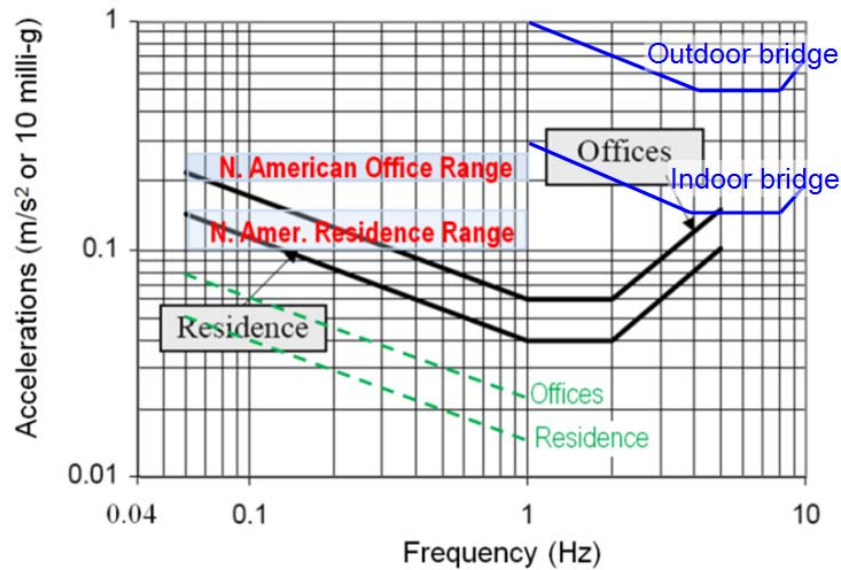


Figure 4.1 Vibration perception criteria of human beings. Peak acceleration suggested by ISO 10137 (solid), RMS acceleration suggested by ISO6897 (dash line), North American practice (red words), and peak acceleration of bridges suggested by ISO 2632-2 (blue line).

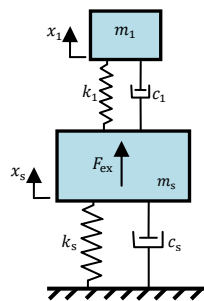


Figure 4.2 Classic TMD

The modeling of TMD has been introduced in Chapter 2 and re-drawn in Figure 3.2. The peak amplitude of the relative displacement between the TMD and the primary building structure in the mode coordinate at the resonance of the structure  $\omega = \omega_s$  can be expressed as

$$|\dot{x}_1 - \dot{x}_s| = \left| \frac{-1}{\omega_1^2 - \omega^2 + i 2\zeta_1 \omega_1 \omega} \right|_{\omega=\omega_s} |\ddot{x}_s| = \frac{1}{\omega_s^2 \sqrt{(f^2 - 1)^2 + (2\zeta_1 f)^2}} |\ddot{x}_s| \quad (4.1)$$

where  $f$  is the tuning ratio of the TMD  $f = \frac{\omega_1}{\omega_s} = \frac{\sqrt{k_1/m_1}}{\sqrt{k_s/m_s}}$ ,  $\zeta_1$  is the damping ratio of the TMD subsystem  $\zeta_1 = \frac{c_1}{2\sqrt{k_1 m_1}}$ , and  $|\ddot{x}_s|$  is the peak amplitude of the building acceleration.

The average dissipating power, which can be obtained by dividing the energy  $\Delta W$  dissipated by the damping force  $c_1(\dot{x}_1 - \dot{x}_s)$  over one cycle divided by time period  $2\pi/\omega_s$ , is expressed by Equation (3.2)

$$P = \frac{\Delta W}{2\pi/\omega_s} = \frac{1}{2\pi/\omega_s} \int_{t=0}^{2\pi/\omega_s} c_1(\dot{x}_1 - \dot{x}_s)(\dot{x}_1 - \dot{x}_s) dt = \frac{m_1 f \zeta_1}{\omega_s [(f^2 - 1)^2 + (2\zeta_1 f)^2]} |\ddot{x}_s|^2 \quad (4.2)$$

Den Hartog (1947) obtained the analytical expression of the optimal tuning rule of TMDs in the 1940s, and it is still the most widely used equation for the design of the classical TMDs. For a lightly-damped structure, Den Hartog's optimal tuning rule is (Den Hartog, 1947),

$$f^{\text{opt}} = \frac{\omega_1}{\omega_s} = \frac{1}{1+\mu} \quad (4.3)$$

$$\zeta_1^{\text{opt}} = \sqrt{\frac{3\mu}{8(1+\mu)}} \quad (4.4)$$

where  $\mu$  is the mass ratio  $m_1/m_s$ . By observing that the optimal tuning ratio  $f = f^{\text{opt}} \approx 1$  and the optimal damping  $\zeta_1^{\text{opt}} \approx \sqrt{3\mu/8}$  for  $\mu=0.25\%-2\%$ , Equation (3.2) can be simplified as

$$P \approx \frac{m_1}{4\omega_s \zeta_1} |\ddot{x}_s|^2 \approx \frac{m_1}{\omega_s \sqrt{6\mu}} |\ddot{x}_s|^2 \quad (4.5)$$

Equation (3.5) gives us a simple estimation of the energy dissipating rate of classical TMDs. The amplitude of structure acceleration will depend on the intensity of the wind, and the peak limits are 0.1-0.15 m/s<sup>2</sup> for residential buildings and 0.2-0.25 m/s<sup>2</sup> for office buildings in North American practice (Kareem *et al.*, 1999). (The ISO 10137 shown in Figure 3.1 suggests the peak limit 0.09 and 0.13 m/s<sup>2</sup> of one year return period for resonant frequency of 0.15 Hz.)

Based on the above analysis, we can estimate that for the 410 tons (or 370 metric tons,  $\mu = 0.02$ ) of TMDs on the office building Citigroup Tower ( $\omega_s = 0.16\text{Hz}$ ), the harvestable power is 43 KW - 67 KW. And the harvestable energy from the 730 tons TMD (660 metric tons) in Taipei 101 is

33 KW - 208 KW. The harvestable energy from some other buildings with TMDs in some structures is listed in Table 3.1.

Table 4.1 Estimated harvestable energy in some structures using the existing TMDs.

Name of Structures	TMD	Frequency	Estimated Power
Taipei 101, Taipei (1474ft)	730 tons, 0.78% modal mass	0.146 Hz	33 kW - 208 kW
CitiGroup Tower, NY	410 tons, 2% modal mass	0.16 Hz	43 kW - 67 kW
Trump World Tower, NYC	600 tons, 2.8% modal mass	0.216 Hz	10 kW - 23kW
Bloomberg Tower, NYC	600 tons	NA	NA
Chicago Spire, Chicago	1300 tons	0.059, 0.2Hz	NA
John Hancock Tower, Boston	300 tons + 300 tons	0.14Hz	NA
Shinjuku Park Tower, Tokyo	330 tons	NA	NA
Crystal Tower, Osaka, Japan	180 tons + 360tons, 4.2% in Y, 2.2% in rotation	0.24-0.28 Hz	26 kW - 40kW
Chifley Tower, Sydney	400 tons, 2% modal mass	0.25 Hz	27 kW - 42kW
Bronx-Whitestone Bridge, NY	94 tons, 0.39% modal mass	0.1 Hz	142 kW-320 kW

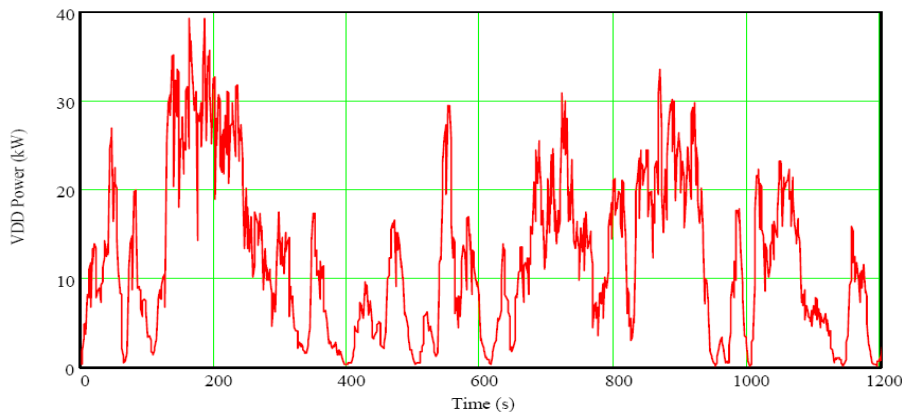


Figure 4.3 Power dissipated by one of the eight viscous damping devices in the TMD on Taipei 101 in wind-induced vibration (Haskett *et al.*, 2004).

In the state of arts, oil-based viscous dissipating devices are used in TMDs. Such a large power rate already creates a lot of challenges, and forced liquid cooling or a heat resistant design must be used. Figure 3.3 shows the energy dissipated by one of the eight oil dampers in the TMD of

Taipei 101 during a wind event with 100 year recurrence interval (Haskett *et al.*, 2004). We can conclude that our estimation agrees well with the recorded data well.

#### 4.1.2 Economic Analysis

Besides better vibration mitigation in hazards, the research in this thesis can bring significant economic benefits in term of the energy and environment to the high-rise buildings. In this section I will look into the economic feasibility.

The vibration perception criteria in Chapter 3.1.1 is used to estimate the harvestable energy, which assumes that large wind is acting on the structures. In practice the wind speed varies day by day and hour by hour. The speed usually follows Weibull distribution. Figure 3.4 shows such measurement data (RERL Wind Data). The vibration intensity of the TMD and structures will depend on the wind speed and direction, as well as structure and TMD design. Figure 3.5 shows the measured peak acceleration and wind speed of some an 84m building (Denoon and Kwok, 1996) (30% height of Citigroup Tower). Though these two sets of data are at different sites, they give us some hints to make assumptions for the first order estimation of the annual energy (accurate estimation depends on the particular site and structure): for 50% of the time the TMD stays calmly or is locked to the structure, and for 40% of the time the TMD harvests energy at 60% of the power rate calculated in Chapter 3.1.1, and for 10% of the time TMD harvests at full power rate (structure 0.1-0.25 m/s<sup>2</sup>). Subsequently we estimate the annual harvested electric energy as:

$$(0.4 \times 0.6 + 0.1) \times (50 \sim 100) \text{ KW} \times 365 \times 24 \text{ H} = 150,000 \sim 300,000 \text{ KW-H} \quad (4.6)$$

Recent statistics from the U.S. DOE (2006) estimate that the average electricity used in a house on a national level is about 920 KW-H per month with a corresponding annual CO<sub>2</sub> emission of 7.5 tons. Therefore, the proposed technology implemented in a single high-rise building can power 14-27 typical houses in the US, and reduce CO<sub>2</sub> emissions by 105-203 tons annually. At rate of \$0.15/KW-H (New York state residents pay at \$0.19/KW-H), \$22,500~\$45,000 will be saved on energy bills a year from the implementation in a single skyscraper.





Figure 4.4 A typical wind speed distribution in a period of three months measured in Boston area (RERL Wind Data).

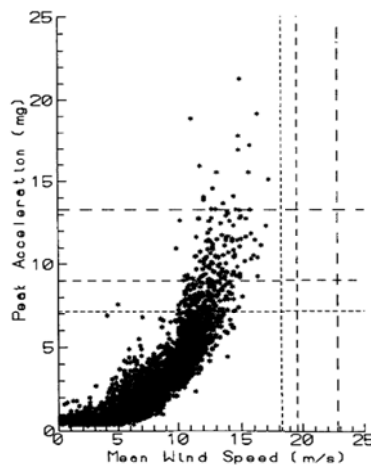


Figure 4.5 Peak acceleration of a structure at various wind speed (Denoon and Kwok, 1996).

Table 4.2 Cost Estimation on the retrofit of the TMD in Taipei 101.

Hardware and Software Cost	Electromagnetic transducer (25kW)	\$1,000X 8
	Motion mechanism (ball-screw)	\$500X8
	Electronics components and sensors	\$900X8
	Grid tie inverter (grid feeding)	\$5,000
	Control unit	\$3,000
Installation Labor Fee		\$20,000
Total Cost of Full-scale Implementation		\$47,200

The electricity-generating TMD can be retrofitted into existing buildings with TMDs (like the CitiGroup Tower or Taipei 101), or some buildings with space reserved for TMDs, for example, Carnegie Hall Tower in NYC), or be integrated into new buildings. It is hard to tell the exact cost of a full-scale implementation at the early research stage, however, a quick estimation can be carried out. For the retrofit implementation with classic TMDs, we will replace the viscous energy-dissipating device with the energy-harvesting system composed of an electromagnetic transducer, power electronics (including battery storage), sensors, a grid tie inverter, and a controller. The cost estimation of a full-scale implementation is shown in Table 3. 2. It suggests that we can recoup the investment within in 1-2 years.

## 4.2 Wind Modeling

In section 3.1, the vibration power that is available for harvesting is estimated based on the vibration perception suggested by ISO, where the dynamics of the wind and building integration is simplified and the disturbance is assumed to be harmonic. To better understand the vibration induced by the wind, the wind modeling is studied in this section. It should be noted that the wind modeling has been studied by many researchers (Samali *et al.*, 2004; NatHaz Modeling Laboratory, 2007; Ni *et al.* 2011). Hence, some of the results are cited and reviewed here in this chapter.

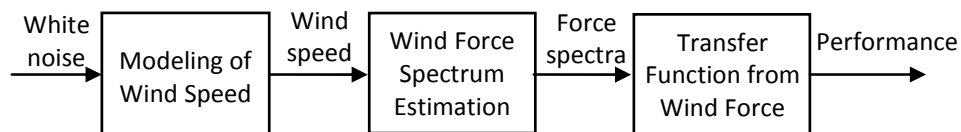


Figure 4.6 Performance calculation based on the wind modeling, wind force spectrum and building dynamics.

In this section, the wind speed is first simulated based on the wind data measured by National Oceanic and Atmospheric Administration (NOAA). Then, the across- and along-wind induced forces are calculated with the spectrum method, and then used as input forces for a 76 story benchmark building. The whole system from wind modeling to TMD controlled building performance is then calculated by taking account of both wind and structure dynamics, the methodology of which is shown in Figure 3.6.

The 76-story benchmark building will be used for the simulation in this section. It is proposed by researcher in structural vibration control for fair comparison of different control algorithms, as described in literature (Samali *et al.*, 2004). The total mass of the building is 153,000 metric tons, with a height of 306.1 m. The total volume of the building is 510,000 m<sup>3</sup>, implying the mass density is 300 kg/m<sup>3</sup>. The cross section of this building is a square with width and length of 42 m on each side. The aspect ratio can be calculated as 306.1/42=7.3. The building is model as vertical cantilever beam with first five natural frequencies are 0.16, 0.765, 1.992, 3.790, and 6.395 Hz. The damping ratio for the building in lateral direction is assumed to be 1%.

#### 4.2.1 Wind Speed Modeling

The wind speed is significant dependent on the location height and terrain topography. It can be decomposed into two parts: the mean part and the fluctuating part. The fluctuating part of wind speed contributes to the randomness of wind, so it is more important to simulate the fluctuating wind speed for along wind response. Several literatures have discussed about how to simulate the wind speed including using spectral based schemes and time based approach schemes (Kareem, 2008; Chen and Kareem, 2001). Since the autoregressive (AR) method for wind simulation does not require large amount of computer memories, it is used to model the wind in this thesis. Using the above AR model, which is detailed in (Chen and Kareem, 2001; Ni *et al.* 2011) the simulated wind power spectrum is plotted and compared with the (2011) in Figure 3.6. The annual wind speed data from NOAA, which were based on the measured wind speed 3 miles offshore from Chicago lakeshore, Illinois during the year of 2009 is used to simulate the average wind speed. Since the NOAA data were sampled at every 5 minutes, the NatHaz on-line wind simulator (NatHaz Modeling Laboratory, 2007) is used as a supplement to generate fluctuation wind speed with higher sampling rate.

The mean wind speed is very sensitive to the height. The mean wind speed  $U_h$  at different height  $h$  usually follows a power law (Davenport, 1967):  $U_h = U_r * (h/r_h)^{\alpha_a}$ , where  $r_h$  refers the reference height,  $U_r$  is the speed at reference height, and  $\alpha_a$  is the power law exponent (Hellman exponent) which is 0.365 for urban area setting. The mean wind speed and fluctuating wind speed acting on each floor of the 76 story benchmark building (Samali *et al.*, 2004) are plotted in

Figure 3.8. The mean wind speed increases as the height increases, however, the fluctuating wind speed appears to be independent of the height.

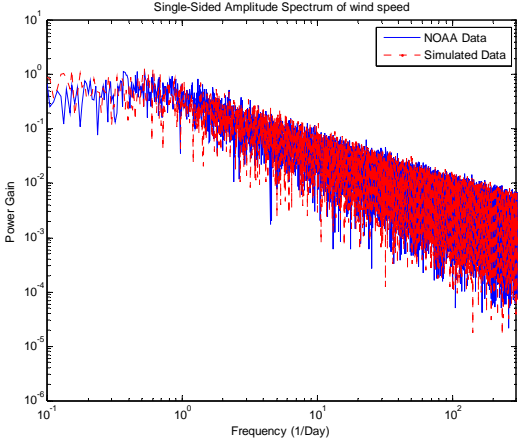


Figure 4.7 Power spectrum comparison of simulated and measured wind speed (Ni *et al.*, 2011).

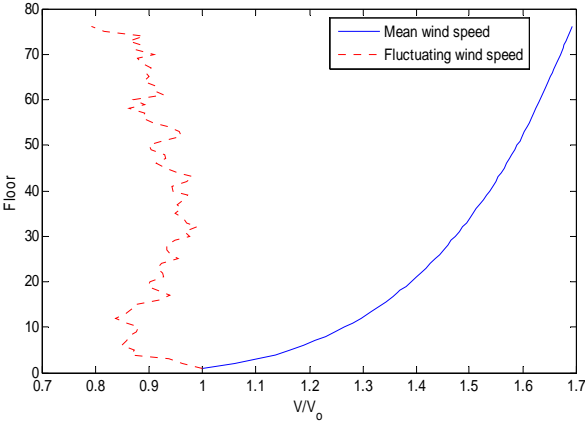


Figure 4.8 Mean wind speed and fluctuation along the height of the benchmark building (Ni *et al.*, 2011).

### 4.2.2 Wind Force Modeling

Once wind speed is simulated, wind forces acting on the building can be calculated. These forces can be decomposed into three components, along wind force, across wind force, and torsion force.

The along-wind forces acting on the building can be calculated by taking the spectrum of the fluctuating wind speed and the aerodynamics into account (Zhou *et al.*, 2002), the spectrum for the along wind force can be written as:

$$S_{Fa} = (C_d \rho U_H B H)^2 \chi^2(f) S_u(f) \quad (4.7)$$

where  $C_d$  is the drag coefficient,  $\rho$  is the air density,  $BH$  is the projection area in the wind direction. The normalized along-wind speed spectrum  $(f S_u(f)) * (\sigma^{-2})$  is plotted in Figure 3.9, for typical wind speed, the dominate along-wind frequency does not coincide with the 1<sup>st</sup> mode of natural frequency of the building. Since the natural frequency of the building is typically higher than the dominant wind fluctuations, the along-wind forces typically contribute to the background and resonant response.

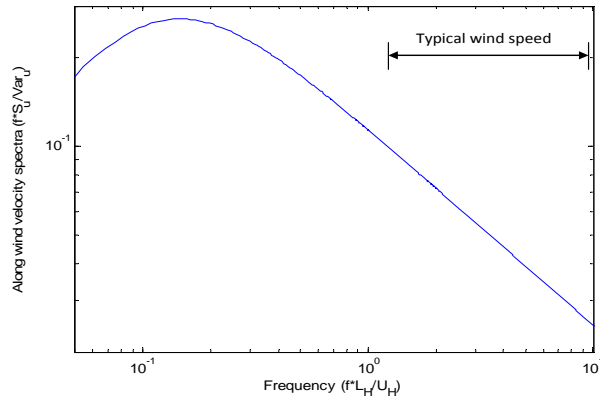


Figure 4.9 Normalized spectrum of along-wind fluctuating speed. (Ni *et al.*, 2011).

Unlike along-wind forces, the across-wind forces are typically narrow banded forces with a large gain around the dominant frequency. The across-wind forces tend to excite most flexible tall buildings which may lead to occupant discomfort. Humans are sensitive to acceleration higher than 5mg in horizontal direction. Due to the complexity of the across wind loading mechanism it is theoretically not tractable by akin to the along-wind component. Typically, wind tunnel tests are conducted to measure the fluctuating loads in the across wind side. However, it is inconvenient and costly to develop wind tunnel test for every tall buildings. The spectral approach provided by Kareem (1984), provides a fast and accurate result on predicting the across-wind forces spectrum acting on tall building based on analysis and curve fitting:

$$S_{F_x}(Z, f) = A_A H_h(C_1) \left(\frac{f}{2\pi n}\right)^2 / \left[ \left(1 - \left(\frac{f}{2\pi n}\right)^2\right)^2 + C_1 \left(\frac{f}{2\pi n}\right)^2 \right] + (1 - A) C_2^{0.5} \left(\frac{f}{2\pi n}\right)^3 / [1.56 \left[ \left(1 - \left(\frac{f}{2\pi n}\right)^2\right)^2 + C_2 \left(\frac{f}{2\pi n}\right)^2 \right]] \quad (4.8)$$

where  $S_{F_x}(f)$  is the across-wind forces spectrum; The reduced frequency is defined as  $n = fB/U_H$ ;  $\beta$ ,  $\alpha$ ,  $f_p$ , and  $S_p$  are parameters relative to building breadth  $B$ , depth  $D$ , and aspect ratio  $D/B$ , and wind field condition. The parameters can be found in (Tschanz and Davenport, 1983). Based on the calculation above, the 1<sup>st</sup> mode normalized across-wind reduced spectrum  $(fS_{F_x}(f)) * \{0.5\rho U_H^2 BH\}^{-2}$  is plotted as shown in Figure 3.10 for tall slender buildings. For typical square/rectangular tall buildings, the Strouhal number is around 0.1. The plot shows that the across-wind force spectrum is largest when the reduced frequency equals to the Strouhal number. In addition, for normal tall buildings, it is easier for the dominate frequency of across-wind forces to coincide with the natural frequency of the building than the along-wind.

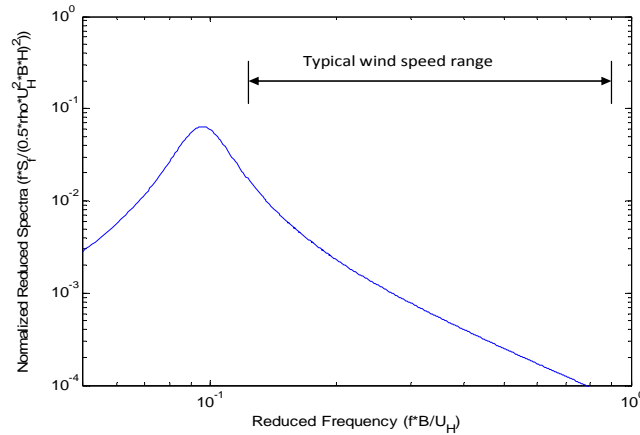


Figure 4.10 Normalized spectrum of across-wind force (Ni *et al.*, 2011).

### 4.3 Summary

In this chapter, I estimated the vibration energy that is available for harvesting in different civil structures, using vibration perception criteria of human beings suggested by ISO. It is found that about 10KW- 300KW can be harvested from different structures, which can power 14-27 typical houses in the US, and reduce CO<sub>2</sub> emissions by 105-203 tons annually. Table 3.1 shows the detailed power estimation of different civil structures. The economic analysis in this chapter suggests that we can recoup the investment within in 1-2 years. The wind modeling is also investigated in this chapter.

## Chapter 4

# Optimization of Different TMDs for Vibration Control and Energy Harvesting

In this chapter, different TMDs will be investigated and optimized for vibration control and energy harvesting, including the traditional vibration energy harvester, the newly proposed electromagnetic TMDs, series TMD, electricity-generating TMD and electromagnetic series TMD. The parameters of the electricity-generating TMD and electromagnetic TMDs are optimized analytically with closed-form solutions, which are very convenient in practical applications. The parameters of the series TMD and electromagnetic series TMDs are optimized numerically using decentralized control method. In addition, the advantages of the TMDs with new configurations, for example, smaller mass requirement, more effectiveness, more robustness, smaller actuation force when used for self-powered active control, are discussed in this chapter.

### 5.1 Some Discussions on the Traditional Vibration Energy Harvester

#### 5.1.1 Harmonic Excitation

Figure 4.1 shows the traditional single DOF vibration energy harvester subjected to force excitation on the mass. The single DOF vibration energy harvester is among the most popular

configurations used in the vibration energy harvesting system (Stephen, 2006). It consists of a moving mass connected to the base with a spring, an energy transducer and parasitic damping element. When subjected to force excitation, the governing equation of the vibration harvester with electromagnetic transducer is expressed as:

$$\begin{cases} m_s \ddot{x}_s + k_s x_s + c_m \dot{x}_s + f_e = F_{ex} \\ f_{EMF} = \frac{k_t k_e \dot{x}_s}{R_H} \end{cases} \quad (4.1)$$

where  $f_{EMF}$  is the force provided by the energy transducer (back electromotive force of electromagnetic transducers),  $c_m$  is the mechanical damping of the system,  $k_t k_e$  are the thrust motor constant and the back electromotive force coefficient (EMF), respectively.  $R_H$  is resistance of the electric load. The equivalent force  $f_{EMF}$  is treated as a viscous damping force, which is valid for electromagnetic based energy transducer with resistive load (Tang and Zuo, 2009). As seen in Equation (4.1) the damping force can be controlled via adjusting the resistance of the electric load  $R_H$ , one practical implementation of which is controlling duty cycle of the DC-DC converter, (Ottman, *et al.*, 2003; Zuo and Tang, 2009). The equivalent damping coefficient due to the electric load is denoted as  $c_e$ . Hence, the total damping of the system is  $c = c_m + c_e$ . The total damping ratio  $\zeta = \zeta_m + \zeta_e$ , where  $\zeta_m = c_m / 2m_s \omega_s$  is the parasitic mechanical damping ratio, and  $\zeta_e = c_e / 2m_s \omega_s$  is the equivalent damping ratio due to the electric load.

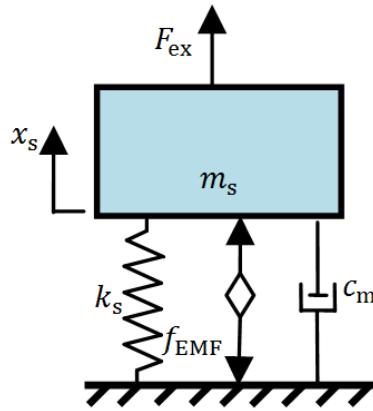


Figure 5.1. Single DOF vibration energy harvester with harmonic force excitation.

When transducer is based on piezoelectric material, the force due to harvester and resistive electric load can be expressed as (Guyomar, *et al.*, 2005):



$$f_{\text{EMF}} = \left( k_{\text{PE}} + \frac{R_{\text{H}}\alpha_{\text{p}}^2 S}{1 + C_{\text{P}}R_{\text{HS}}} \right) x_{\text{s}} \quad (4.2)$$

where  $k_{\text{PE}}$  is the stiffness of the piezoelectric transducer when it is short-circuited,  $\alpha_{\text{p}}$  is the force factor of the piezoelectric material,  $C_{\text{P}}$  is the capacitance of the piezoelectric transducer. Equation (4.2) shows that the piezoelectric harvester will have viscoelastic effect rather than viscous damping effect. Though this thesis mainly focuses on energy harvesting using electromagnetic transducers, the methodology used herein can be extended to the optimization of piezoelectric based harvesters by replacing Equation (4.1) with Equation (4.2).

When the excitation force  $F_{\text{ex}}$  in Equation (4.1) is harmonic, the system response will come to steady-state, which is in the form of:

$$x_{\text{s}} = X_{\text{s}} \sin(\omega t - \theta) \quad (4.3)$$

where

$$X_{\text{s}} = \frac{F_{\text{ex}}}{\sqrt{(k_{\text{s}} - m_{\text{s}}\omega^2)^2 + c^2\omega^2}} \quad (4.4)$$

The actual useful power harvested by the harvester is the power extracted by the electrical load. Hence, the average harvesting power in dimensionless form can be written as:

$$\overline{P_{\text{ave}}}(\alpha, \zeta_{\text{e}}) = \frac{P_{\text{ave}}}{F_{\text{ex}}^2/\omega_{\text{s}}m_{\text{s}}} = \frac{\frac{1}{2}c_{\text{e}}\omega^2 X_{\text{s}}^2}{F_{\text{ex}}^2/\omega_{\text{s}}m_{\text{s}}} = \frac{\zeta_{\text{e}}\alpha^2}{(1-\alpha^2)^2 + 4(\zeta_{\text{m}} + \zeta_{\text{e}})^2\alpha^2} \quad (4.5)$$

where  $\omega_{\text{s}} = \sqrt{k_{\text{s}}/m_{\text{s}}}$  is the undamped natural frequency of the mechanical system,  $\alpha = \omega/\omega_{\text{s}}$  is the normalized excitation frequency. As suggested by Equation (4.5), the power the single DOF energy harvester can obtain is dependent on the damping ratio due to the electric load and the excitation frequency. Figure 4.2 and contours in Figure 4.3 show that there is an global optimal electrical damping ratio  $\zeta_{\text{e}}$  and normalized excitation frequency  $\alpha$ , at which the maximum power can be attained. The global maximum dimensionless power is 6.25 for  $\zeta_{\text{m}} = 1\%$ . Figure 4.2 also indicates that the energy harvesting rate reduces very fast with the decrease of  $\zeta_{\text{e}}$  when the actual damping ratio is smaller than  $\zeta_{\text{e}}^{\text{opt}}$ . It decreases slowly with the increase of  $\zeta_{\text{e}}$  when the actual damping ratio is larger than  $\zeta_{\text{e}}^{\text{opt}}$ , which means the power is less sensitive to  $\zeta_{\text{e}}$  when it is larger than  $\zeta_{\text{e}}^{\text{opt}}$ . This result suggests that higher damping is preferable if the optimal damping is hard to be achieved in real implementation.

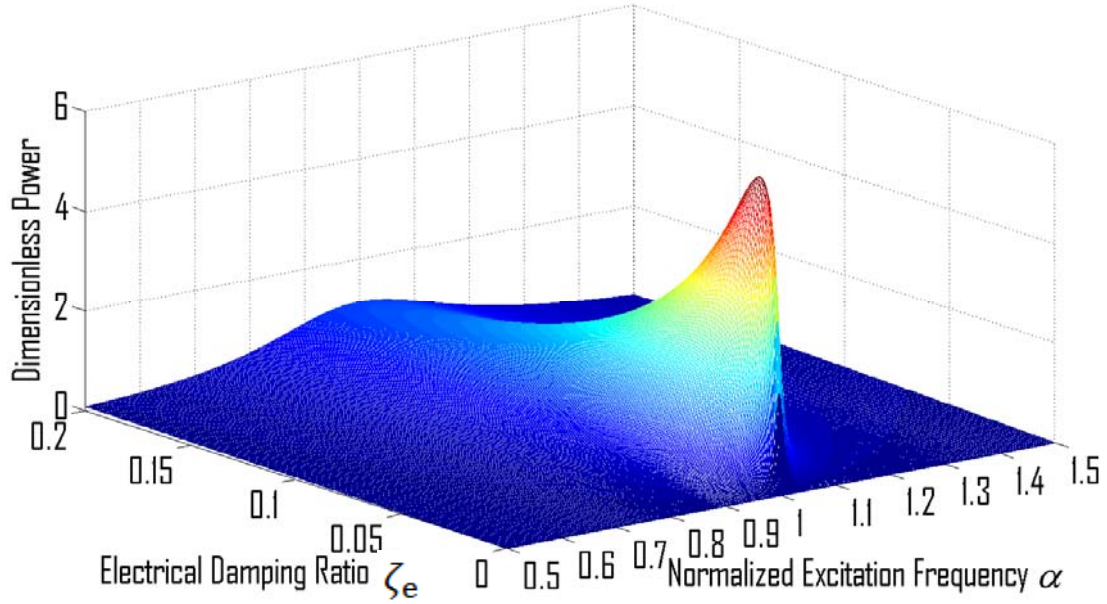


Figure 5.2 Dimensionless average harvesting power  $\overline{P_{ave}}$  at different excitation frequency  $\alpha = \omega/\omega_s$  and electrical damping ratio  $\zeta_e$ , where the mechanical damping is  $\zeta_m=1\%$ . The peak of  $\overline{P_{ave}}$  is 6.25 at the optimal condition ( $\alpha = 1$  and  $\zeta_e = \zeta_m$ ).

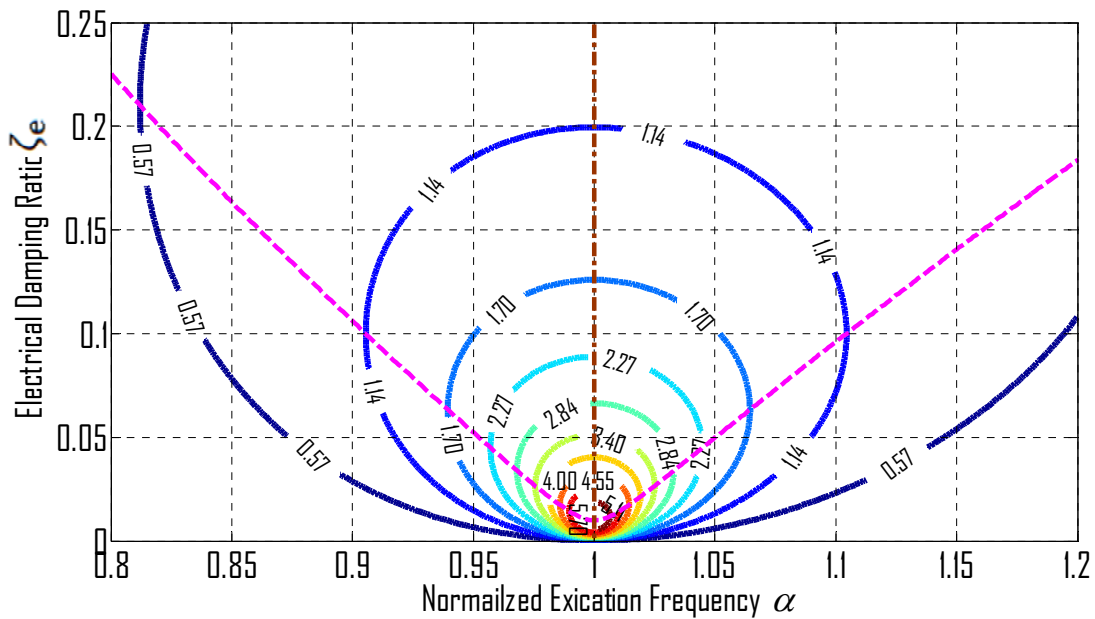


Figure 5.3 Contours of dimensionless average harvesting power  $\overline{P_{ave}}$  at different excitation frequency  $\alpha = \omega/\omega_1$  and electrical damping ratio  $\zeta_e$ , where the mechanical damping is  $\zeta_m=1\%$ . (purple dashed curve shows the optimal electrical damping ratio; grey dashed-dot curve shows the optimal excitation frequency at a given electrical damping).

In order to obtain the optimal damping ratio due to the electric load  $\zeta_e^{\text{opt}}$ , we rewrite Equation (4.5) in the following form:

$$\overline{P_{\text{ave}}}(\alpha, \zeta_e) = \frac{\alpha^2}{\frac{(1-\alpha^2)^2 + 4\zeta_m^2 \alpha^2}{\zeta_e} + 4\zeta_e \alpha^2 + 8\zeta_m \alpha^2} \quad (4.6)$$

Hence, the optimal electrical damping ratio  $\zeta_e^{\text{opt}}(\alpha)$  at different excitation frequency  $\alpha = \omega/\omega_1$  is obtained as:

$$\zeta_e^{\text{opt}}(\alpha) = \sqrt{\zeta_m^2 + \frac{(1-\alpha^2)^2}{4\alpha^2}} \quad (4.7)$$

The dashed line in Figure 4.3 shows the optimal  $\zeta_e^{\text{opt}}(\alpha)$  at different excitation frequency as indicated by Equation (4.7). We see that the optimal electrical damping  $\zeta_e^{\text{opt}}(\alpha)$  is larger than the mechanical damping  $\zeta_m$  unless the excitation frequency is the same of the undamped natural frequency. If the excitation is 5% larger or smaller than the system natural frequency, the desired electric damping  $\zeta_e$  will increase from  $\zeta_m$  to over  $5\zeta_m$ , otherwise the harvesting power will decrease to half if we keep  $\zeta_e$  the same as  $\zeta_m$ . Figure 4.4(a) and (b) show the dimensionless powers and displacements at different excitation frequencies when the electrical damping ratio  $\zeta_e$  is optimal (as in Equation (4.7)) and when the damping ratio is fixed as  $\zeta_e = \zeta_m$ . We see the influence to displacement is not very large, but the influence to the harvesting power is remarkable.

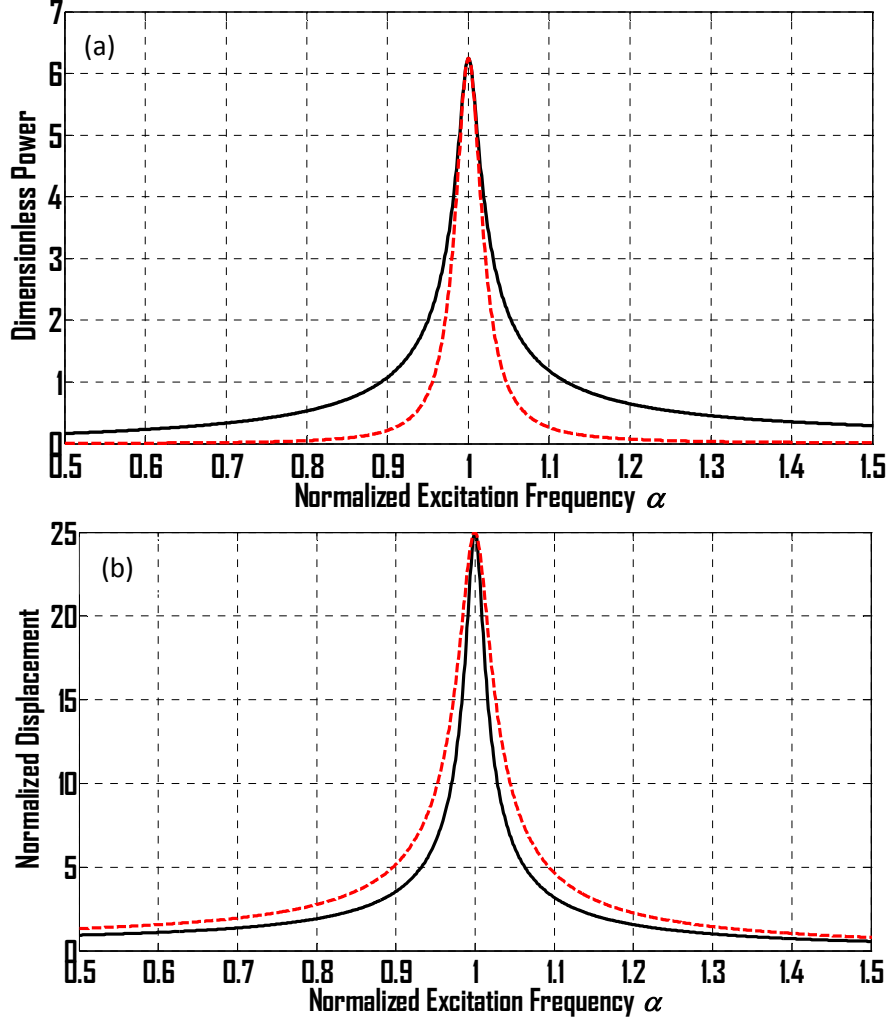


Figure 5.4 Harvesting power and displacement of the mass at different frequencies, when mechanical damping  $\zeta_m=1\%$ . (a). dimensionless power; (b). normalized displacement. (Solid-black: Optimal  $\zeta_e$ . dashed-red:  $\zeta_e = \zeta_m = 1\%$ ).

Substituting the optimal damping in Equation. (4.7) into Equation (4.5), the maximum dimensionless power at different frequencies can be expressed as:

$$\overline{P_{ave}^{max}}(\alpha) = \frac{\alpha}{4\sqrt{(1-\alpha^2)^2 + 4\zeta_m^2\alpha^2 + 8\zeta_m\alpha}}, \text{ where } \zeta_e = \zeta_e^{opt}(\alpha) \quad (4.8)$$

By taking the derivative of Equation (4.8)  $\partial \overline{P_{ave}^{max}} / \partial \alpha$ , and setting it to zero, we can further conclude that the maximal harvesting power happens when the excitation frequency is the same as the system natural frequency ( $\alpha = 1$ ), and the electrical damping is the same as mechanical

damping  $\zeta_e^{\text{opt}} = \zeta_m$ . The global maximum of dimensionless harvesting power can be expressed as:

$$\overline{P}_{\text{ave}}^{\text{max}} = \frac{1}{16\zeta_m} \quad (4.9)$$

In fact, the contour of Figure 4.3 also indicates that for a given electrical damping the maximum harvesting power is achieved when the excitation frequency is the same as natural frequency, where

$$\overline{P}_{\text{ave}}^{\text{max}}(\zeta_e) = \frac{1}{4\frac{\zeta_m^2}{\zeta_e} + 4\zeta_e + 8\zeta_m}, \text{ where } \alpha^{\text{opt}} = 1 \quad (4.10)$$

In conclusion, the maximal harvesting power occurs when the excitation is the same the natural frequency and the electrical damping is the same as mechanical damping, and it is inverse proportional to the mechanical damping. It should be noted this conclusion has been reported in literature (Stephen, 2006); yet, in this thesis more comprehensive discussions are provided. For fixed excitation frequency, the electrical damping for optimal power harvesting depends on the tuning ratio and is general much larger than the mechanical damping. So when the vibration energy harvester is used in off-resonance situation, large electrical damping ratio is preferred. For fixed electrical damping, the excitation frequency should be the same as the natural frequency. For harmonic force excitation, the harvesting power is proportional to  $1/\omega_s m_s$ , or  $\omega_s/k_s$ , or  $1/\sqrt{k_s m_s}$ .

### 5.1.2 Random Force Excitation

For the single-mass vibration energy harvester subjected to random force excitation, the transfer function from the force to the square root of energy output can be written as:

$$\text{TF} = \sqrt{P}/F_{\text{ex}} = \sqrt{c_e}|\dot{x}_s|/F_{\text{ex}} = \left| \frac{\frac{i\omega_s\sqrt{c_e}\alpha}{k_s}}{-\alpha^2 + 2i\alpha\zeta + 1} \right| \quad (4.11)$$

The instant output power of the vibration energy harvester will be  $P = c_e \dot{x}_s^2$ .

When the vibration energy harvesters are subjected to white-noise random excitation, the energy harvesting performance index can be defined as the root-mean-square (RMS) value of the output power of the vibration energy harvester over the power spectrum of excitation force:

$$I_P = \frac{E[P]}{S_F} = \frac{E[c_e \dot{x}_s^2]}{S_F} = \frac{\langle c_e \dot{x}_s^2 \rangle}{S_F} \quad (4.12)$$

where  $E[\cdot]$  stands for the means square value, and  $\langle \cdot \rangle$  stands for the temporal average, respectively. The system is subjected to the excitation with a uniform power spectrum  $S_F$ .

The mean square value of the output power can be expressed by:

$$E[P] = \frac{1}{2\pi} \int_{-\infty}^{\infty} S_F |TF|^2 d\omega = \frac{1}{2\pi} \frac{c_e S_F \omega_s^3}{k_s^2} \int_{-\infty}^{\infty} \left| \frac{i\alpha}{-\alpha^2 + 2i\alpha\zeta + 1} \right|^2 d\alpha \quad (4.13)$$

As seen from Equations (4.11) and (1.13), the output power performance index  $\sqrt{I_P}$  is essentially the  $H_2$  norm of the system where the input is the random excitation and the output is the square root of the power (Zhou *et al.*, 1995). The integral of Equation (4.13) can be obtained by using residue theorem, the general result of which can be expressed by the following equation:

$$I = \int_{-\infty}^{\infty} \left| \frac{B_0 + i\omega B_1}{A_0 + i\omega A_1 - \omega^2 A_2} \right|^2 d\omega = \frac{\pi(A_0 B_1^2 + A_2 B_0^2)}{A_0 A_1 A_2} \quad (4.14)$$

The final result of Equation (4.12) can be expressed as in a very concise form:

$$I_P = \frac{\zeta_e}{2m_s(\zeta_m + \zeta_e)} \quad (4.15)$$

Remark 1: As shown by Equation (4.15), the energy harvesting performance is inverse proportional to the weight of the mass. This result suggests that if the ratio of damping  $\zeta_e/\zeta_m$  is constant, a lighter mass will be better when the harvester has random force excitation. The equation also shows that the output power of the vibration energy harvester is independent of the stiffness of the system if  $\zeta_e/\zeta_m$  is constant. In another word, the stiffness play role only through  $\zeta = c/(2\sqrt{k_s m_s})$ .

Remark 2: There is no finite optimal value for the electric damping ratio  $\zeta_e$  or  $\zeta_e/\zeta_m = c_e/c_m$ . The output power always increases with the electric damping ratio  $\zeta_e/\zeta_m$ . High  $\zeta_e/\zeta_m$  is preferred for better energy harvesting performance, as shown by Figure 4.5. As also seen from Figure 4.5, the power first increases very fast with the ratio of electric and mechanical damping, then the

increasing rate becomes smaller. So in practice, the mechanical damping should be at least 3-5 times less than the electrical damping.

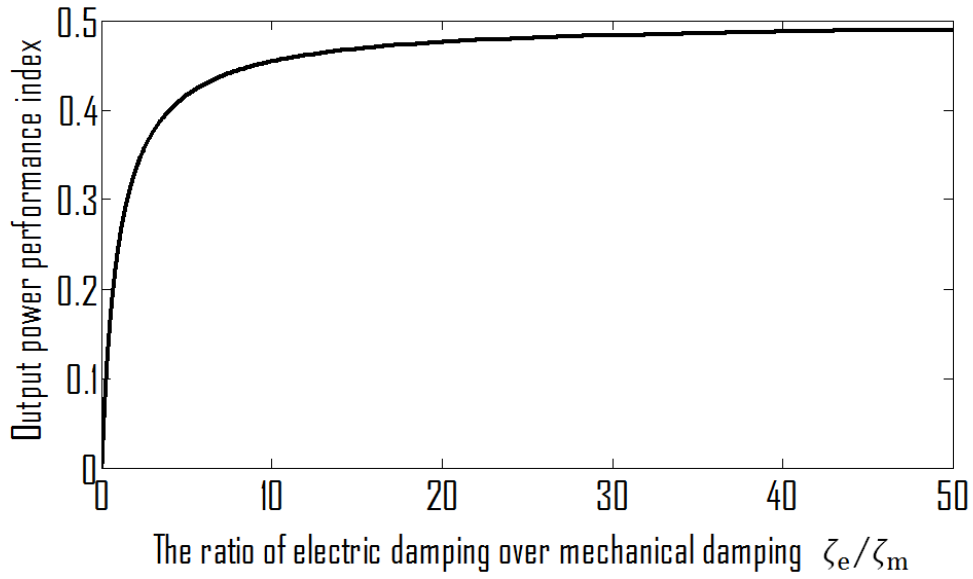


Figure 5.5 Output power performance index at different ratio of  $\zeta_e/\zeta_m$  ( $m_s=1$ ).

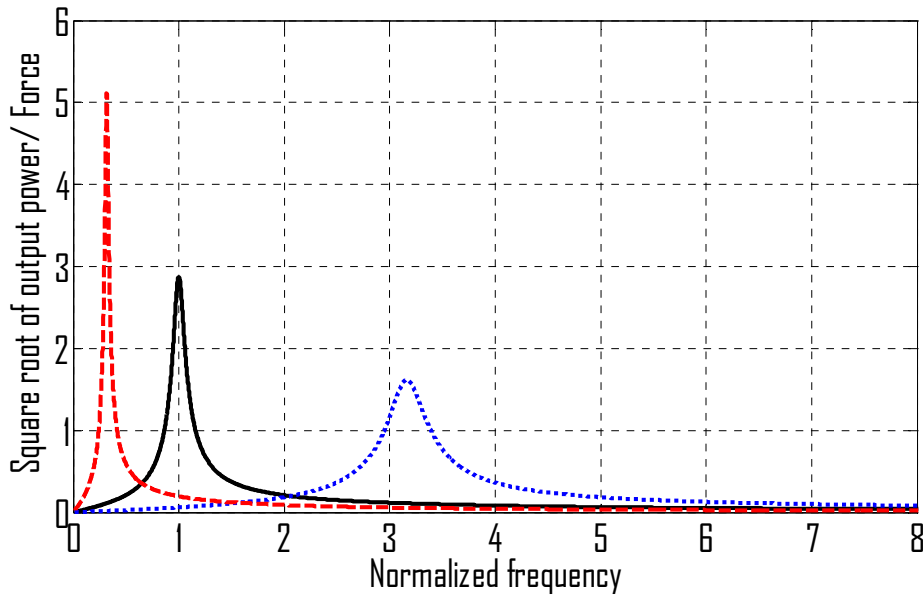


Figure 5.6 Frequency response of force to square root of the output power for single-mass vibration energy harvester, where the nominal parameters are,  $m_s=1, k_s=1, \zeta_e = 5\%, \zeta_m = 0.5\%$ . (Black solid: nominal  $k_s$ ; blue dot:  $k_s$  decreased 10 times; red dashed:  $k_s$  increased 10 times).

Remark 3: If the parasitic mechanical damping of the energy harvester is ignorable small ( $\zeta_m \ll \zeta_e$ ), the output power of the harvester is only a function of the mass ( $I_p = 1/2m_1$ ), independent of the spring stiffness and the damping due to the electric load. To gain some physical insight on this observation, we plot the frequency responses for different spring stiffness from force to square root of the output power ( $\sqrt{E[c_e \dot{x}_s^2]}$ ) in Figure 4.6. The natural frequency increases with the increase of stiffness. The area under the curve  $\sqrt{E[c_e \dot{x}_s^2]}/F_{ex}$  decreased at lower frequency is compensated by the area increased at higher frequency; as a result the mean value of output power, which is the integration of  $E[c_e \dot{x}_s^2]S_F$  doesn't change. It should be noted that in the Figure 4.6 we keep the damping ratios constant  $\zeta_e = 5\%$ ,  $\zeta_m = 0.5\%$ .

## 5.2 Electromagnetic Shunt TMDs

The classic TMD works in the following way: when resonance of the absorber system ( $m_1, k_1, c_1$ ) is tuned near the resonance of the primary system, it will counteract the disturbance and draw away vibration energy from the primary system, resulting in reduced vibration near resonant frequency. An R-L-C circuit can also introduce a resonance which can be coupled primary structure, as shown in Figure 4.7(b). This is so called electromagnetic shunt TMD, in which an electromagnetic transducer of inductance “ $L$ ” (such as a linear electromagnetic motor, or a rotary motor and a linear-to-rotational motion mechanism) is installed in parallel with the spring. A capacitor of capacitance “ $C$ ” and a resistive load of resistance “ $R$ ” are used to shunt the electromagnetic transducer to form the resonant R-L-C circuit. The idea of the electromagnetic shunt TMD is similar as the shunted piezoelectric resonant damping, initially observed by Forward in 1979 (Forward, 1979). Hagood and Flotow (1991) analytically interpreted and experimentally proved that piezoelectric shunt with an  $R-L$  circuit will act as a TMD. Extensive research has been done for shunted piezoelectric damping, as seen in the reviewers (Lesieutre, 1998; Moheimani, 2003) and references therein. Behrens *et al.* (2003 and 2006) first presented the concept of electromagnetic resonant damping with an  $R-C$  shunt circuit, and obtained the tuning parameters were numerically. Inoue *et al.* (2008) obtained the analytical expressions of the optimal tuning frequency and damping, or parameter of  $L$  and  $R$ , by following a similar approach of Den Hartog's fixed point method of classic TMD. Most recently, Zuo and Cui (2012) proposed the electromagnetic shunt series TMD with enhanced performance, in which a mechanical resonance and an electrical R-L-C resonance in series are tuned close to that of the



primary structure. Decentralized  $H_2$  control and gradient based numerical method were used to obtain the optimal parameters for vibration control and energy harvesting.

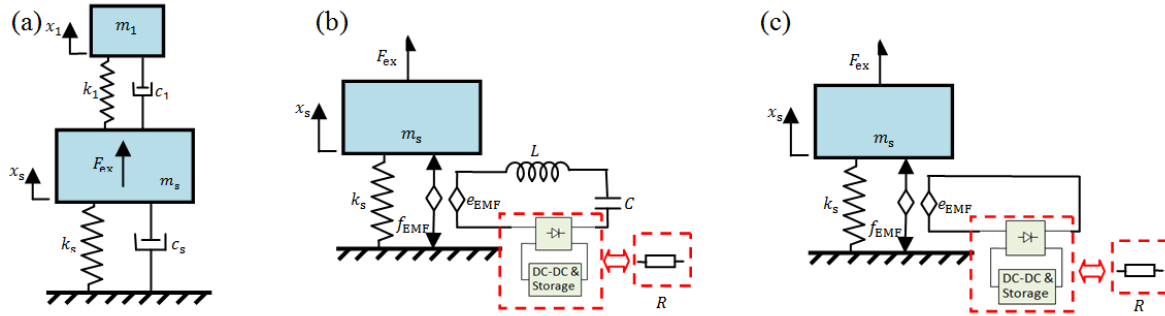


Figure 5.7 (a) classic TMD, (b) electromagnetic TMD or vibration energy harvester shunted with an  $RLC$  circuit, (c) a traditional electromagnetic vibration harvester with an resistive charging circuit.

The section is to derive the closed-form solutions to the  $H_2$  and  $H_\infty$  optimization of the electromagnetic shunt TMD system, which provides ready-to-use analytical formula convenient for practical TMD application. The traditional vibration energy harvester typically has resistive load or a resistive charging circuit (the dc-to-dc charging circuit can be modeled as a resistor “ $R$ ” (Lefeuvre *et al.*, 2007) under moderate assumption), as shown in Figure 4.7(c). Enhanced energy harvesting performance can be achieved with the resonant charging circuit at harmonic excitations.

Figure 4.7(b) shows the electromagnetic resonant shunt damper, in which a resonant charging or load circuit is used here instead of a traditional resistive load. Using the fixed-point theory, Inoue *et al.* (2008) optimized the parameters, such as  $R$  and  $C$  circuit for vibration suppression. We will derive the closed-form expression of the optimal parameters for both vibration suppression and energy harvesting, with  $H_2$  and  $H_\infty$  optimization criteria. Since many vibration energy harvesting systems are composed of a vibrating mass connected with electromagnetic transducer and a spring, the analytical solutions are very valuable for the parameters design of electromagnetic shunt TMD and energy harvesting circuits.

The governing equation of the system shown in Figure 4.7(b) under external force excitation  $F_{ex}$  can be expressed as:

$$\begin{cases} m_s \ddot{x}_s + k_s x_s = F_{\text{ex}} - k_t i \\ k_e \dot{x}_s = R i + L \frac{di}{dt} + \frac{1}{C} \int i dt \end{cases} \quad (4.16)$$

The resonant frequency of the circuit is  $\omega_e = 1/\sqrt{LC}$ .

And the equivalent electrical damping ratio contributed by the circuit is

$$\zeta_e = \frac{R}{2L\omega_e} \quad (4.17)$$

The relation of the external force  $F_{\text{ex}}$  and the displacement  $X_s$  can be obtained as:

$$\left[ m_s s^2 + k_s + \frac{k_e k_t s^2}{L s^2 + R s + \frac{1}{C}} \right] X_s = F_{\text{ex}} \quad (4.18)$$

From Equation (4.18), we can see that if the electromagnetic transducer circuit has inductance only ( $R=0, C=\infty$ ),  $\frac{k_e k_t}{L}$  will act as an additional stiffness to  $k_s$ . Therefore, we define

$$\mu_k = \frac{k_e k_t}{L k_s} \quad (4.19)$$

as the coefficient of electromagnetic mechanical coupling. It is actually a stiffness ratio (the electromagnetic mechanical coupling stiffness  $\frac{k_e k_t}{L}$  divided by the stiffness of the original system), which plays a similar role as the mass ratio in the classic TMD. If  $R=0$  and  $L=0$ ,  $k_e k_t C$  will act as an additional mass. However, when comparing with the relationship between the displacement  $X_s$  and  $F_{\text{ex}}$  relation of the classic TMD,

$$\left[ m_s s^2 + k_s + \frac{m_1 s^2 (k_1 + c_1 s)}{m_1 s^2 + c_1 s + k_1} \right] X_s = F_{\text{ex}} \quad (4.20)$$

It can be seen that the resonant shunt electromagnetic TMD (Equation 4.18) is not exactly the same as the classic TMD (Equation 4.20), except for the case when  $R=0$  where the single mass with L-C shunted electromagnetic transducer is equivalent to un-damped TMD system.

Using fixed-point method, Inoue *et al.* (2008) obtained the analytical expressions of the optimal tuning ratio and damping ratio for such electromagnetic shunt TMD:

$$\begin{cases} f^{\text{opt}} = \frac{\omega_e}{\omega_s} = \frac{\sqrt{1/LC}}{\omega_s} = \sqrt{1 - \frac{\mu_k}{2}} \\ \zeta^{\text{opt}} = \frac{R}{2L\omega_e} \approx \frac{1}{2} \sqrt{\frac{3\mu_k}{2 - \mu_k}} \end{cases} \quad (4.21)$$

where  $f = \omega_e/\omega_s$  is the tuning ratio,  $\omega_s = \sqrt{k_s/m_s}$  is natural frequency of primary system.

## 5.2.1 $H_2$ Optimal Solutions

### 5.2.1.1 $H_2$ Optimization for Vibration Mitigation

If the system is subject to the random vibration input,  $H_2$  norm is better for evaluating the performance, since it is the RMS value of the performance under unit white noise input (Zhou *et al.*, 1995). In this Section,  $H_2$  optimization method minimizes the RMS value of displacement  $\langle x_s^2 \rangle$  of the primary system under the Gaussian white noise input force  $F_{ex}$ .

The performance index is defined as:

$$PI = \frac{k_s E[x_s^2]}{S_F} = \frac{k_s \langle x_s^2 \rangle}{S_F} \quad (4.22)$$

where  $S_F$  is the uniform power spectrum density of the Gaussian white noise input. The RMS value of the displacement of the primary mass can be obtained as:

$$\langle x_s^2 \rangle = S_F \int_{-\infty}^{\infty} \left| \frac{X_s}{F_{ex}} \right|^2 d\omega \quad (4.23)$$

Substituting Equation (4.23) into Equation (4.22), the performance index can be expressed as:

$$PI = \int_{-\infty}^{\infty} \left| \frac{X_s}{F_{ex}/k_s} \right|^2 d\omega \quad (4.24)$$

The transfer function from  $F_{ex}/k_s$  to  $X_s$  can be written as:

$$TF = \frac{X_s}{F_{ex}/k_s} = \frac{\frac{k_s}{m_s}(S^2 + \frac{R}{L}S + \frac{1}{CL})}{S^4 + \frac{R}{L}S^3 + (\frac{1}{CL} + \frac{k_s}{m_s} + \frac{k_e k_t}{m_s L})S^2 + \frac{k_s R}{m_s L}S + \frac{k_s}{m_s LC}} \quad (4.25)$$

The dimensionless form of which is:

$$\frac{X_s}{F_{ex}/k_s} = \frac{(j\alpha)^2 + 2\zeta_e f(j\alpha) + f^2}{(j\alpha)^4 + 2\zeta_e f(j\alpha)^3 + (f^2 + 1 + \mu_k)(j\alpha)^2 + 2\zeta_e f(j\alpha) + f^2} \quad (4.26)$$

where  $\alpha$  is the excitation frequency ratio,  $\alpha = \omega/\omega_s$ . The integral of Equation (4.24) can be solved using residue theorem, the general result of which can be expressed as.

$$I = \int_{-\infty}^{\infty} \left| \frac{B_0 + i\omega B_1 + (i\omega)^2 B_2 + (i\omega)^3 B_3}{A_0 + i\omega A_1 + (i\omega)^2 A_2 + (i\omega)^3 A_3 + (i\omega)^4 A_4} \right|^2 d\omega = \omega_n \int_{-\infty}^{\infty} \left| \frac{B_0 + i\bar{\omega} B_1 + (i\bar{\omega})^2 B_2 + (i\bar{\omega})^3 B_3}{A_0 + i\bar{\omega} A_1 + (i\bar{\omega})^2 A_2 + (i\bar{\omega})^3 A_3 + (i\bar{\omega})^4 A_4} \right|^2 d\bar{\omega} \quad (4.27)$$

$$I = \pi \left( \frac{A_0 B_3^2 (A_0 A_3 - A_1 A_2) + A_0 A_1 A_4 (2B_1 B_3 - B_2^2) - A_0 A_3 A_4 (B_1^2 - 2B_0 B_2) + A_4 B_0^2 (A_1 A_4 - A_2 A_3)}{A_0 A_4 (A_0 A_3^2 + A_1^2 A_4 - A_1 A_2 A_3)} \right) \quad (4.28)$$

Hence, the performance index can be finally obtained as a function of the two parameters, tuning ratio  $f$  and damping ratio  $\zeta_e$

$$PI = \frac{1 + 4\zeta_e^2 f^2 - 2f^2 + f^4 + \mu_k f^2}{4\zeta_e f \mu_k} \quad (4.29)$$

In order to minimize the performance index  $PI$ , the derivative of  $PI$  in respect to  $\zeta_e$  and  $f$  should be equal to zero, which means:  $\frac{\partial PI}{\partial \zeta_e} = 0$  and  $\frac{\partial PI}{\partial f} = 0$ . Then the following two equations are obtained.

$$\begin{cases} 4\zeta_e^2 f^2 + 2f^2 - f^4 - f^2 \mu_k - 1 = 0 \\ 4\zeta_e^2 f^2 + 3f^4 - 1 + f^2 \mu_k - 2f^2 = 0 \end{cases} \quad (4.30)$$

Solve Equation (4.30) for the optimal tuning ratio  $f$  and the optimal  $\zeta_e$ . Since the stiffness ratio  $\mu_k$  is usually small ( $\mu_k \ll 2$ ), the final result of  $H_2$  optimal tuning rule is obtained as:

$$\begin{cases} f^{\text{opt}} = \sqrt{\frac{2 - \mu_k}{2}} \\ \zeta_e^{\text{opt}} = \sqrt{\frac{\mu_k^2 - 4\mu_k}{8\mu_k - 16}} \end{cases} \quad (4.31)$$

The corresponding optimal values of  $R$  and  $C$  are:

$$\begin{cases} C^{\text{opt}} = \frac{1}{\omega_s^2 f^{\text{opt}2} L} \\ R^{\text{opt}} = 2L \zeta_e^{\text{opt}} f^{\text{opt}} \omega_s \end{cases} \quad (4.32)$$

The tuning ratio is the same as the one obtained using fixed-point theory while the damping ratio is not. And at the optimal condition, the performance index  $PI^{\text{opt}}$  is:

$$PI^{\text{opt}} = \frac{\mu_k}{2\sqrt{\mu_k^2 - 4\mu_k}} \quad (4.33)$$

### 5.2.1.2 $H_2$ Optimization for Energy Harvesting

For energy harvesting, we would like to maximize the average electrical power on the resistive load  $R$ . The instant power is:

$$P(t) = Ri(t)^2 \quad (4.34)$$

When the system is subjected to the excitation with a uniform power spectrum  $S_F$ , the performance index is defined as:

$$PI_P = \frac{k_s E[P]}{S_F} = \frac{k_s E[Ri(t)^2]}{S_F} = \frac{k_s \langle Ri(t)^2 \rangle}{S_F} \quad (4.35)$$

From the dynamic equations of the system, we can obtain the dimensionless transfer function from  $F_{ex}/k_s$  to the current  $i$

$$TF = \frac{i}{F_{ex}/k_s} = \frac{\frac{k_e(j\alpha)^2}{L}}{(j\alpha)^4 + 2\zeta_e f(j\alpha)^3 + (f^2 + 1 + \mu_k)(j\alpha)^2 + 2\zeta_e f(j\alpha) + f^2} \quad (4.36)$$

Similarly, by using residue theorem, performance index can be finally obtained as:

$$PI_P = \frac{R\omega_s k_e^2 / L^2 k_s^2}{4\zeta_e f \mu_k} = \frac{1}{2m_s} \quad (4.37)$$

As we can see from Equation (4.37), the performance index is independent of the two parameters, electrical damping ratio  $\zeta_e$  and tuning ratio  $f$ . The results concur with the conclusions in (Tang and Zuo, 2012), where additional DOF is not necessary better for energy harvesting under white noise type of random force excitation. Equation (4.37) also suggests that the energy harvesting performance under random disturbance depends on the property of the harvester itself only, and the resonant circuit will not have additional gain.

## 5.2.2 $H_\infty$ Optimal Solutions

### 5.2.2.1 $H_\infty$ Optimization for Vibration Mitigation

As found by Asami *et al.* (2002) for the classic TMD, the fixed point tuning rule doesn't concede with the optimal  $H_\infty$  solution which minimize the maximal peak in the frequency domain. In  $H_\infty$  optimization criterion, the purpose is to minimize the maximum amplitude factor, also known as  $H_\infty$  norm. Numerical  $H_\infty$  control has appeared in literature for the optimization of classic TMD. Asami *et al.* (2002) gives the analytical solution to the optimal result using  $H_2$  and  $H_\infty$  control.

The similar methodology can be used for the optimization of electromagnetic shunt TMD. In order to minimize the  $H_\infty$  norm, the condition can be expressed as:

$$\begin{cases} \frac{\partial \left| \frac{X_S}{F_{ex}/k_s} \right|^2}{\partial \zeta} = 0 \\ \frac{\partial \left| \frac{X_S}{F_{ex}/k_s} \right|^2}{\partial \alpha^2} = 0 \\ \left| \frac{X_S}{F_{ex}/k_s} \right|_{\alpha=\alpha_A} = \left| \frac{X_S}{F_{ex}/k_s} \right|_{\alpha=\alpha_B} \end{cases} \quad (4.38)$$

where  $\zeta$  is damping ratio,  $\alpha$  is force frequency ratio and  $\alpha_A$  and  $\alpha_B$  are two resonant frequencies. The first two equations of Equations (4.38) results from the observation that the resonant amplitudes happens at a certain combination of  $\zeta$  and  $\alpha$ . There are two combinations related to two resonant amplitudes, represented as  $(\zeta_A, \alpha_A)$  and  $(\zeta_B, \alpha_B)$ . The last equation indicates the two resonant amplitudes are at equally height. The last equation of Equation (38) cannot be solved analytically. In (Asami, *et al.*, 2002), it is solved using the perturbation method approximately. In this section an indirect method is used to obtain the close-form optimal parameters. It should be noted that this method is used in (Nishihara and Asami, 2002) for the optimization of traditional TMD and the methodology is referred during the analysis.

For simplification, we re-define Intermediate parameter,

$$\bar{\zeta}_e = \frac{R}{2L\omega_s}, \zeta_e = \bar{\zeta}_e/f \quad (4.39)$$

Hence, the transfer function can be re-written as:

$$TF(\alpha) = \frac{X_S}{F_{ex}/k_s} = \frac{(j\alpha)^2 + 2\bar{\zeta}_e(j\alpha) + f^2}{(j\alpha)^4 + 2\bar{\zeta}_e(j\alpha)^3 + (f^2 + 1 + \mu_k)(j\alpha)^2 + 2\bar{\zeta}_e(j\alpha) + f^2} \quad (4.40)$$

The objective is to minimize the  $H_\infty$  norm of  $TF(\alpha)$ . Since the system is a second order system, it is reasonable to assume that  $T(\alpha)$  has two distinct resonance points, with frequency ratio  $\alpha_A$  and  $\alpha_B$  (Nishihara and Asami, 2002).

$X = \alpha^2$  is defined for simplicity, the square of the  $H_\infty$  norm can be expressed as:  $h = \frac{N(X)}{D(X)}$ ,

where

$$N(X) = (f^2 + X)^2 + 4\bar{\zeta}_e^{-2}X \quad (4.41)$$

$$D(X) = [X^2 - (f^2 + 1 + \mu_k)X + f^2]^2 + 4\bar{\zeta}_e^{-2}X(1 - X)^2 \quad (4.42)$$

By assuming that when the system is optimized, the square of the magnification factor is  $h^{\text{opt}}$  at point A and B, we can have the following equation:

$$h^{\text{opt}} = \frac{N(X)}{D(X)} \Big|_{X=X_A \text{ or } X_B} \quad (4.43)$$

Beside, the tangents of the frequency response at point A and B are horizontal, hence

$$\frac{N'(X)D(X) - N(X)D'(X)}{D^2(X)} \Big|_{X=X_A \text{ or } X_B} = 0 \quad (4.44)$$

Equations (4.43) and (4.44) are simplified to

$$N(X) - h^{\text{opt}}D(X) \Big|_{X=X_A \text{ or } X_B} = 0 \quad (4.45)$$

$$N'(X) - h^{\text{opt}}D'(X) \Big|_{X=X_A \text{ or } X_B} = 0 \quad (4.46)$$

Therefore the following equation is defined as

$$F \equiv D - N/h^{\text{opt}} \quad (4.47)$$

which has two double roots:  $X_A = \alpha_A^2$  and  $X_B = \alpha_B^2$ .

Equation (4.47) can be simplified as:

$$F(X) = X^4 + b_1X^3 + b_2X^2 + b_3X + b_4 \quad (4.48)$$

where

$$\begin{cases} b_1 = -2(f^2 + 1 + \mu_k - 2\bar{\zeta}_e^{-2}) \\ b_2 = f^4 + 4f^2 + 2f^2\mu_k + 2\mu_k + \mu_k^2 - 8\bar{\zeta}_e^{-2} + r^2 \\ b_3 = -2(f^4 + \mu_k f^2 + r^2 f^2 - 2r^2 \bar{\zeta}_e^{-2}) \\ b_4 = r^2 f^4 \end{cases} \quad (4.49)$$

and  $r = \sqrt{1 - 1/h^{\text{opt}}}$  ( $h^{\text{opt}} > 1, 0 < r < 1$ ) is introduced for simplicity (Nishihara and Asami, 2002).

Since  $F(X) \equiv 0$  has two double roots, we can express  $b_i (i=1, \dots, 4)$  in a different form according to Vieta's theorem (Nishihara and Asami, 2002):

$$\begin{cases} b_1 = -2(X_A + X_B) \\ b_2 = X_A^2 + 4X_A X_B + X_B^2 \\ b_3 = -2X_A X_B (X_A + X_B) \\ b_4 = X_A^2 X_B^2 \end{cases} \quad (4.50)$$

By eliminating  $X_A$  and  $X_B$ , Equation (4.50) can be reduced to the following equations

$$b_1 \sqrt{b_4} - b_3 = 0 \quad (4.51)$$

$$\frac{b_1^2}{4} + 2\sqrt{b_4} - b_2 = 0 \quad (4.52)$$

By substitute Equation (4.50) into Equation (4.51), we can have

$$f_{T1} = (2rf^2 - 2r^2)\bar{\zeta}_e^2 - [rf^4 + rf^2 + \mu_k rf^2 - (f^4 + \mu_k f^2 + r^2 f^2)] \quad (4.53)$$

By solving Equation (4.53)  $\bar{\zeta}_e$  can be expressed as a function of  $f$ .

$$\bar{\zeta}_e = \sqrt{\frac{f^2[r(f^2+1+\mu_k)-(f^2+\mu_k+r^2)]}{2r(f^2-r)}} \quad (4.54)$$

Substitute Equation (4.54) into (4.52) to eliminate  $\bar{\zeta}_e$  and define  $Y = f^2$  for simplicity, Equation (4.52) can be expressed in the following form:

$$f_{T2} = c_0 Y^4 + c_1 Y^3 + c_2 Y^2 + c_3 Y + c_4 \quad (4.55)$$

where

$$\begin{cases} c_0 = 1 - r^2 \\ c_1 = 4r^3 - 2\mu_k r^2 - 4r + 2\mu_k \\ c_2 = -\mu_k^2 r^2 + \mu_k^2 + 4\mu_k r^3 - 4\mu_k r - 6r^4 + 6r^2 \\ c_3 = 2\mu_k^2 r^3 - 2\mu_k^2 r^2 - 2\mu_k r^4 + 2\mu_k r^2 + 4r^5 - 4r^3 \\ c_4 = r^4 - r^6 \end{cases} \quad (4.56)$$

Since Equation (4.55) has repeated real roots, the following matrix is equivalent to zero (Nishihara and Asami, 2002).

$$\begin{vmatrix} c_0 & c_1 & c_2 & c_3 & c_4 & 0 & 0 \\ 0 & c_0 & c_1 & c_2 & c_3 & c_4 & 0 \\ 0 & 0 & c_0 & c_1 & c_2 & c_3 & c_4 \\ 4c_0 & 3c_1 & 2c_2 & c_3 & 0 & 0 & 0 \\ 0 & 4c_0 & 3c_1 & 2c_2 & c_3 & 0 & 0 \\ 0 & 0 & 4c_0 & 3c_1 & 2c_2 & c_3 & 0 \\ 0 & 0 & 0 & 4c_0 & 3c_1 & 2c_2 & c_3 \end{vmatrix} = 0 \quad (4.57)$$

Equation (4.57) will reduce to:



$$64r^4 - 16\mu_k r^3 + (11\mu_k^2 + 16\mu_k - 64)r^2 + (2\mu_k^3 - 20\mu_k^2 + 32\mu_k)r + 2\mu_k^3 - 4\mu_k^2 = 0 \quad (4.58)$$

Since  $\mu_k$  is very small, Equation (4.58) can be reduced to:

$$4r^3 - \mu_k r^2 + (\mu_k - 4)r + 2\mu_k = 0 \quad (4.59)$$

Solving Equation (4.59), we can obtain the root as:

$$r = \frac{1}{2} + \frac{\mu_k}{8} + \frac{\sqrt{\mu_k^2 - 24\mu_k + 16}}{8} \quad (4.60)$$

Since Equation (4.55) has only even-ordered terms, it can be factorized into the following form (Nishihara and Asami, 2002):

$$f_2 = (1 - r^2)(f^2 + 2Pf + P^2 + Q^2)(f^2 - 2Pf + P^2 + Q^2)(f^2 - P^2)^2 \quad (4.61)$$

where

$$P = \sqrt{\frac{2r - \mu_k + \sqrt{(2r - \mu_k)^2 + 12r^2}}{6}} \quad (4.62)$$

$$Q = \sqrt{\frac{2\mu_k - 4r + \sqrt{(2r - \mu_k)^2 + 12r^2}}{3}} \quad (4.63)$$

Hence, the final  $H_\infty$  optimal parameters of frequency tuning and damping can be expressed as

$$f^{\text{opt}} = \sqrt{\frac{2r^{\text{opt}} - \mu_k + \sqrt{(2r^{\text{opt}} - \mu_k)^2 + 12r^{\text{opt}2}}}{6}} \quad (4.64)$$

$$\bar{\zeta}_e^{\text{opt}} = \sqrt{\frac{f^{\text{opt}2} [r^{\text{opt}} (f^{\text{opt}2} + 1 + \mu_k) - (f^{\text{opt}2} + \mu_k + r^{\text{opt}2})]}{2r^{\text{opt}} (f^{\text{opt}2} - r^{\text{opt}})}} \quad (4.65)$$

$$\zeta_e^{\text{opt}} = \sqrt{\frac{r^{\text{opt}} (f^{\text{opt}2} + 1 + \mu_k) - (f^{\text{opt}2} + \mu_k + r^{\text{opt}2})}{2r^{\text{opt}} (f^{\text{opt}2} - r^{\text{opt}})}} \quad (4.66)$$

where the optimal  $r^{\text{opt}}$  can be expressed by Equation (4.60).

The corresponding optimal values of  $R$  and  $C$  are:

$$\begin{cases} C^{\text{opt}} = \frac{1}{\omega_s^2 f^{\text{opt}2} L} \\ R^{\text{opt}} = 2L \zeta_e^{\text{opt}} \omega_e \end{cases} \quad (4.67)$$

### 5.2.2.2 $H_\infty$ Optimization for Energy Harvesting

For the traditional energy harvester, composed of one mass and an electromagnetic transducer shunt with resistive load and negligible inductance, as shown in Figure 4.7(c), the dimensionless power under external harmonic force can be expressed as (Stephen, 2006; Tang and Zuo, 2011b)

$$\overline{P_{\text{ave}}}(\alpha, \zeta_e) = \frac{Ri^2}{F^2/\omega_s m_s} = \frac{\zeta_e \alpha^2}{(1-\alpha^2)^2 + 4\zeta_e^2 \alpha^2} \quad (4.68)$$

By taking the derivative of Equation (4.68)  $\partial \overline{P_{\text{ave}}}/\partial \alpha$ , and setting it to zero, we can further conclude that the maximal harvesting power happens when the excitation frequency is the same as the system natural frequency ( $\alpha = 1$ ). The global maximum of dimensionless harvesting power can be expressed as:

$$\overline{P_{\text{ave}}}^{\text{max}} = \frac{1}{4\zeta_e} \quad (4.69)$$

When the electromagnetic transducer is shunt with  $R$ - $L$ - $C$  resonant circuit, as shown in Figure 4.7(b), the dimensionless power will be:

$$\overline{P_{\text{ave}}} = \frac{Ri^2}{F_{\text{ex}}^2/\omega_s m_s} = \frac{\mu_k \zeta_e f \alpha^4}{(\alpha^4 - (f^2 + 1 + \mu_k)\alpha^2 + f^2)^2 + 4\zeta_e^2 f^2 \alpha^2 (1-\alpha^2)^2} \quad (4.70)$$

From Equation (4.70), we can see the optimal equivalent damping ratio  $\zeta_e$  for maximizing the average energy harvesting rate can be expressed by Equation (4.71), for a given excitation frequency  $\alpha$  and tuning ratio  $f$ .

$$\zeta_e^{\text{opt}}(\alpha) = \frac{\alpha^4 - (f^2 + 1 + \mu_k)\alpha^2 + f^2}{2f\alpha(1-\alpha^2)} \quad (4.71)$$

By substituting the optimal electric damping  $\zeta_e$  in Equation (4.71) to Equation (4.70), the maximum power can be expressed as:

$$\overline{P_{\text{ave}}}^{\text{max}}(\alpha) = \frac{\mu_k \alpha^3}{4[\alpha^4 - (f^2 + 1 + \mu_k)\alpha^2 + f^2](1-\alpha^2)} \quad (4.72)$$

It can be seen from Equations (4.71) and (4.72), the optimal damping and energy harvesting rate can be infinity in an extreme case, when  $\alpha = 1$  and  $\zeta_e = \infty$ . This extreme case is different from the extreme case of traditional energy harvester ( $\alpha = 1$  and  $\zeta_e = 0$  suggested in Equation 4.69.) One sees that the resonant circuit can be used to achieve larger energy harvesting rate.

Similar observation has been found for the dual-mass vibration energy harvester, where the resonance introduced by auxiliary spring-mass system can enhance the energy harvesting rate (Tang and Zuo, 2011b).

Table 4.1 summarized the results of the optimal parameters of both classic and electromagnetic shunt TMD using different methods.

Table 5.1 Optimum parameters for vibration mitigation.

		$H_2$	$H_\infty$	Fixed point method
Electromagnetic shunt TMD	Tuning ratio $f$	$\sqrt{1 - \frac{\mu_k}{2}}$	$\sqrt{\frac{2r^{\text{opt}} - \mu_k + \sqrt{(2r^{\text{opt}} - \mu_k)^2 + 12r^{\text{opt}2}}}{6}}$ **	$\sqrt{1 - \frac{\mu_k}{2}}$
	Damping ratio $\zeta$	$\sqrt{\frac{\mu_k^2 - 4\mu_k}{8\mu_k - 16}}$	$\sqrt{\frac{r^{\text{opt}}(f^{\text{opt}2} + 1 + \mu_k) - (f^{\text{opt}2} + \mu_k + r^{\text{opt}2})}{2r^{\text{opt}}(f^{\text{opt}2} - r^{\text{opt}})}}$	$\frac{1}{2} \sqrt{\frac{3\mu_k}{2 - \mu_k}}$
Classic TMD	Tuning ratio $f$	$\frac{1}{1 + \mu} \sqrt{\frac{2 + \mu}{2}}$	$\frac{1}{1 + \mu}$	$\frac{1 + \mu}{2}$
	Damping ratio $\zeta$	$\sqrt{\frac{\mu(3\mu + 4)}{8(1 + \mu)(2 + \mu)}}$	$\sqrt{\frac{3\mu}{8(1 + \mu)}}$	$\sqrt{\frac{3\mu}{8(1 + \mu)^3}}$

$$**r^{\text{opt}} = \frac{1}{2} + \frac{\mu_k}{8} + \sqrt{\frac{\mu_k^2 - 24\mu_k + 16}{8}}$$

### 5.2.3 A Case Study and Sensitivity Analysis

Figure 4.8 shows the frequency response of the corresponding optimized TMDs with 1% mass ratio (classic TMD) or 1% stiffness ratio (electromagnetic TMD). It shows that the electromagnetic shunt TMD can achieve similar vibration mitigation performance as the classic TMD.

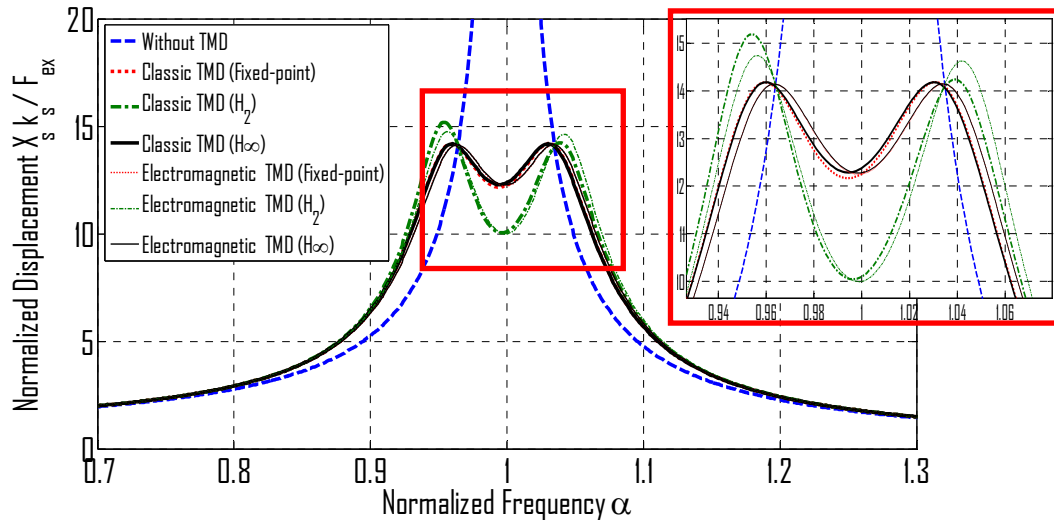


Figure 5.8 The frequency responses of the classic TMD of mass ratio 1% and electromagnetic shunt TMD of stiffness ratio 1% .

In practice it is difficult to make perfect tuning, or some parameter may change after some time. Figures 4.9 and 4.10 show how the vibration mitigation performance will change with the uncertainties of parameters of the primary mechanical system and the resonant circuit. It can be concluded that the vibration performance is sensitive to the frequency tuning ratio, namely the value of the capacitor, but it not sensitive to the damping ratio, namely the value of the resistor. It should be noted Figures 4.9 and 4.10 are based on the optimal value obtained by  $H_\infty$  optimization. Similar observation is true for the design obtained by  $H_2$  optimization.

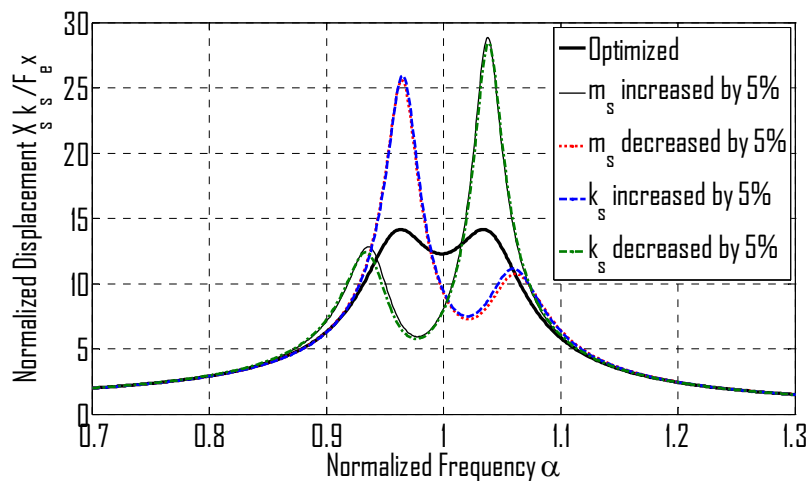


Figure 5.9 Sensitivity of vibration suppression of the  $H_\infty$  optimal electromagnetic shunt TMD to the parameter changes of the primary systems.

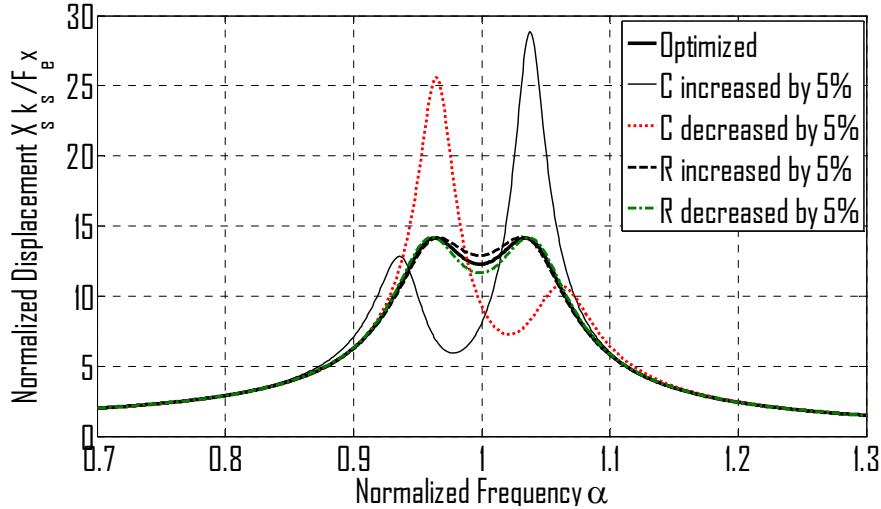


Figure 5.10 Sensitivity of vibration suppression of the  $H_\infty$  optimal electromagnetic shunt TMD to the parameter changes of electrical resonant circuit.

To illustrate the effectiveness of the resonance circuit on the energy harvesting rate, we plot the frequency responses from force to harvesting power in Figure 4.11. It should be noted that in Figure 4.11 the tuning ratio is set as  $f=0.95$  (not optimal) and the damping ratio is 2%. In comparison with the traditional energy harvesting with resistive load, this figure clearly shows that the maximum energy harvesting rate of the electromagnetic TMD with resonant circuit is much larger than the one with only restive load.

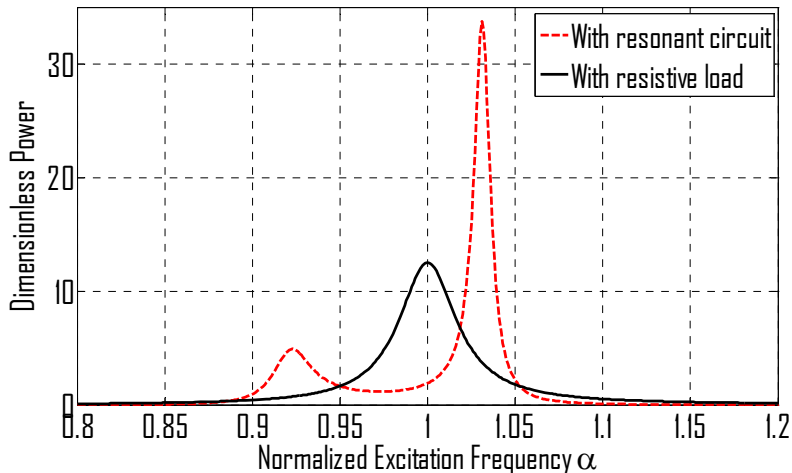


Figure 5.11 Frequency responses of the energy harvesting power of electromagnetic TMD with resonant circuit and with restive load, where stiffness ratio  $\mu_k = 1\%$ , frequency tuning ratio  $f = 0.95$ , damping  $\zeta_e = 2\%$ .

### 5.3 Electricity-Generating TMD

One of the realizations of simultaneous vibration control and energy harvesting from tall buildings is to replace the energy-dissipative element of the TMD with electromagnetic transducers, which is called electricity-generating TMD. However, the electromagnetic transducers and the energy harvesting circuit, the modeling of which is an essentially a RL circuit, will introduce extra dynamics into the system, which has significant influence on the vibration mitigation performance. This section investigates the influence, by optimizing the parameters. We found that the electricity-generating TMD can provide better vibration mitigation performance than the classic TMD and similar performance as the three-element TMD while harvesting the vibration energy at the same time.

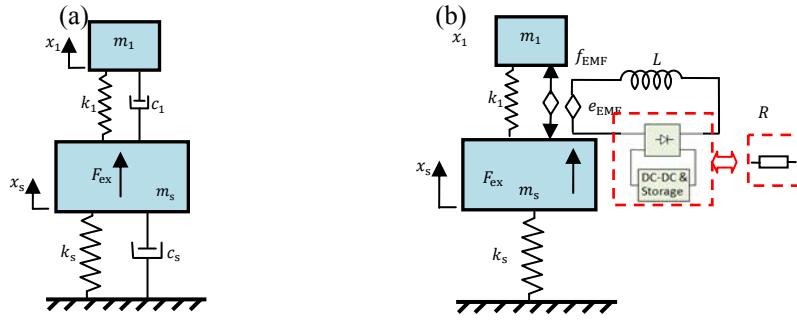


Figure 5.12 (a). classic TMD, (b). electricity-generating TMD.

#### 5.3.1 Electricity-generating TMD

Figure 1(b) shows the electricity-generating TMD, in which the inductance of the electromagnetic transducer is noted as  $L$ , and the resistive load or a resistive charging circuit is noted as  $R$  (the dc-to-dc charging circuit can be modeled as a resistor “ $R$ ” (Lefevre *et al.*, 2007) under moderate assumption). The governing equation of the system shown in Figure 4.12(b) under external force excitation  $F_{ex}$  can be expressed as:

$$\begin{cases} m_1 \ddot{x}_1 + k_1(x_1 - x_s) = -k_t i \\ m_s \ddot{x}_s + k_s x_s = k_1(x_1 - x_s) + F_{ex} + k_t i \\ k_e(\dot{x}_1 - \dot{x}_s) = Ri + L \frac{di}{dt} \end{cases} \quad (4.73)$$

From equation (4.73), the relation of the external force  $F_{\text{ex}}$  and the displacement  $X_s$  can be obtained as:

$$TF = \frac{X_s}{F_{\text{ex}}/k_s} = \frac{(j\alpha)^3 + 2\zeta_e(j\alpha)^2 + (1+\mu_k)f^2(j\alpha) + 2f^2\zeta_e}{(j\alpha)^5 + 2\zeta_e(j\alpha)^4 + (f^2+1+\mu f^2+f^2(1+\mu)\mu_k)(j\alpha)^3 + (2\zeta_e f^2 + 2\mu\zeta_e f^2 + 2\zeta_e)(j\alpha)^2 + (1+\mu_k)f^2(j\alpha) + 2f^2\zeta_e} \quad (4.74)$$

where  $\alpha$  is the excitation frequency ratio,  $\alpha = \omega/\omega_s$ ,  $\zeta_e = \frac{R}{2L\omega_s}$  is the damping ratio,  $\mu = \frac{m_1}{m_s}$  is the mass ratio,  $f = \omega_1/\omega_s$  is the tuning ratio,  $\omega_s = \sqrt{k_s/m_s}$  is the natural frequency of the primary system,  $\omega_1 = \sqrt{k_1/m_1}$  is the natural frequency of the TMD,  $\mu_k = \frac{k_e k_t}{L k_1}$  is the coefficient of electromagnetic mechanical coupling. It is actually a stiffness ratio (the electromagnetic mechanical coupling stiffness  $\frac{k_e k_t}{L}$  divided by the stiffness of the TMD system).

### 5.3.2 Parameters Optimization

In this Section,  $H_2$  optimization method minimizes the RMS value of displacement  $\langle x_s^2 \rangle$  of the primary system under the Gaussian white noise input force  $F_{\text{ex}}$ .

The performance index is defined as:

$$PI = \frac{k_s E[x_s^2]}{S_F} = \frac{k_s \langle x_s^2 \rangle}{S_F} \quad (4.75)$$

where  $S_F$  is the uniform power spectrum density of the Gaussian white noise input,  $E[\cdot]$  stands for the means square value, and  $\langle \cdot \rangle$  stands for the temporal average, respectively. The RMS value of the displacement of the primary mass can be obtained as:

$$\langle x_s^2 \rangle = S_F \int_{-\infty}^{\infty} \left| \frac{X_s}{F_{\text{ex}}} \right|^2 d\omega \quad (4.76)$$

Substituting Equation (4.76) into Equation (4.75), the performance index can be expressed as:

$$PI = \int_{-\infty}^{\infty} \left| \frac{X_s}{F_{\text{ex}}/k_s} \right|^2 d\omega \quad (4.77)$$

The integral of Equation (4.77) can be solved using residue theorem or the general formula described in (Nishihara and Asami, 2002).

Hence, the performance index can be finally obtained as a function of the three parameters, tuning ratio  $f$  and damping ratio  $\zeta_e$ , and stiffness ratio  $\mu_k$

$$PI = \frac{(4\mu^2 f^4 + 8\mu f^4 + 4f^4 - 4\mu f^4 - 8f^2 + 4)\zeta_e^2 + (\mu + 1)f^4 - 2(\mu_k + 1)f^2 + 2\mu_k f^4 + \mu_k^2 f^4 + 2\mu\mu_k f^4 + 1}{2\mu\mu_k\zeta_e f^2} \quad (4.78)$$

In order to minimize the performance index  $PI$ , the derivative of  $PI$  in respect to  $\mu_k$ ,  $\zeta_e$  and  $f$  should be equal to zero, which means:  $\frac{\partial PI}{\partial \mu_k} = 0$ ,  $\frac{\partial PI}{\partial \zeta_e} = 0$  and  $\frac{\partial PI}{\partial f} = 0$ . Then the following three equations are obtained.

$$\begin{cases} f^4((1 + \mu)[(\mu_k + 1)^2 + 4\zeta_e^2(1 + \mu)]) - 4\zeta_e^2 - 1 = 0 \\ f^4((1 + \mu)[\mu_k^2 - 4\zeta_e^2(1 + \mu) - 1]) + 2f^2[(2\mu + 4)\zeta_e^2 + 1] - 4\zeta_e^2 - 1 = 0 \\ f^4((1 + \mu)[4\zeta_e^2(1 + \mu) - (\mu_k + 1)^2]) + 2f^2[\mu_k + 1 - (2\mu + 4)\zeta_e^2] + 4\zeta_e^2 - 1 = 0 \end{cases} \quad (4.79)$$

Solve Eq. (4.79) for the stiffness ratio  $\mu_k$ , optimal tuning ratio  $f$  and the optimal  $\zeta_e$ . The final result of  $H_2$  optimal tuning rule is obtained as:

$$\begin{cases} f^{\text{opt}} = \sqrt{1 - \sqrt{\frac{\mu}{1 + \mu}}} \\ \mu_k^{\text{opt}} = 2[\mu + \sqrt{\mu(1 + \mu)}] \\ \zeta_e^{\text{opt}} = \frac{\mu + \sqrt{\mu(1 + \mu)}}{\sqrt{2[1 - (\frac{\mu}{1 + \mu} - 1)^2](1 + \mu)^2}} \end{cases} \quad (4.80)$$

Hence the corresponding optimal  $k_1, L$  and  $R$  can be expressed as:

$$\begin{cases} k_1^{\text{opt}} = (1 - \sqrt{\frac{\mu}{1 + \mu}}) m_s \omega_s^2 \\ L^{\text{opt}} = \frac{k_e k_t}{2k_1^{\text{opt}}[\mu + \sqrt{\mu(1 + \mu)}]} \\ R^{\text{opt}} = 2\omega_s L^{\text{opt}} \frac{\mu + \sqrt{\mu(1 + \mu)}}{\sqrt{2[1 - (\frac{\mu}{1 + \mu} - 1)^2](1 + \mu)^2}} \end{cases} \quad (4.81)$$

It should be noted that the optimal damping ratio  $f^{\text{opt}}$  and optimal stiffness ratio  $\mu_k^{\text{opt}}$  is the same as the three-element TMD, the optimal parameter of which is (Nishihara and Asami, 2002):



$$\begin{cases} f^{\text{opt}} = \sqrt{1 - \sqrt{\frac{\mu}{1+\mu}}} \\ k^{\text{opt}} = 2[\mu + \sqrt{\mu(1+\mu)}] \\ \zeta_1^{\text{opt}} = \sqrt{\mu[(1+\mu) - \frac{3+2\mu}{2} \sqrt{\frac{\mu}{1+\mu}}]} \end{cases} \quad (4.82)$$

where the stiffness ratio is defined as  $k = k_a/k_1$  and damping ratio is  $\zeta_1 = c_1/2m_1\omega_1$ . The configuration of three-element TMD is shown in Figure 4.13. However, the optimal damping ratios of these two TMDs are different.

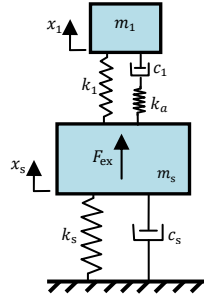


Figure 5.13 Three-element TMD.

Figure 4.14 shows the frequency response of the corresponding optimized TMDs and electricity-generating TMD with 1% mass ratio. It should be noted that the optimal parameters for the classic TMD is (Asami, *et al*, 2002):

$$\begin{cases} f^{\text{opt}} = \frac{1}{1+\mu} \sqrt{\frac{2+\mu}{2}} \\ \zeta_1^{\text{opt}} = \sqrt{\frac{\mu(4+3\mu)}{8(1+\mu)(2+\mu)}} \end{cases} \quad (4.83)$$

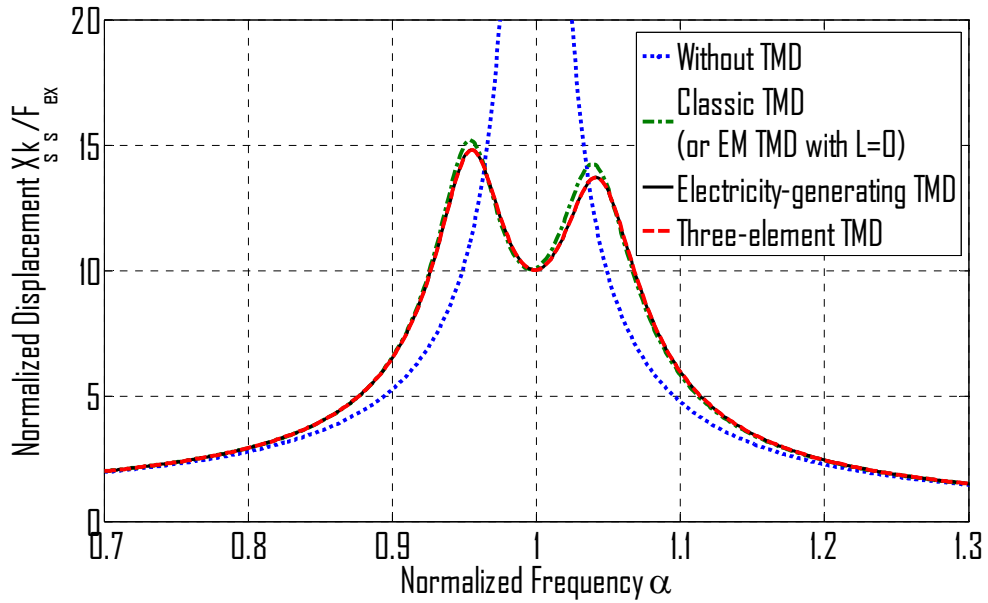


Figure 5.14 The frequency responses of the building with different TMDs of mass ratio  $\mu = 1\%$  .

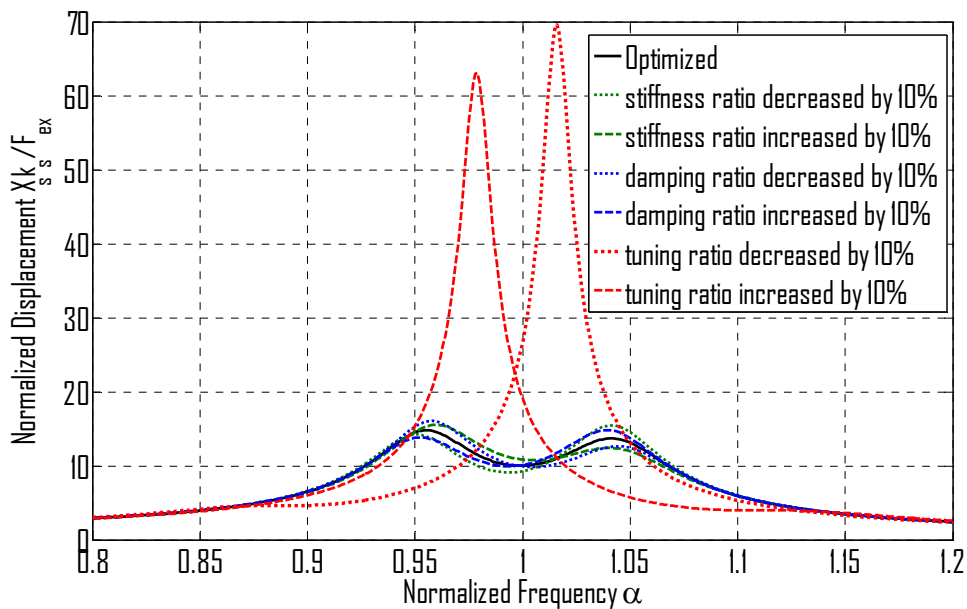


Figure 5.15 Sensitivity of vibration suppression of the optimal electricity-generating TMD to the parameter changes.

It shows that the electricity-generating TMD can achieve better vibration mitigation performance than the classic TMD, and similar performance as the three-element TMD. The optimal

parameters for different TMD are listed in Table 4.2. It should be noted the definition of the damping ratio for the electricity-generating TMD and three-element TMD are different.

Table 5.2 Optimal parameters with H<sub>2</sub> optimization for different TMDs.

	Electricity- generating TMD	Three- element TMD	Classic TMD
Tuning ratio	0.9489	0.9489	0.9926
Stiffness ratio	0.2210	0.2210	N/A
Damping ratio	0.5654	0.0927	0.0498

In practice it is difficult to make perfect tuning, or some parameter may change after some time. Figure 4.15 shows how the vibration mitigation performance will change with the parameters change. It can be concluded that the vibration performance is sensitive to the frequency tuning ratio, but it not sensitive to the damping ratio, namely the value of the resistor or the stiffness ratio which is the inductance of the electromagnetic motor. It will give some feasibility when design the electricity-generating TMD in practice.

## 5.4 Series TMDs

### 5.4.1 Description of Series TMDs

The classic TMD usually needs very bulky mass in order to be effective and it may need large dissipative device. Another disadvantage of classic TMD is that it is very sensitive (i.e., not robust) to parameter changes of the systems. When the parameters of the primary systems change a small amount, the performance of TMDs will be greatly defected. It is called off-tuning problem. Hence, in order to reduce the auxiliary mass and damping coefficient and increase the effectiveness and robustness, various types of TMD have been proposed and investigated by researchers, such as parallel multiple TMDs (Setareh *et al.*, 2006; Yamaguchi and Hampornchai, 1993), multi-degree-of-freedom TMDs (Zuo and Nayfeh, 2002) and three- or four-element TMDs (Snowdon, 1974). As pointed by Zuo (2009), the series TMDs with two auxiliary masses of total mass ratio of 5% can appear to have 31–66% more mass than the classical TMD, and it can perform better than the optimal parallel ten TMDs of the same total mass ratio. Especially, the

series TMDs (Zuo, 2009) have many advantages over classic TMD in passive, active and semi-active realization. In this chapter, the series TMD will be optimized and analyzed using decentralized control method. A design example is presented to show the effectiveness and robustness of series TMD.

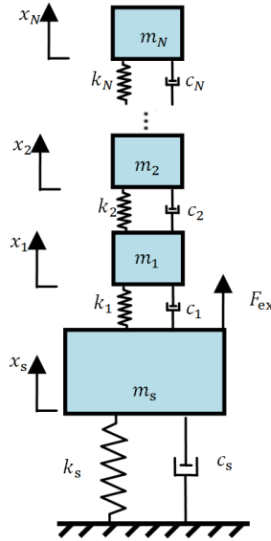


Figure 5.16 Building structure with series TMDs when subjected to wind load disturbance (Zuo, 2009).

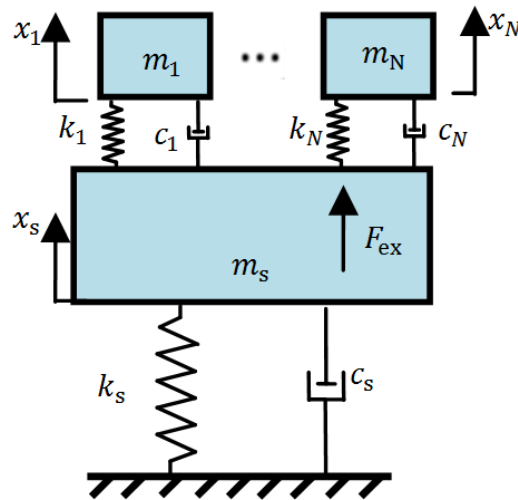


Figure 5.17 Building structure with parallel TMDs.

Series TMD consists of multiple masses and absorbers connected in series to the primary structure, as shown in Figure 4.16 The primary system of mass  $m_s$  is supported on the base with a spring of stiffness  $k_s$  and a damper of damping coefficient  $c_s$ . Auxiliary masses  $m_1, m_2, \dots, m_N$

are attached to the primary system in series, with the spring of stiffness  $k_1, k_2, \dots, k_N$  and dampers of damping coefficient  $c_1, c_2, \dots, c_N$ . The primary system is subjected to the disturbance of external wind load or ground motion. It was found that the optimized passive series TMDs are more effective and robust than other types of TMDs with the same mass ratio, such as the classic TMD, parallel multiple TMDs (Figure 4.17), multi-DOF and three- or four-element TMD (Zuo, 2009).

The advantages of series TMDs over other types of TMDs for random excitation can also be seen from the frequency responses and impulse responses shown in Figure 4.18 and 4.19 (Zuo, 2009). Especially, the series two TMDs have better vibration mitigation performance than the optimal parallel ten TMDs of the same total mass ratio. Hence, in this chapter we will further investigate series TMD for the application of simultaneous energy harvesting and vibration control.

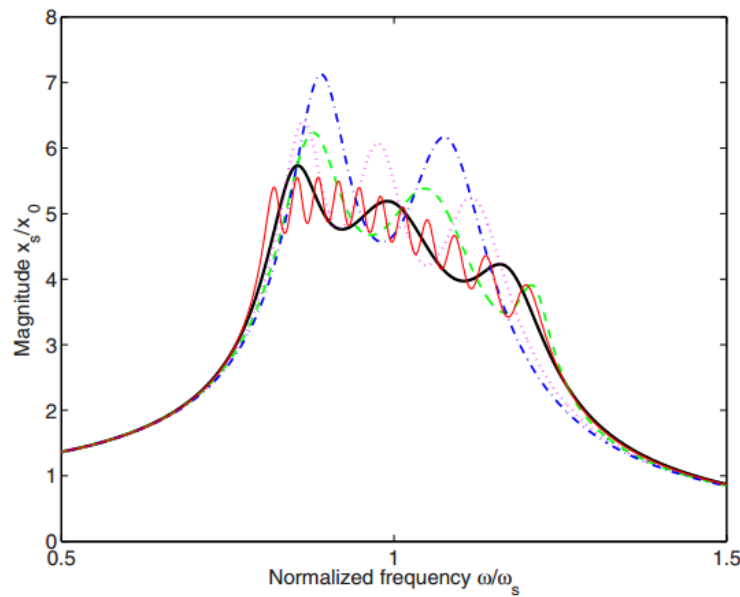


Figure 5.18 Frequency responses of  $H_2$  optimal series two TMDs with  $m_1/(m_1+m_2)=0.909$  (thicker solid)  $H_2$  optimal parallel two TMDs (dot) and parallel ten TMDs (thinner solid)  $H_2$  optimal 2DOF TMD of (dash) and  $H_2$  optimal classic TMD (dash-dot) where the total mass of absorbers is  $0.05m_s$  for all the cases, and the primary system has no damping (Zuo, 2009).

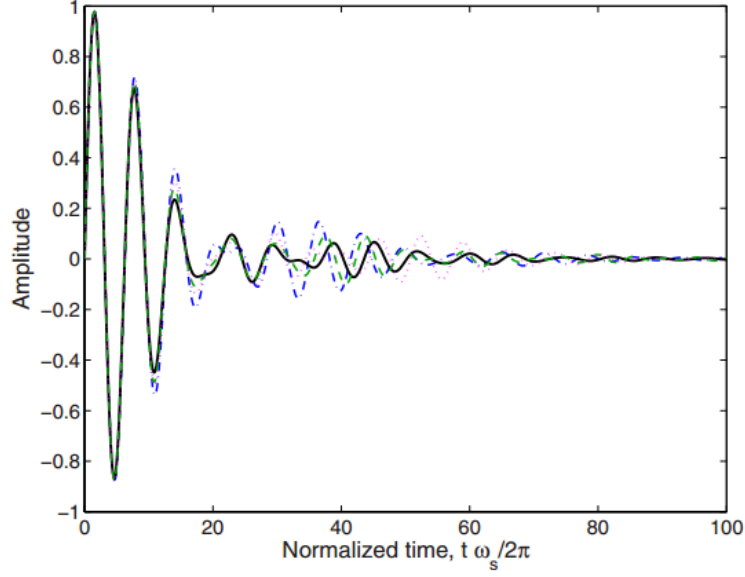


Figure 5.19 Impulse responses of systems with  $H_2$  optimal series two TMDs with  $m_1/(m_1+m_2)=0.909$  (thicker solid)  $H_2$  optimal parallel two TMDs (dot) and parallel ten TMDs (thinner solid)  $H_2$  optimal 2DOF TMD of (dash) and  $H_2$  optimal classic TMD (dash-dot) where the total mass of absorbers is  $0.05m_s$  for all the cases, and the primary system has no damping (Zuo, 2009).

#### 5.4.2 Review of Parameter Optimization with Decentralized Control Method

Under external disturbance  $F_{ex}$ , the dynamics of the passive series TMDs as shown in Figure 4.16 can be expressed as:

$$\begin{aligned}
 m_s \ddot{x}_s + c_s \dot{x}_s + k_s x_s &= u_1 + F_{ex} \\
 m_i \ddot{x}_i &= -u_i + u_{i+1}, \quad 1 \leq i < N \\
 m_N \ddot{x}_N &= -u_N
 \end{aligned} \tag{4.84}$$

where  $u_i, i=1, 2, \dots, N$ , is the passive “control” force generated by the  $i$ -th spring and damper.

The system Equation (4.84) can be further expressed in matrix form:

$$M_x \ddot{X} + C_x \dot{X} + K_x X = B_d F + B_u u \tag{4.85}$$

where  $X = [x_s, x_1, x_2, \dots, x_N]^T$ . Equation (4.85) can be further expressed in the state space form:

$$\begin{aligned}
 \dot{x} &= Ax + B_1 w + B_2 u \\
 z &= C_1 x + D_{11} w + D_{12} u
 \end{aligned} \tag{4.86}$$

$$y = C_2x + D_{21}w$$

where  $z$  is the performance output, which can be the vibration amplitude, velocity, or acceleration of the primary system. The “measurement output”  $y$  is a vector of the relative displacements and velocities between these bodies. Here we take it as the vibration amplitude  $z = x_s$ . The “control input”  $u$  is a vector constructed using the “measurement output”  $y$  with a block diagonal matrix:

$$u = \begin{pmatrix} u_1 \\ u_2 \\ \vdots \\ u_N \end{pmatrix} = \begin{bmatrix} k_1 & c_1 & & & \\ & & k_2 & c_2 & \\ & & & & \ddots \\ & & & & & k_N & c_N \end{bmatrix} y = F_d \quad (4.87)$$

The parameter optimization of  $k_i$  and  $c_i$  is casted to a decentralized control problem by obtaining the optimal static feedback gain matrix  $F_d$  in block diagonal form (Zuo and Nayfeh, 2002). The physical insight is to take the springs (and dampers) as relative displacement (and velocity) sensors and force actuators. The spring stiffness  $k_i$  is the feedback gain of the relative displacement, and the damping coefficient  $c_i$  is the feedback gain of the relative velocity. This is zero-order decentralized control with output feedback, as shown in Figure 4.20. Moreover, all the entries of the matrix  $F_d$  often need to be nonnegative so that we can implement them with passive mechanical elements. Therefore, the parameter optimization of the series TMDs system becomes an optimal feedback control problem: by designing the optimal control gain matrix  $F_d$  in Equation (4.87), the optimal parameters of spring stiffness and damping coefficients are obtained.

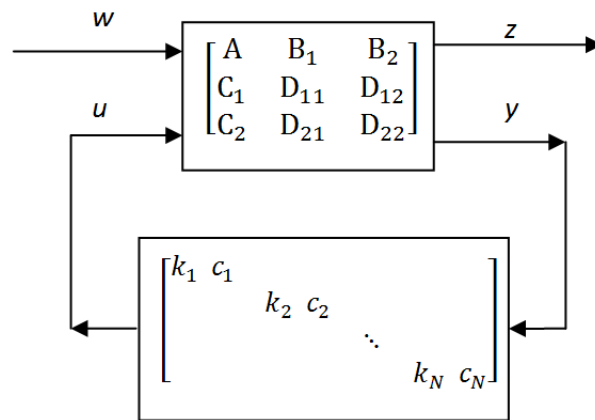


Figure 5.20 Casting the optimization to control problem (Zuo, 2009).

The detailed optimization result can be seen in reference (Zuo, 2009). In order to evaluate the performance of the series TMD, simulations are carried out based on the parameters of building with 730 tons TMD, 0.146 Hz natural frequency,  $\mu=0.78\%$  where  $\mu$  is ratio of total auxiliary masses over the modal mass of the primary system, which is typically 1/3 of the building mass (Higashino and Aizawa, 1993). It should be noted that, the optimal stiffness and damping coefficient in Section 4.4 are given in terms of dimensionless tuning ratio  $f_i$  and damping ratio  $\zeta_i$  as in Equations (4.88) and (4.89).

$$f_i = \sqrt{\frac{k_i / \sum_{j=i}^N m_j}{k_s / m_s}} \quad (4.88)$$

$$\zeta_i = \frac{c_i}{2\sqrt{k_i \sum_{j=i}^N m_j}} \quad i = 1, 2 \quad (4.89)$$

### 5.4.3 Results of $H_\infty$ Optimal Series TMDs

Decentralized  $H_\infty$  control is used to reduce the peak of the frequency response, where the optimal parameters of series TMDs can be found in the chart of reference (Zuo and Nayfeh, 2002). For the classic TMD, the  $H_\infty$  optimal parameters of the stiffness and damping coefficient are very close that that obtained with Den Hartog's fixed point method (1947).

The detailed optimal parameters for a building with 730 tons TMD, 0.146 Hz natural frequency, 0.78% modal mass ratio are listed in Table 4.3. The performances in the frequency domain of four TMDs are shown in Figure 4.21. As we can see from the figure, with the same mass ratio, the optimal series can provide much better vibration mitigation performance. The peaks are further reduced by 22.2% with the utilization of series TMDs. In order to provide the same performance of series TMDs with mass ratio of 0.78%, classic TMD with mass ratio of 1.29% is needed. On the other hand, in order to achieve same performance of the classic TMD with 0.78% mass ratio, series TMDs with only 0.47% mass ratio is sufficient, as compared in Figure 4.21. That means the mass of the classic TMD in the building can be reduced from 730 tons to 440 tons, which will reduce the relevant cost in real implementation. Another interesting characteristic of series TMDs is that its optimal damping coefficient is significant smaller than the one of classic TMD. It is reduced from 71.05kN·s/m to 2.40 kN·s/m when having the same mass ratio of 0.78%, which is only 3.38% of the optimal one in classic TMD. Similarly findings also exist in series TMDs optimized using decentralized  $H_2$  control method.



Table 5.3 Parameters and performances of  $H_\infty$  optimal TMDs.

System	Mass Ratio	Mass(kg)	Tuning ratio	Damping ratio	Frequency peak
Classic TMD	$\mu=0.78\%$	$m_I=7.30 \times 10^5$	$f_I=0.9923$	$\zeta_1=0.053$ ( $c_1=71.05 \text{ kN} \cdot \text{s/m}$ )	16.1
Classic TMD	$\mu=1.29\%$	$m_I=7.30 \times 10^5$	$f_I=0.9056$	$\zeta_1=0.069$ ( $c_1=150.66 \text{ kN} \cdot \text{s/m}$ )	12.5
Series TMDs	$\mu=0.78\%$	$m_I=7.16 \times 10^5$ $m_2=1.36 \times 10^4$	$f_I=0.9968$ $f_2=0.9873$	$\zeta_1=0, \zeta_2=0.0971$ ( $c_1=0, c_2=2.40 \text{ kN} \cdot \text{s/m}$ )	12.5
Series TMDs	$\mu=0.47\%$	$m_I=7.22 \times 10^5$ $m_2=0.78 \times 10^4$	$f_I=0.9980$ $f_2=0.9929$	$\zeta_1=0, \zeta_2=0.072$ ( $c_1=0, c_2=1.03 \text{ kN} \cdot \text{s/m}$ )	16.1

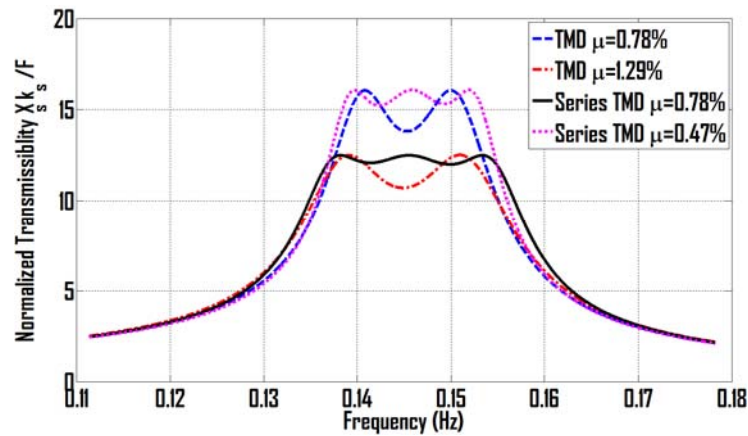


Figure 5.21 Frequency responses of structure with series and classic TMDs with parameters optimized by  $H_\infty$  control method.

#### 5.4.4 Results of $H_2$ Optimal Series TMDs

Decentralized  $H_2$  control method is used to minimize the RMS of the output index under random excitation. The physical insight of the decentralized  $H_2$  control is to minimize the area under the frequency response curve, or to minimize the energy of impulse response. The parameters of  $H_2$  optimal series TMDs using decentralized  $H_2$  control method can be found in the chart of reference (Zuo, 2009). For the classic TMD, the optimal parameters with  $H_2$  optimization are already analytically solved by Asmai *et al.* (2002), as shown by Equations (4.90) and (4.91).

Detailed parameters of different TMDs for building with 730 tons TMD, 0.146 Hz natural frequency, 0.78% modal mass ratio are listed in Table 4.4.

Table 5.4 Parameters and performances of  $H_2$  optimal TMDs.

System	Mass Ratio	Mass(kg)	Tuning ratio	Damping ratio	$H_2$ norm
<b>Classic TMD</b>	$\mu=0.78\%$	$m_I=7.30 \times 10^5$	$f_I=0.9120$	$\zeta_1=0.0440$ ( $c_1=58.63 \text{ kN} \cdot \text{s/m}$ )	$4.1 \times 10^{-8}$
<b>Classic TMD</b>	$\mu=1.15\%$	$m_I=7.30 \times 10^5$	$f_I=0.9095$	$\zeta_1=0.0534$ ( $c_1=104.54 \text{ kN} \cdot \text{s/m}$ )	$3.7 \times 10^{-8}$
<b>Series TMDs</b>	$\mu=0.78\%$	$m_I=7.18 \times 10^5$ $m_2=1.14 \times 10^4$	$f_I=1$ $f_2=0.9923$	$\zeta_1=0, \zeta_2=0.0760$ ( $c_1=0, c_2=1.58 \text{ kN} \cdot \text{s/m}$ )	$3.8 \times 10^{-8}$
<b>Series TMDs</b>	$\mu=0.50\%$	$m_I=7.23 \times 10^5$ $m_2=0.73 \times 10^4$	$f_I=1$ $f_2=0.9950$	$\zeta_1=0, \zeta_2=0.0615$ ( $c_1=0, c_2=0.82 \text{ kN} \cdot \text{s/m}$ )	$4.2 \times 10^{-8}$

$$f_1 = \frac{1}{1+\mu} \sqrt{\frac{2+\mu}{2}} \quad (4.90)$$

$$\zeta_1 = \sqrt{\frac{\mu(4+3\mu)}{8(2+\mu)(1+\mu)}} \quad (4.91)$$

Similarly, the frequency responses of classic TMD and series TMDs optimized by  $H_2$  control method are compared in Figure 4.22. With the same vibration mitigation performance the mass ratio is reduced by 35.9%, from 0.78% to 0.5%. That means the mass of the classic TMD in the building can be reduced from 730 tons to 468 tons. In order to provide the same performance as series TMDs with mass ratio 0.78%, the classic TMD needs 1.15% mass ratio, which is 1.47 times more.

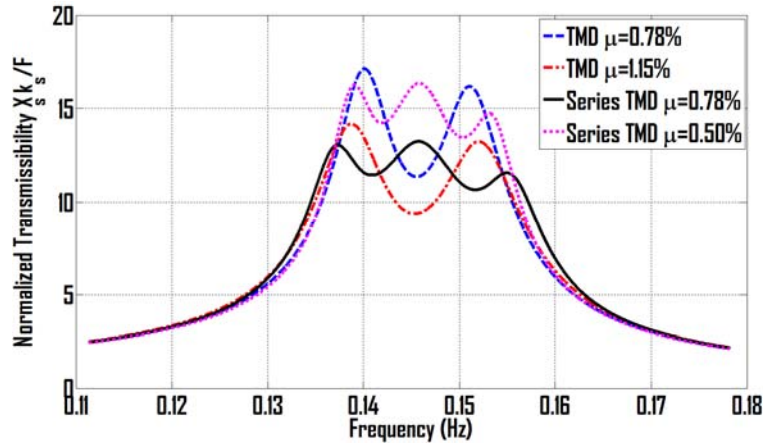


Figure 5.22 Frequency responses of structures with series and classic TMDs with parameters optimized by  $H_2$  control method.

## 5.5 Electromagnetic Series TMDs

### 5.5.1 Description and Optimization of Electromagnetic Series TMD

We just discussed about the concept of series TMD and reported the enhanced effectiveness and robustness. However, Ni *et al.* (2011) examined the application of series TMD for vibration control and energy harvesting of wind-induced tall building vibration. They concluded that two masses with 1.62% total mass ratio can attain the vibration control effect of the classic TMD of 2% mass, while harvest similar amount of energy. However, the motion stroke is a few times larger, as shown in Figure 4.23.

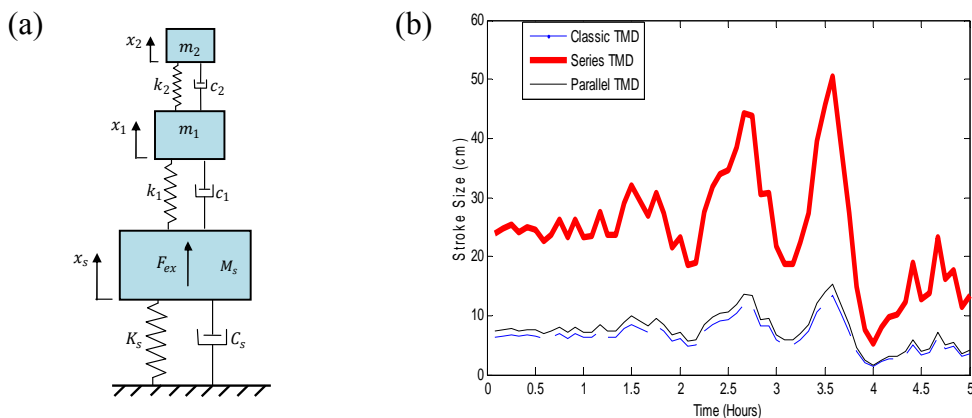


Figure 5.23 (a) Double-mass series TMD, (b) the RMS stroke the double-mass series TMD is several times larger than the classic TMD or parallel TMDs (Ni *et al.*, 2011)

Hence, we proposed a so called electromagnetic series TMD, which is composed of an electromagnetic transducer, resonant shunt circuit, and the classic TMD, as shown in Figure 4.24. The electromagnetic transducer is shunted with a R-L-C circuit instead of a resistive circuit. It should be noted that the difference between the electromagnetic series TMD and electricity-generating TMD discussed in Section 4.3 is the additional capacitor. This R-L-C circuit will create another resonant, which will benefit the vibration energy harvesting and mitigation performance. In this section, the parameter of the electromagnetic series TMD will be optimized.

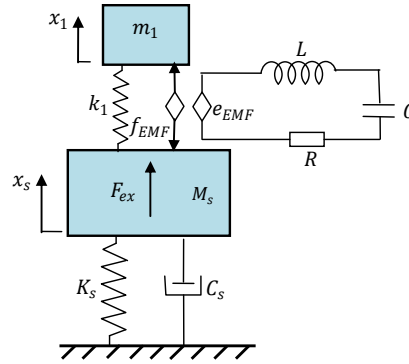


Figure 5.24 The electromagnetic series TMD.

To optimize the tuning parameters, we reformulate the problem of parameter optimization as a control problem, by following the procedure proposed in (Zuo, 2009). As seen in Figure 4.25, we replace the force of the spring  $k_1$  as control input

$$u_1 = k_1(x_1 - x_s) \quad (4.92)$$

and the voltage on the resistor and capacitor as control input

$$u_2 = \frac{1}{C}q + R\dot{q} \quad (4.93)$$

Hence the control  $u$  can be expressed as

$$u = \begin{pmatrix} u_1 \\ u_2 \end{pmatrix} = \begin{bmatrix} k_1 & 0 & 0 \\ 0 & 1/C & R \end{bmatrix} y = F_d y \quad (4.94)$$

Thus, the parameter optimization problem can be solved by using the decentralized control; once the block-diagonal feedback matrix  $F_d$  is obtained, we can obtain the tuning parameters  $k_1$ ,  $C$ , and  $R$ .

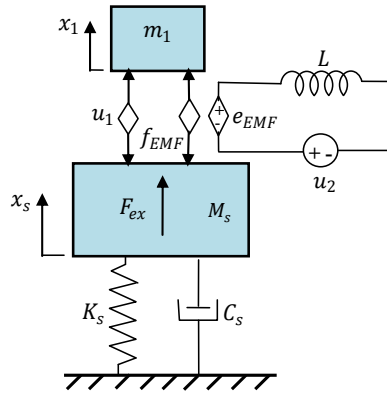


Figure 5.25 The modeling of electromagnetic shunt series TMD as a control problem, where the control force  $u_1$  is generated by the spring  $k_1$ , and the control force  $u_2$  is produced by the electrical capacitor  $C$  and the resistor  $R$ .

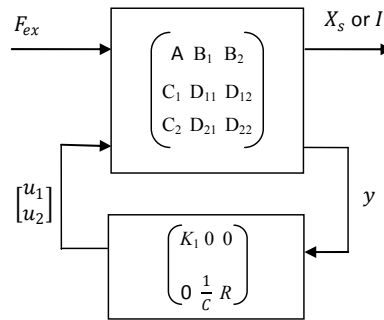


Figure 5.26 The parameter optimization of the mechanical and electrical components in the framework of decentralized control.

The optimization procedure is similar to that in (Zuo, 2009), which we omit here. For energy harvesting, we would like to maximize the average electrical powder on the resistive load  $R$ . Since instant power is

$$P(t) = R \dot{q}(t)^2 \quad (4.95)$$

one may realize that this problem is very tricky, because the power involve one state variable  $\dot{q}$  and one feedback gain  $R$  in the matrix  $F_d$ , and the problem is maximization instead of minimization in  $H_2$  control.

To solve the problem of maximizing the energy, we rewrite the objective function as

$$P_{ave} = R(\dot{q}_{RMS})^2 = R \|H_{w \rightarrow \dot{q}}\|_2^2 \quad (4.96)$$

Hence two factors can be observed: (1) The objective function  $P_{ave}$  can be evaluated for a given feedback matrix  $F_d$  (composed of  $k_1$ ,  $C$ , and  $R$ ) by calculating the system  $H_2$  norm from  $w$  to the electrical current,  $\|H_{w \rightarrow \dot{q}}\|_2$ . (2) The gradient of  $P_{ave}$  with respect to the block-diagonal feedback matrix  $F_d$  can be evaluated using the chain rule

$$\frac{\partial P_{ave}}{\partial F_d} = R \frac{\partial \|H_{w \rightarrow z}\|_2^2}{\partial F_d} + \frac{\partial R}{\partial F_d} \|H_{w \rightarrow z}\|_2^2 \quad (4.97)$$

where  $\frac{\partial \|H_{w \rightarrow z}\|_2^2}{\partial F_d}$  can be obtained using the expression in (Zuo, 2009), and  $\frac{\partial R}{\partial F_d}$  can be obtained from Equation (4.97) as  $\frac{\partial R}{\partial F_d} = \begin{bmatrix} 0 & 0 & 0 \\ 0 & 0 & 1 \end{bmatrix}$ .

Therefore, we can use the gradient based methods (Bertsekas, 1995) to obtain the block-diagonal feedback matrix  $F_d$  that maximize the electrical power harvested. Please note the system stability can be ensured if we replace  $F_d$  as  $\begin{bmatrix} \bar{k}_1^2 & 0 & 0 \\ 0 & 1/\bar{C}^2 & \bar{R}^2 \end{bmatrix}$ , and the gradient can be modified correspondingly.

### 5.5.2 A Case Study and Sensitivity Analysis

In this session we take the Taipei 101 tower as case study, and illustrate the electromagnetic shunt series TMD for energy harvesting and vibration control. Results are presented in comparison with the dual-functional TMDs with classic one mass and two masses in series.

Taipei 101 is one of the tallest building in the world (449.2m to roof, and 509.2m to spire). A TMD of 660 metric tonnes (728 short tons) is suspended on the top of the building from the 92nd to the 87th floor to suppress the wind induced vibration. Up to 40KW of energy dissipation (average 15-20KW) has been simulated in a 100-year wind event from one of the eight viscous damping devices between the primary structure and TMD. The TMD is 0.78% of the modal mass, the first natural frequency is 0.146 Hz and inherent damping is 1%. In the case study, the parameters of the classic TMD is designed using the  $H_2$  optimization, and the parameter of series TMDs of total mass ratio 0.78% are obtained using the  $H_2$  design chart in (Zuo, 2009) with the optimal mass distribution  $m_2/(m_1+m_2)=1.56\%$ , as shown in Table 4.5. For the dual functional implementation, the damping  $c_1$  or  $c_2$  can be realized using an electromagnetic transducer shunted with a resistive electrical load.

Table 5.5 Parameters of Taipei 101 tower and the  $H_2$  optimal classic and double-mass series TMDs.

System	Mass (Kg)	Stiffness (N/m)	Damping (N•s/m)
<b>Without TMD</b>	$m_s=8.46e7$	$k_s=7.12e7$	$c_s=1.55e6$ ( $\zeta_s=1\%$ )
<b>Classic TMD</b> $\mu=0.78\%$	$m_s=8.46e7$ $m_1=6.60e5$	$k_s=7.12e7$ $k_1=5.48e5$	$c_s=1.55e6$ $c_1=5.30e4$
<b>Double-mass series TMDs</b> $\mu=0.78\%$	$m_s=8.46e7$ $m_1=6.495e5$ $m_2=1.05e4$	$k_s=7.12e7$ $k_1=5.55e5$ $k_2=8.52e3$	$c_s=1.55e6$ $c_1=0$ $c_2=1.388e3$

### 5.5.2.1 Results of Electromagnetic Shunt Series TMD for Vibration Suppression

We assume the electromagnetic transducer has an inductance  $L=2.5$  Henrys, force constant  $k_t = 150$  N/A, and voltage constant  $k_e = 150$  V/(m/sec). The electromagnetic mechanical coupling stiffness  $\frac{k_e k_t}{L} = 9000$  N/m. We keep  $m_1=6.60e^5$  kg.

The decentralized  $H_2$  control will yield the following matrix to minimize the displacement  $x_s$  under random force input  $F_{ex}$ ,  $\|H_{w \rightarrow z}\|_2=3.707e^{-8}$  m.

$$F_d = \begin{bmatrix} 5.4963e5 & 0 & 0 \\ 0 & 2.0991 & 0.3532 \end{bmatrix}$$

which mean,  $k_{1-opt} = 5.4963 \times 10^5$  N/m,  $C_{opt} = 0.4763$  Farads, and  $R_{opt} = 0.3532 \Omega$ .

The optimal vibration performances, including the vibration amplitude of the building, stroke of the harvester, and harvesting power, of the electromagnetic shunt series TMD are shown in Table 4.6. The normalized frequency response of the building displacement with electromagnetic shunt series TMD is shown in Figure 4.27 in comparison with these of the classic TMD and double-mass series TMD.

Table 5.6 Performances of optimal electromagnetic shunt series TMD in comparison with classic and double-mass series TMDs for Taipei 101\* under unit white-noise force excitation  $F_{ex}$ .

System	Vibration $X_{s-rms}$ (m)	Stroke $\Delta X_{rms}$ (m)	Harvesting* $\sqrt{P_{ave}}$ ( $\sqrt{W}$ )	Dissipation* $\sqrt{c_s  \dot{x}_s _{rms}}$ ( $\sqrt{W}$ )
<b>Without TMD</b>	6.726e-8	-		7.688e-5
<b>Classic TMD</b>	3.892e-8	2.724e-7	6.272e-5	4.445e-5
<b>Double-mass series TMDs</b>	3.704e-8	1.721e-6 ( $\Delta x = x_2 - x_1$ )	6.416e-5	4.234e-5
<b>Electromagnetic shunted series TMD</b>	3.707e-8	3.24e-7 ( $\Delta x = x_1 - x_s$ )	6.417e-5	4.233e-5

\*Note: Harvesting means the energy harvested by the electromagnetic transducer, and dissipation refers to the power dissipated by the inherent damping  $C_s$  of the primary system.

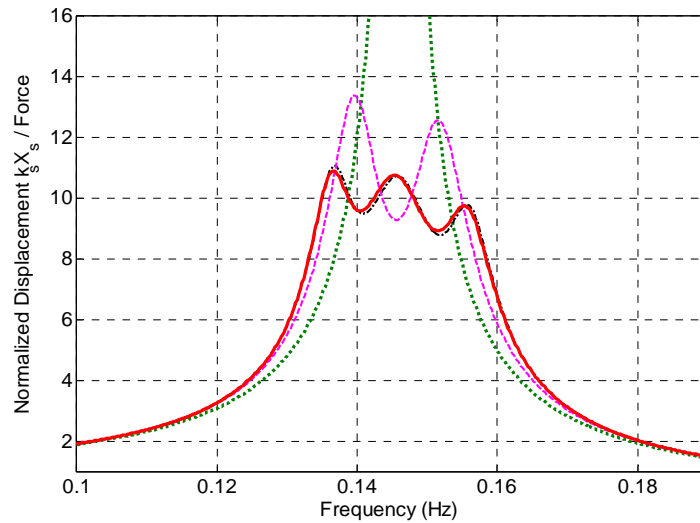


Figure 5.27 The frequency responses of electromagnetic shunt series TMD for Taipei 101 Tower (red solid) in comparison with double-mass TMD (black dash-dot), classic TMD (purple dash), and system without TMD (green dot), where all parameters are optimized to minimize the  $H_2$  norm from external force to the displacement of the primary system.



We see that the vibration control and energy harvesting performances of electromagnetic shunt series TMD are very close to those of double-mass series TMD and are better than the classic TMD. In term of stroke of energy harvester, we see that the double-mass series TMD is 6.3 times as that of classic TMD, but the electromagnetic shunt series TMD is just increased by 19%.

### 5.5.2.2 Results of Electromagnetic Shunt Series TMD for Energy Harvesting

The parameters of stiffness  $k_1$  and the electrical capacitor  $C$  and resistor  $R$  to maximize the harvesting power are also optimized using the gradient based method described. The results are compared with the ones optimized for vibration control, as shown in Table 4.7. The frequency responses from excitation force  $F_{ex}$  to the building displacement  $x_s$  are shown in Figure 4.28. We see that the parameters and performances are very close in these two cases.

Table 5.7 Optimal parameters and performances of electromagnetic shunted series TMDs optimized for vibration control and for energy harvesting under unit white-noise excitation  $F_{ex}$ .

Electromagnetic shunt series TMD System	Stiffness $k_1$ (N/m)	$R$ and $C$ ( $\Omega$ or F)	Vibration $X_{s-rms}$ (m)	Stroke $\Delta X_{rms}$ (m)	Harvesting $\sqrt{P_{ave}}$ ( $\sqrt{W}$ )
Optimized for vibration control	$5.496e^{-5}$	$0.353\Omega$ $0.476F$	$3.704e^{-8}$	$3.2426e^{-7}$	$6.417e^{-5}$
Optimized for energy harvesting	$5.540e^{-5}$	$0.351\Omega$ $0.473F$	$3.707e^{-8}$	$3.2431e^{-7}$	$6.419e^{-5}$

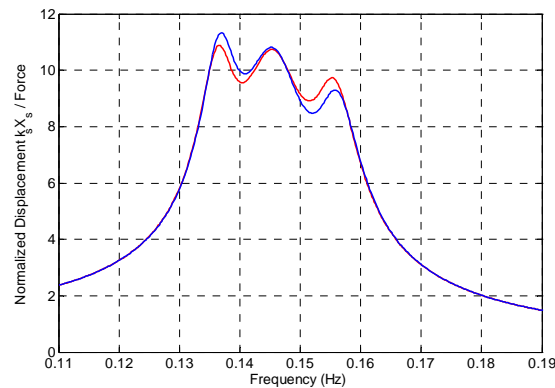


Figure 5.28 The frequency response of the electromagnetic series TMD optimized for vibration suppression (red solid) and optimized for energy harvesting (blue dash) for Taipei 101 Tower.

The frequency responses from external force  $F_{ex}$  to the square root of harvesting power  $\sqrt{P}=\sqrt{R}|\dot{q}|$  of electromagnetic shunt series TMDs are compared in Figure 4.29 with the square root of power of the classic TMD  $\sqrt{c_1}|\dot{x}_1 - \dot{x}_s|$  and that of double-mass series TMD  $\sqrt{c_1}|\dot{x}_2 - \dot{x}_1|$ . Again we see the electromagnetic series TMDs perform similar as the double-mass series TMD and outperform the classic TMD in power harvested.

It is also noted that the energy dissipations by the primary damping of the Taipei 101 building with TMDs ( $\sqrt{c_s}|\dot{x}_s|/F_{ex}$ ) are less than the energy extracted by the dual-functional TMDs, as indicated in the right column of Table 4.7.

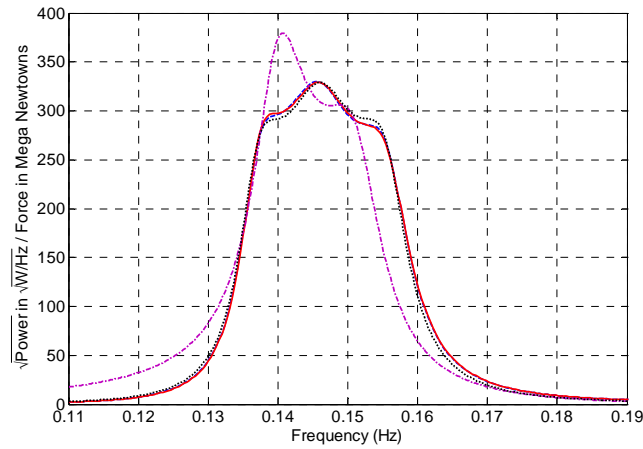


Figure 5.29 The linear power spectrum density of harvested energy in electromagnetic series TMD system optimized for energy harvesting under white-noise force excitation (solid red) and optimized for vibration suppression (blue dash) in comparison with the classic TMD (purple dash-dot) and double-mass series TMD (black dot)

### 5.5.2.3 Sensitivity of Vibration Suppression and Energy Harvesting to Tuning Parameters

In practice it is difficult to make perfect tuning, or some parameter may change after some time. To investigate the sensitivity of the performances to the tuning parameters  $k_1$ ,  $C$ , and  $R$ , we plot the root mean square of the vibration amplitude and the square root of the harvested power under unit white-noise excitation force  $F_{ex}$  when the parameters change from 1/3 to 3 time of the optimal value, as shown in Figures 4.30 and 4.31. We see that the performances are less sensitive to the change of electrical load  $R$  than the changes of capacity  $C$  and stiffness  $k_1$ .

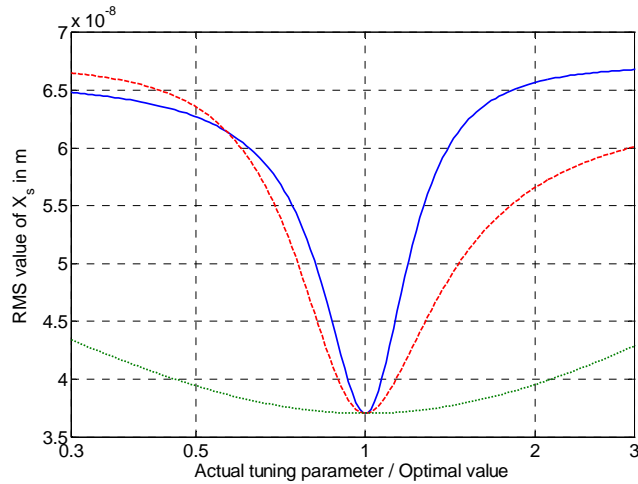


Figure 5.30 Sensitivity of vibration suppression of the electromagnetic shunt series TMD for Taipei 101 to the changes of tuning parameters: stiffness  $k_1$  (blue solid), capacitor  $C$  (red dash), and electrical load  $R$  (green dot) under unit white-noise force excitation  $F_{ex}$ .

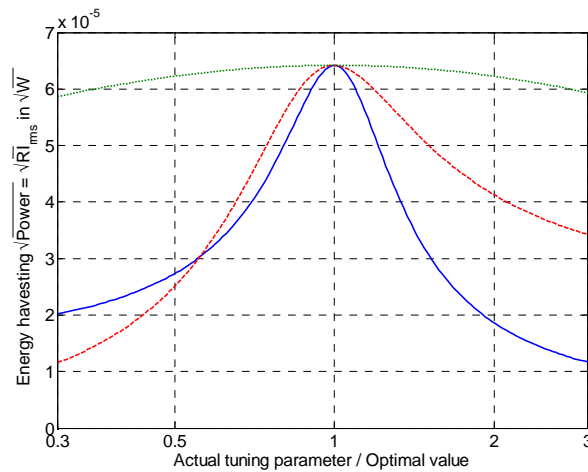


Figure 5.31 Sensitivity of energy harvesting of the electromagnetic shunt series TMD for Taipei 101 to the changes of tuning parameters: stiffness  $k_1$  (blue solid), capacitor  $C$  (red dash), and electrical load  $R$  (green dot) under unit white-noise force excitation  $F_{ex}$ .

## 5.6 Summary

This chapter optimized the parameters of the different TMDs for vibration control and energy harvesting, including the traditional vibration energy harvester, the newly proposed

electromagnetic TMDs, series TMD, electricity-generating TMD and electromagnetic series TMD.

Table 5.8 Optimal parameters of different TMD for vibration mitigation.

		$H_2$	$H_\infty$	Fixed point method
Electromagnetic shunt TMD	Tuning ratio $f$	$\sqrt{1 - \frac{\mu_k}{2}}$	$\sqrt{\frac{2r^{\text{opt}} - \mu_k + \sqrt{(2r^{\text{opt}} - \mu_k)^2 + 12r^{\text{opt}2}}}{6}}$ **	$\sqrt{1 - \frac{\mu_k}{2}}$
	Damping ratio $\zeta$	$\sqrt{\frac{\mu_k^2 - 4\mu_k}{8\mu_k - 16}}$	$\sqrt{\frac{r^{\text{opt}}(f^{\text{opt}2} + 1 + \mu_k) - (f^{\text{opt}2} + \mu_k + r^{\text{opt}2})}{2r^{\text{opt}}(f^{\text{opt}2} - r^{\text{opt}})}}$	$\frac{1}{2} \sqrt{\frac{3\mu_k}{2 - \mu_k}}$
Classic TMD	Tuning ratio $f$	$\frac{1}{1 + \mu} \sqrt{\frac{2 + \mu}{2}}$	$\frac{1}{1 + \mu}$	$\frac{1 + \mu}{2}$
	Damping ratio $\zeta$	$\sqrt{\frac{\mu(3\mu + 4)}{8(1 + \mu)(2 + \mu)}}$	$\sqrt{\frac{3\mu}{8(1 + \mu)}}$	$\sqrt{\frac{3\mu}{8(1 + \mu)^3}}$
Electricity-generating TMD	Tuning ratio $f$	$\sqrt{1 - \sqrt{\frac{\mu}{1 + \mu}}}$	N/A	N/A
	Stiffness ratio $\mu_k$	$2[\mu + \sqrt{\mu(1 + \mu)}]$	N/A	N/A
	Damping ratio $\zeta$	$\sqrt{\frac{\mu + \sqrt{\mu(1 + \mu)}}{2[1 - (\sqrt{\frac{\mu}{1 + \mu}} - 1)^2](1 + \mu)^2}}$	N/A	N/A
Three-element TMD	Tuning ratio $f$	$\sqrt{1 - \sqrt{\frac{\mu}{1 + \mu}}}$	N/A	N/A
	Stiffness ratio $k$	$2[\mu + \sqrt{\mu(1 + \mu)}]$	N/A	N/A
	Damping ratio $\zeta$	$\sqrt{\mu[(1 + \mu) - \frac{3 + 2\mu}{2} \sqrt{\frac{\mu}{1 + \mu}}]}$	N/A	N/A

$$**r^{\text{opt}} = \frac{1}{2} + \frac{\mu_k}{8} + \frac{\sqrt{\mu_k^2 - 24\mu_k + 16}}{8}.$$

The analytical solutions to the optimal parameters for vibration mitigation are summarized in Table 4.8, which can be useful for practical implementation. The others are optimized numerically using decentralized control method. The sensitivity analysis carried out in this chapter. It is also found that when optimized the electricity-generating TMD will have similar

performance as the three-element TMD, which also have better vibration mitigation performance than the classic TMD. The series TMD will have more robustness and effectiveness than the classic TMD while having large stroke problem, which is solve by the so-called electromagnetic series TMD, where a R-L-C circuit is implemented for the additional resonant in similar way as the mass-spring system.

## Chapter 5

# Design and Optimization of Electromagnetic Vibration Energy Harvesters

In this chapter, the electromagnetic vibration harvesters which are used to convert the vibration energy into electric energy will be developed and optimized. The electromagnetic energy harvesters have been used in large-scale vibration energy harvesting applications, such as energy harvesting from vehicle suspensions (Nakano *et al.*, 2003; Gupta *et al.*, 2006; Kawamoto *et al.*, 2007 and 2008; Zuo *et al.*, 2011) and civil structures. By using regenerative vehicle suspensions, the vibration energy due to the road roughness, turning and braking, can be converted into useful form of electricity. The unique challenge in large-scale energy harvesting is retrofit and dual-function design, which means the dimension of the harvester should be strictly constrained to the existing suspension structure or the civil structures and be able to provide sufficient damping coefficient while harvesting the vibration energy. So far, most the linear electromagnetic harvesters in literature are too large for retrofit or can't extract sufficient energy to provide sufficient damping. In another word, the power density is not as large as the energy dissipation rates of current oil dampers. The motivation of this chapter is to study parameter optimization and new configurations, intending to make harvester retrofittable with reasonable size and capable of providing sufficient damping while harvesting the energy. It should be noted that some relevant work on the configurations of the magnets were studied by Zuo *et al.* (2011),

Ebrahimi *et al.* (2008) and Palomera-Arias (2005) for the applications of eddy current dampers, where the energy harvesting is not considered.

## 6.1 Tubular Linear Energy Harvester

### 6.1.1 Optimization of a Tubular Linear Energy Harvester

The tubular linear energy harvester proposed and optimized in this chapter, consists of a magnet assembly and coil assembly, as shown in Figure 5.1. Relative motion between the coils and magnets will convert the vibration energy into electricity. The magnet assembly is made of ring-shaped NdFeB permanent magnets and ring-shaped high magnetically permeable steel spacers stacked on a rod made of high reluctance material. The magnets are arranged with like-poles of adjacent magnets facing each other to redirect the magnetic flux to the radial direction. A concentric outer cylinder made of high magnetically permeable material is used to reduce the reluctance of magnetic loops, to further increase magnetic flux density in the coils.

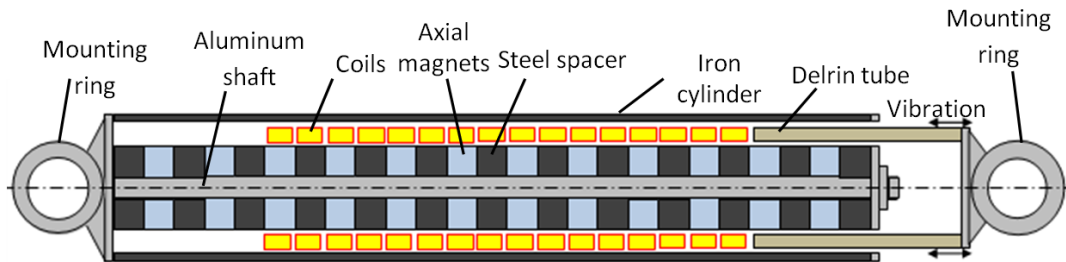


Figure 6.1 Diagram of the linear electromagnetic vibration energy harvester.

The parameters such as the axial thickness  $\tau_{ma}$  and the thickness of the coil in radial direction  $\tau_{cr}$ , as shown Figure 5.1, are optimized in order to improve the magnetic flux density and power density with 2D axisymmetric FEA.

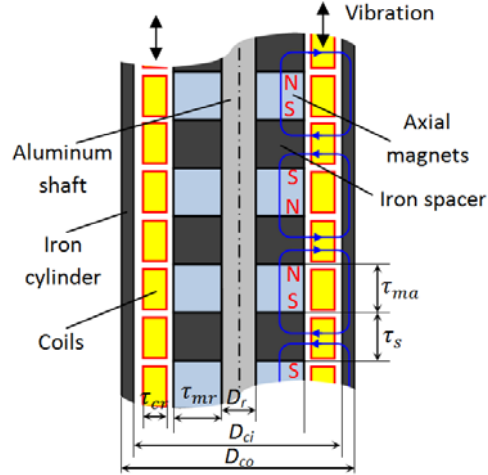


Figure 6.2 Linear energy harvester dimensions and parameters.

The voltage  $V$  generated by a conductor of length  $l$  moving in a constant magnetic flux density  $B$ , at a constant velocity  $v$  is given by

$$V = Bvl \quad (5.1)$$

The current  $I$ , generated by the device with short circuit can be expressed by the equation (5.2).

$$I = \sigma B_r v_z A_w \quad (5.2)$$

where  $\sigma$  is the electrical conductivity of the conductor,  $B_r$  is the average magnetic flux density in the radial direction,  $v_z$  is the constant relative velocity of the conductor in the axial direction moving in the magnetic field, and  $A_w$  is the cross-sectional area of the wire. The peak power  $P$  is calculated by combining Equations (5.1) and (5.2):

$$P = VI = B_r^2 v_z^2 \sigma l A_w \quad (5.3)$$

The effective length of the coil can be expressed:

$$l = \pi D_c N \quad (5.4)$$

where  $D_c$  is the average diameter of the coils, and  $N$  is the number of turns which is defined as

$$N = \frac{\pi A_c}{2\sqrt{3} A_w} = \frac{\pi 4A_c}{2\sqrt{3} \pi d^2} = \frac{2A_c}{\sqrt{3}d^2} \quad (5.5)$$

where  $d$  is the diameter of the wire,  $A_c$  and  $A_w$  are the cross-sectional area of the coil and wire. Thus,



$$V = \frac{2\pi |B_r| |v_z| D_c A_c}{\sqrt{3} d^2} \quad (5.6)$$

The power can be finally expressed by:

$$P = \frac{\pi^2 \sigma B_r^2 v_z^2 D_c A_c}{2\sqrt{3}} \quad (5.7)$$

According to Equation (5.7), the power is proportional to the square of magnetic flux density and the cross-sectional area of the coil. Therefore, there are two approaches on increasing generated power of LETs. One way is to increase the magnetic flux density inside the air gap. The other way is to increase the effective volume of the coil, which is equivalent to increasing  $\tau_{cr}$ . However, there is a tradeoff, because increasing the coil thickness  $\tau_{cr}$  or the air gap will decrease the magnetic flux. In this chapter, the power density ( $\text{W/m}^3$ , power over the volume of the energy harvester) is taken as the performance index rather than just the power.

Hence, a comprehensive analysis is carried out to optimize magnet thickness  $\tau_{ma}$  and coil thickness  $\tau_{cr}$  using FEA, as shown in Figure 5.3 and 5.4. It should be noted that the overall diameter of the energy harvesting is assumed to be pre-determinate as 63.5mm (2.5") which means that the total space occupied by the coil and the magnets is constant. The assumption is made because the OD is always determined by the specific application. There is also 0.5mm gap in the radial direction between magnets, coil and steel casing, which means the air gap between the magnets and steel casing is 1mm larger than coil thickness in radial direction  $\tau_{cr}$ .

It shows (in Figure 5.3) that  $|B_r|$  always decreases with the increase of coil thickness  $\tau_{cr}$  or the air gap, at different  $\tau_{ma}$ . However, there is an optimal magnet thickness  $\tau_{ma}$  at a constant  $\tau_{cr}$ . It also should be noted that the average  $|B_r|$  in Figure 5.3 is obtained by the integral of radial magnetic flux density (absolute value) in the coil divided by the volume of the coil. If we plug the average  $|B_r|$  into Equation (5.7) to calculate the power, the results may be a little underestimated since the power is proportional to the  $B_r^2$ . Figure 5.4 shows how power density as a function of magnetic thickness  $\tau_{ma}$  in axial direction and coil thickness  $\tau_{cr}$  in radial direction, from which we can conclude that there is an optimal power density. When  $\tau_{ma} = 11\text{mm}$ ,  $\tau_{cr} = 3\text{mm}$ , the global maximum power density is  $18.4 \times 10^4 \text{ W/m}^3$  at 0.25m/s velocity, corresponding to 3.8 times improvement, compared with the previous design, which has  $4.8 \times 10^4 \text{ W/m}^3$  power density (Zuo *et al.*, 2011). From Figure 5.4, we can also conclude that around the

optimal values of  $\tau_{ma}$  and  $\tau_{cr}$ , the power density is not very sensitive to the thickness  $\tau_{ma}$  of magnets and spacers, which gives some flexibility when designing harvesters with dimension constraints

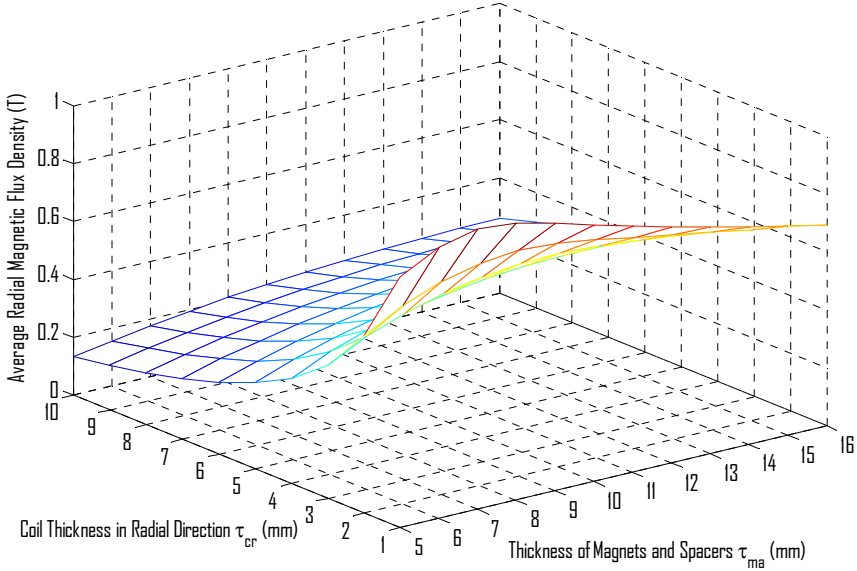


Figure 6.3 Average value of the absolute magnetic flux density in radial direction  $|B_r|$  at different magnets thickness  $\tau_{ma}$  and coil thickness in radial direction  $\tau_{cr}$ , where OD of the harvester is preselected as 63.5mm (2.5 inches).

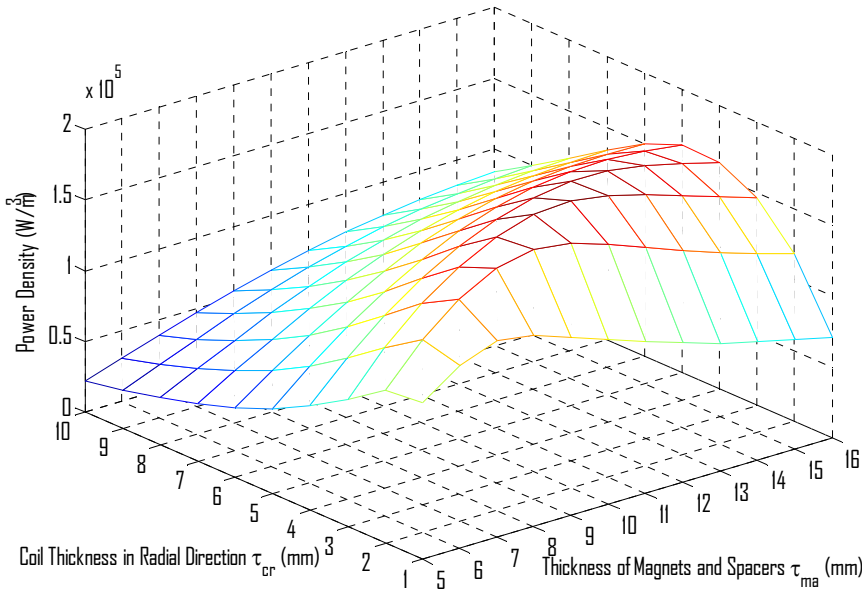


Figure 6.4 Power density at different magnets thickness  $\tau_{ma}$  and coil thickness in radial direction  $\tau_{cr}$ , where OD of the harvester is preselected as 63.5mm (2.5 inches).

The damping density is  $2940 \text{ kN}\cdot\text{s}/\text{m}^4$ , which is in the order of the damping density of oil dampers that are currently used in vehicle suspensions and building vibration mitigation ( $2800\text{-}4200 \text{ kN}\cdot\text{s}/\text{m}^4$  (Rasmussen,1997; Taylor)). It also should be noted that the power and damping density in this chapter are calculated with assumption that the LETs have stroke of 20% of the magnetic thickness and the coils are shunt at two ends.

The power density obtained above actually assumes the number of the coil phases is infinity. In practice the coils have finite phases. The numbers of phases also have important influence on the power output. If the height of the coil is equal to the length of magnetic flux cycle, there will be no electricity generated at all because both positive and negative electromotive potential will be induced in the same coil segment and will be cancelled. The two phase design is shown in Figure 5.5. When one of the two phases reaches the max voltage (positive) another phase will reach minimal (negative).

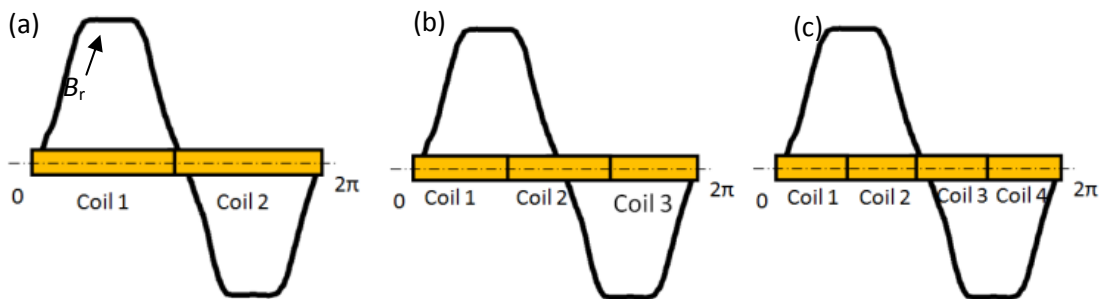


Figure 6.5 Coil design: (a) Two phase coil; (b) Three phase coil; (c) Four phase coil.

Generally speaking, the more the coil phases are, the more power it will produce. Figure 5.6 shows such a relationship, which is obtained by taking the average power of coil segments moving through one period of magnetic flux distribution. Three phase design will have more power density than two phase design, and four-phase motor will have the more power density than three-phase design. Figure 5.5 (b) illustrates the three phase coils, each occupying one third of the flux cycle length. When the coil is moving around the position show in Figure 5.5(b), the second coil generates no electrical voltage. In a four-phase harvester, the width of wire coil is the same as the thickness of the magnets in the axial direction. The four-phase motor design is

illustrated in Figure 5.5(c) and the power density is two times was two-phase design. As shown in Figure 5.6, the benefit of power density is diminishing when the number of phases is large. Besides, more phases may complicate the harvester circuits and more coil winding work. So we choose four-phase design in our prototype.

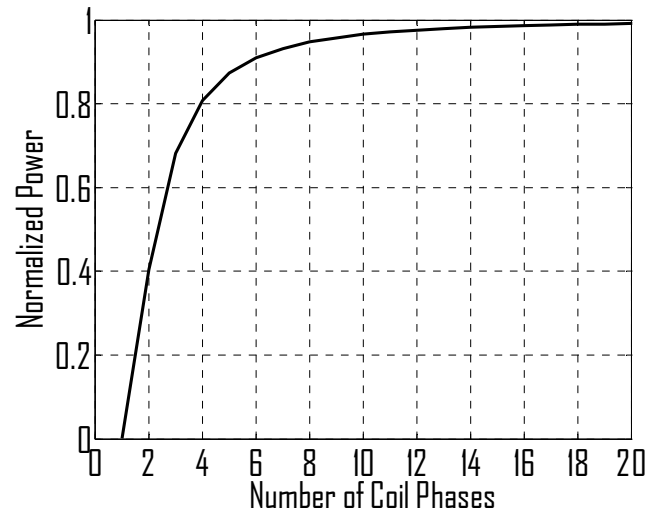


Figure 6.6 Normalized power and number of coils phases.

### 6.1.2 New Configurations and Analysis

The harvesters discussed in the previous section use only axial magnets and steel spacers. Instead of using steel spacers, we can replace them with the radial magnets, as shown in Figure 5.7, to increase the flux density. Radial magnet is new kind of magnet which is magnetized in radial direction. Hence it can directly provide flux density in radial direction directly. The magnetic flux loop is shown in Figure 5.7 as well. In order to have a better guiding on magnetic flux, a double-layer electromagnetic harvester is introduced. Figure 5.8 shows the double-layer linear energy harvesters, where another layer of magnet rings and steel spacers with larger diameter is added to further improve the flux density and power density. It should be noted that in double-layer configurations, the outer cylinder can be eliminated or be made of aluminum rather than steel, because the effective magnetic fluxes are between the inner magnets and outer magnets.

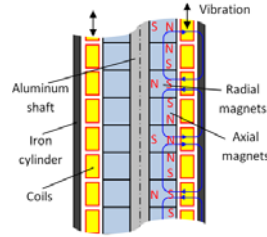


Figure 6.7 The single-layer linear electromagnetic harvester with both axial and radial magnets.

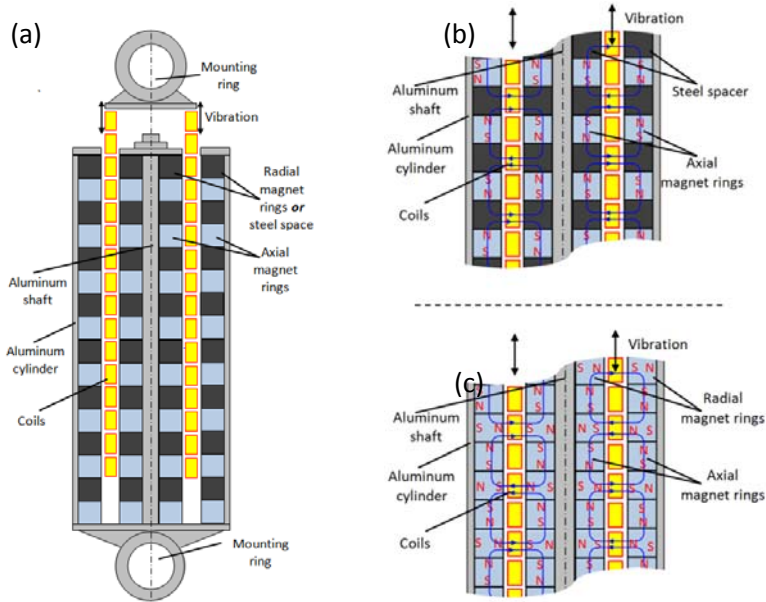


Figure 6.8 The double-layer linear electromagnetic harvester: (a) overview; (b) with axial magnets and steel spacers; (c) with both axial and radial magnets.

Figure 5.9 shows the FEA results of different configurations. In this FEA,  $\tau_{ma} = 11\text{mm}$ ,  $\tau_{cr} = 3\text{mm}$ , the inner magnets has 12.7 mm (0.5”) ID and 44.45 mm (1.75”) OD. The outer magnets for the double-layer configuration have 52.45mm ID and 76.2mm OD (3inches). It should be noted that LETs presented in this section are not optimized except for the one with single-layer axial magnets and spacers. The comparisons in this section are to show the effectiveness of the new configurations. As shown in Table 5.1 and Figure 5.10, with the same dimensions, the single-layer configuration using axial and radial magnets can increase average  $|B_r|$  from 0.614T to 0.682T and power density increases from  $17.2 \times 10^4 \text{ W/m}^3$  to  $21.3 \times 10^4 \text{ W/m}^3$  at 0.25m/s vibration velocity. It also can be seen from Figure 5.10 and Table 5.1, the best configuration is the one shown in Fig. 16 (c), which is double-layer configuration with both axial and radial magnets. The peak flux density is as high as 1.51T and average  $|B_r|$  is 1.01T. The power density

is  $27.2 \times 10^4 \text{ W/m}^3$  and the corresponding damping density  $4357 \text{ kN}\cdot\text{s/m}^4$ , which is 5.6 times larger than the previous design (Zuo *et al.*, 2011). This damping density at shot circuit is comparable with that of the oil dampers currently used in vehicle suspensions and structural vibration control, suggesting that the LETs are able to provide sufficient damping for both vehicle suspension and buildings vibration mitigation with reasonable size. Although the double-layer configuration with axial magnets can increase the average  $|B_r|$  to 0.880T, due to the increased volume the increase of damping density (from 2758 to  $3335 \text{ kN}\cdot\text{s/m}^4$ ) is smaller than that of single-layer configuration using radial magnets (from 2758 to  $3403 \text{ kN}\cdot\text{s/m}^4$ ).

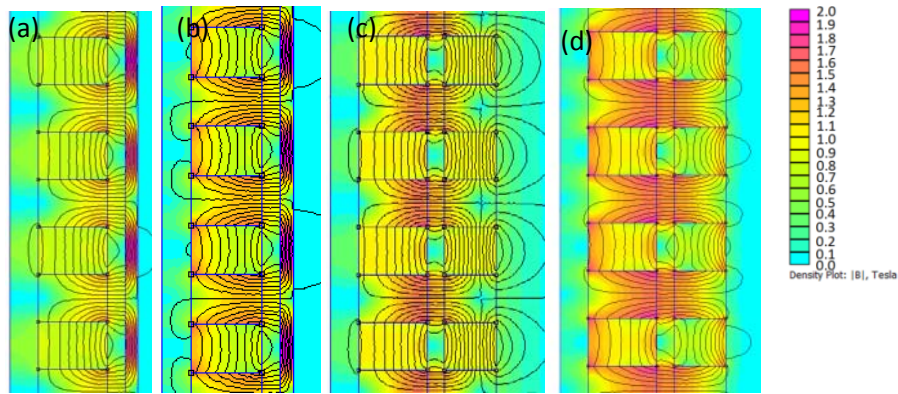


Figure 6.9 FEA result of different configurations: (a) single layer with axial magnets, (b) single-layer with axial and radial magnets, (c) double-layer with axial magnets, (d) double-layer with axial and radial magnets.

Table 6.1 Absolute value of average radial magnetic flux density  $|B_r|$ , power density and damping density in different configurations.

Configurations	$ B_r $ (T)	Power density ( $\text{W/m}^3$ )	Damping density ( $\text{kN}\cdot\text{s/m}^4$ )
Single-layer, axial magnets	0.614	$17.2e^4$	2758
Single-layer, axial & radial magnets	0.682	$21.3e^4$	3403
Double-layer, axial magnets	0.880	$20.8e^4$	3335
Double-layer, axial & radial magnets	1.010	$27.2e^4$	4357
Building oil damper in (Rasmussen,1997)	/	/	3192
Building oil damper in Taylor)	/	/	4263
Typical shock absorber in car	/	/	2800

The performances of different configurations are listed in Table 5.1, where the damping densities of some oil dampers are also included for comparison. Figure 5.10 shows the magnetic flux density along radial and axial direction of the LET in the gap space where coils occupy. Based on the previous experiment results in last section, we expect that 26W and 33W power can be practically harvested for the single-layer and double-layer LETs with both axial and radial magnets of overall diameter 3” at 0.25m/sec vibration velocity, with four-phase coil design.

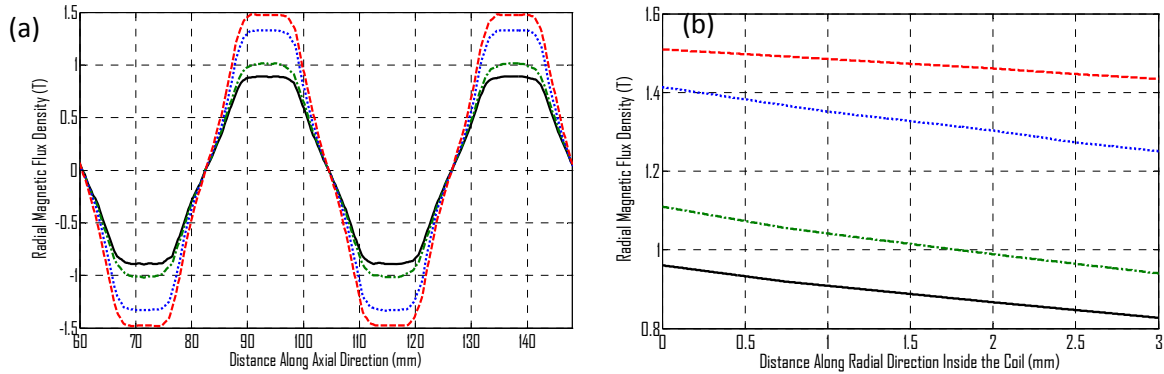


Figure 6.10 Magnetic flux density (a) along the center line of air gap, (b) along the radial direction inside of the coil ( — single-layer with axial magnets, — . — single-layer with both axial and radial magnets, ..... double-layer with axial magnets, - - - - double-layer with both axial and magnets).

### 6.1.3 Experimental Characterization

Since the power density is not sensitive to the thickness of the magnets and spacers and 2mm coil thickness is too small to be implemented, a prototype is built using magnets of 0.5” (12.7mm) thickness and 1.75” (44.45mm) out diameter and the coil thickness is about 5mm. The total compressed length of the harvester is 12 inches (30.5cm) and the diameter is 2.25 inches (5.7cm). We also investigated the effect of the steel casing experimentally. So, two prototypes (Figure 5.11), namely the one without steel casing and with steel casing, are tested and compared in the following section. Figure 5.12 shows the magnetic flux density measurement of the prototype without casing. The results show that the measurement and simulation match well with each other. And the measured magnetic flux density is a little smaller than the simulation results. Since it is hard to measure the magnetic flux density of harvester with casing, it is predicted

using simulation, which is up to 0.56 in center of the coil wall, as shown by the dash-dot curve in Figure 5.12.

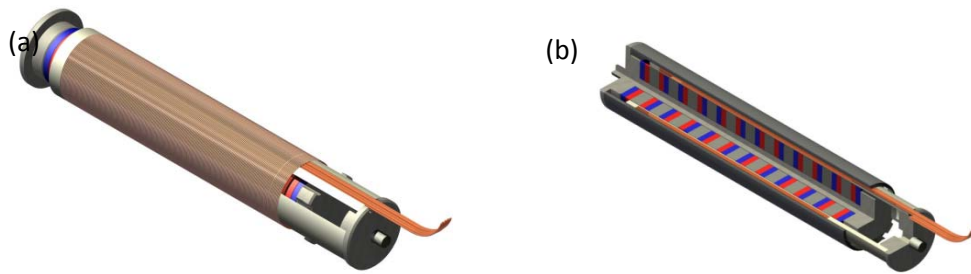


Figure 6.11 Linear energy harvester prototypes: (a) without steel casing (b) with steel casing.

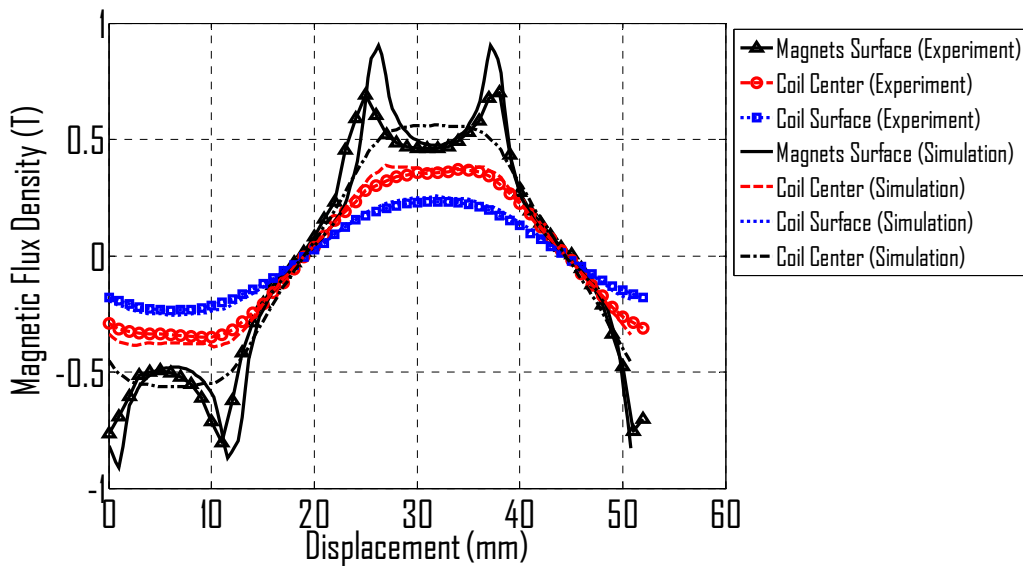


Figure 6.12 Magnetic flux density measurement of the prototypes.

Both prototypes are mounted on a shaker to test the damping capacity and energy harvesting ability, where the coil assembly of the vibration energy harvester is mounted to the mover of a vibration shaker, as shown in Figure 5.13. Since the 0 and 180 degree coils, 90 degree and 270 coils have 180 degree phase difference, coils of phase 0 and 180 degree are connected in series reversely and coils of 90 and 270 degree phases are also connected in series reversely. Hence, there are totally two coils, each of which has totally 40  $\Omega$  internal resistance. The shaker drives the relative motion between the magnet and coil assemblies via a 5x power amplifier. The damping force and output voltage are measured by the dynamic analyzer. A force sensor PCB 208C02 is mounted at the end of the connector to measure the actuation force, and a laser displacement sensor Micro-Epsilon OptoNCDT 1401 is used to measure the relative motion. The



shaker can be modeled as a single-DOF vibration system and the modeling of the whole experiment system are shown in Figure 5.14, where  $m_c$  is the mass of the coil assembly and  $m_s$  is the mass of shaker mover. It should be noted that due to stroke limitation of the shaker, the vibration harvester is tested under small relative displacement. However, it can be used for applications with large stroke too.

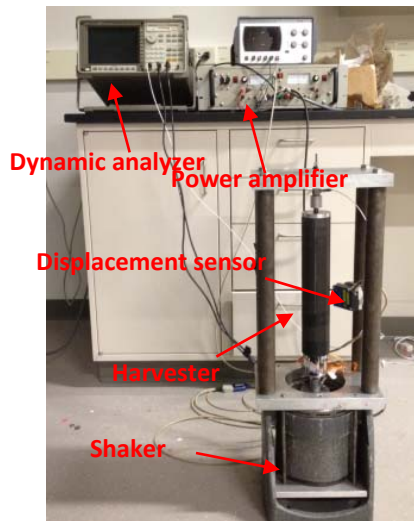


Figure 6.13 Experiment setup.

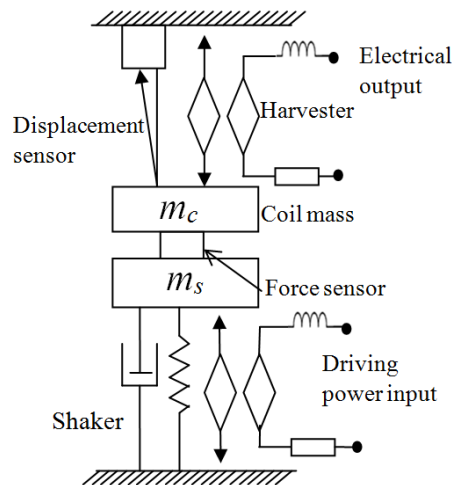


Figure 6.14 Model of the experiment set up.

Figure 5.15 shows the generated open-circuit voltage and force of the harvester under 10Hz and 2.54mm peak-to-peak amplitude harmonic excitation. As we can see from the figure, the forces generated when harvesters are open-circuit are mainly dry friction force, which is 4.8N and

14.5N in prototypes without and with steel case respectively. By adding a steel casing, the voltage generated by each coil increases from 9.5V to 17V and from 2.8V to 4.1V respectively.

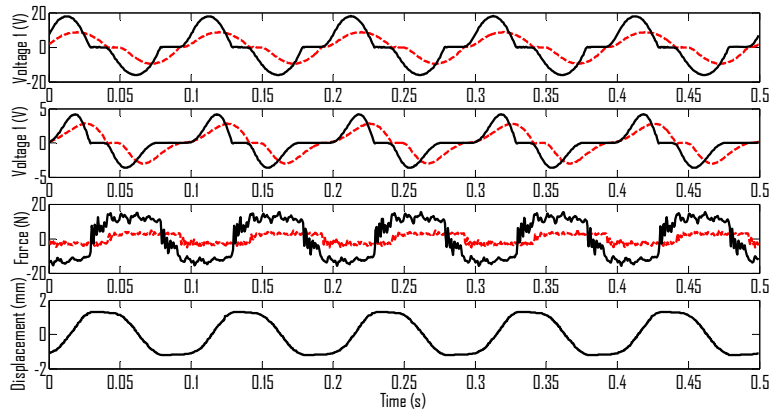


Figure 6.15 Voltages and force generated when LET is open-circuit under 10HZ harmonic excitation of 2.54mm peak-to-peak amplitude. ( — LET with steel casing, - - - LET without steel casing).

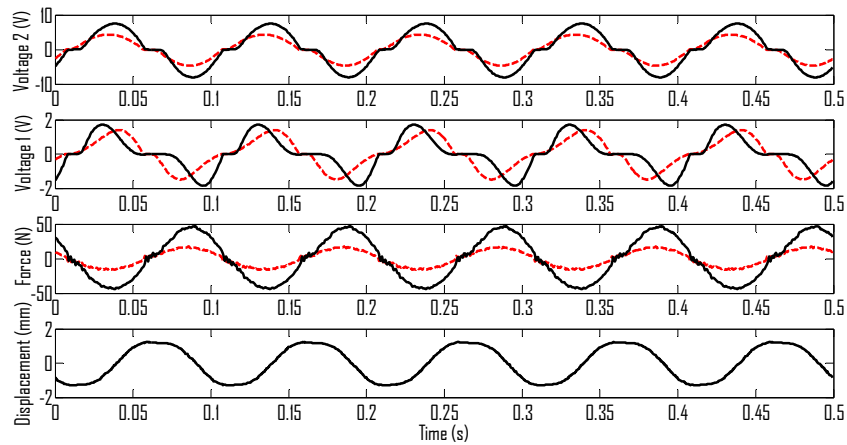


Figure 6.16 Voltages and force generated when LET is shunt with 40  $\Omega$  electric load, under 10HZ harmonic force excitation of 2.54mm peak-to-peak amplitude ( — LET with steel casing, - - - LET without steel casing).

Figures 5.16 and 5.17 show the time response of the vibration energy harvester under 10Hz harmonic force excitation. Since each coil has 40  $\Omega$  internal resistance, it are shunt with 40  $\Omega$  external resistor to achieve maximum power. Under the 2.54mm peak-to-peak harmonic vibration, the harvester can generate 2.8V and 8.9V peak-to-peak voltage and 34N peak-to-peak damping force without steel casing, 3.5V and 15.5V and 91N damping force with steel casing.

The peak power harvested is 0.59W and 1.66W for each prototype and the corresponding RMS power is 0.25 W and 0.64W. The input RMS power for each prototype is 0.64W and 1.83W. Hence the mechanical efficiency of the prototype without steel casing is 78% and 70% for the one with steel casing. The results are further summarized in Table 5.2.

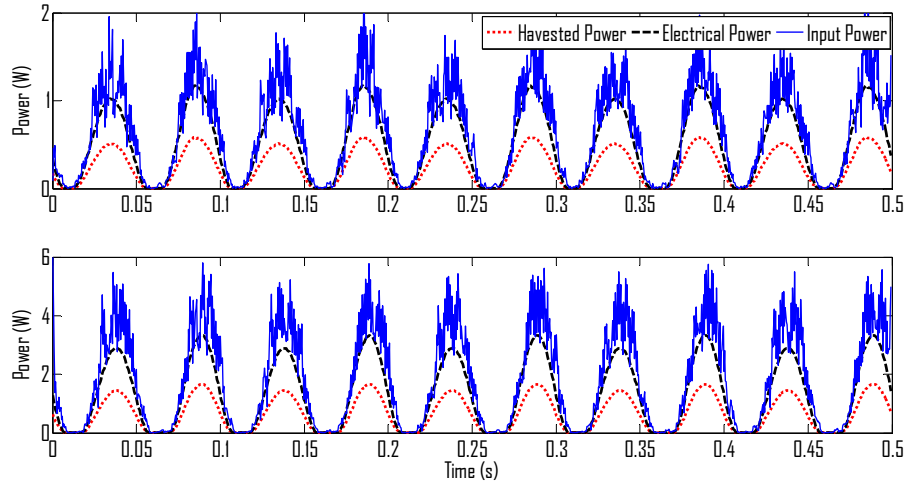


Figure 6.17 Instant power when linear harvester is shunt with 40  $\Omega$  electric load.

Table 6.2 Experiment result of linear energy harvesters under 10Hz excitation.

	Without Casing	With Casing
Peak Power	0.59W	1.66W
RMS Power	0.25W	0.64W
Input Power	0.64W	1.83W
Mechanical Efficiency	78%	70%
Peak-to-Peak Force	34N	91N
Damping Coefficient	213 Ns/m	571Ns/m
Damping Density	274 kN·s/m <sup>4</sup>	734 kN·s/m <sup>4</sup>

\* The terminals of the coils are connected with 40  $\Omega$  electric load.

Figure 5.18(a) shows the RMS voltage generated by harvester with steel casing at different harmonic force amplitude at 10Hz. In this figure, the harvester is also shunted with a 40  $\Omega$  resistor. Figure 5.19(b) shows the corresponding power. About 2.8W power can be generated at obtained at 5mm peak-to-peak amplitude, which is corresponding to 0.11m/s RMS velocity. It should be noted that the relative velocity of vehicle suspension is about at 0-0.15m/s at good road and 0-0.25m/s at average road.

Since the power is proportional to the square of velocity and volume, the experiments can predict that for a single-layer LET with 3" OD and 12" compressed length electrical power 20.8W can be harvested on the matching electric load at 0.25m/s vibration velocity, and the corresponding power density is  $1.5 \times 10^4 \text{ W/m}^3$ . If the energy harvester is short-circuit, the corresponding dissipating power density  $6 \times 10^4 \text{ W/m}^3$ , while the FEA predicts  $15.8 \times 10^4 \text{ W/m}^3$  ( $\tau_{\text{ma}} = 12.7 \text{ mm}$  and  $\tau_{\text{cr}} = 5 \text{ mm}$ ). It can be seen that experimental power density is less than half of the FEA results. There are several reasons: one is that we use four-phase coil which have 80% efficiency; the other reason is that the winding of coil is not perfect and there is significant gap in the coil. Also, the delrin tube space which the coils are wound on is not taken into account. However, the measured magnetic flux density is compared with the simulation result which matches very well. It suggests that the FEA simulation is reasonable. The main reason of the low power density in the experiment is the construction of the coil assembly.

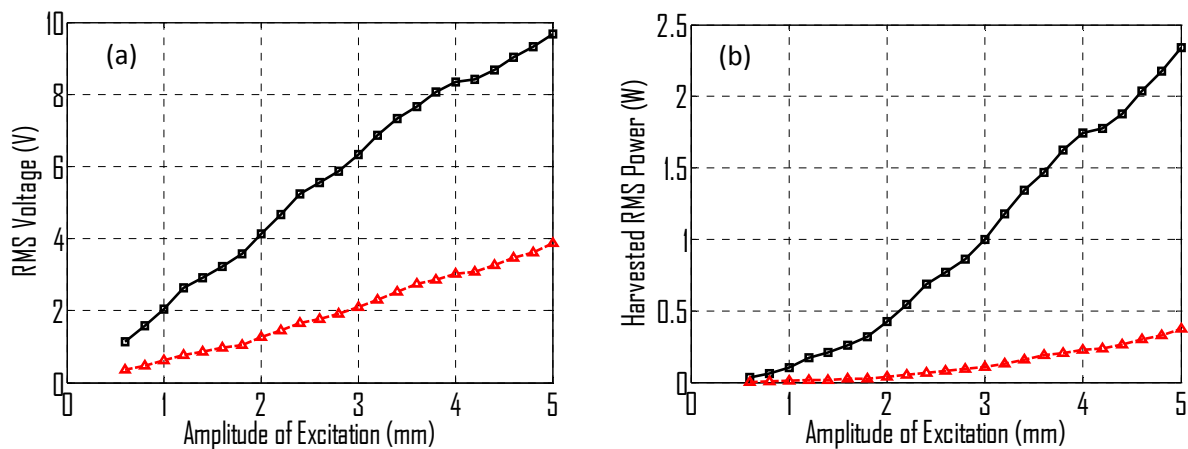


Figure 6.18 Harvester with steel casing under 10Hz harmonic excitation with different amplitude: (a) RMS voltage; (b). RMS power. (— LET with steel casing, - - - LET without steel casing).

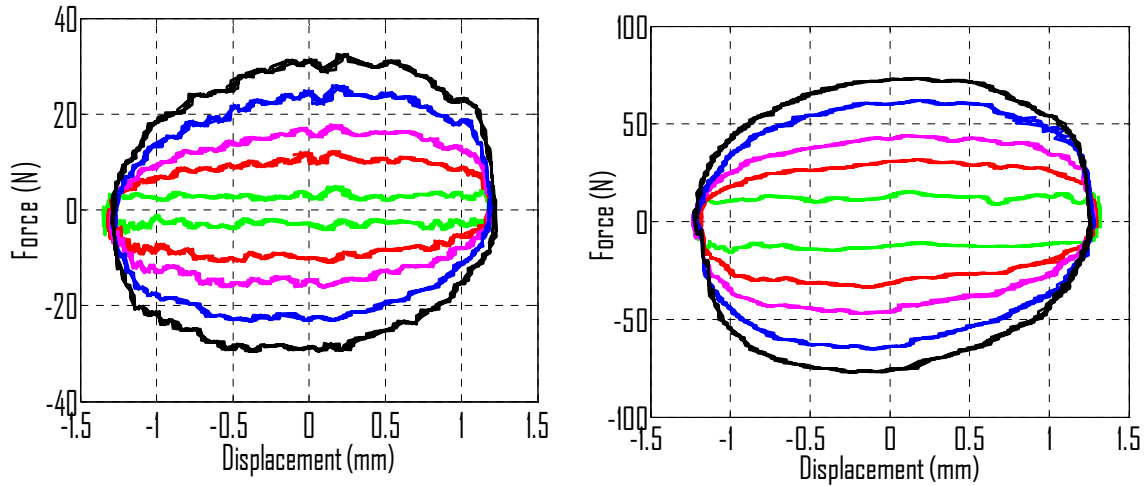


Figure 6.19 Damping loop under harmonic excitation with different external resistors, namely open circuit (green curve), 100  $\Omega$  (red curve), 40  $\Omega$  (purple curve), 10  $\Omega$  (blue curve) and short circuit (black curve): (a)10HZ without casing, (b)10HZ with casing.

Table 6.3 Damping achieved and with different external electrical load.

	Without Casing		With Casing	
	Damping Coefficient (Ns/m)	Damping Density (kNs/m <sup>4</sup> )	Damping Coefficient (Ns/m)	Damping Density (kNs/m <sup>4</sup> )
Open circuit	63	81	169	217
100 $\Omega$	145	186	411	528
40 $\Omega$	213	274	571	734
10 $\Omega$	308	396	798	1026
Short circuit	387	498	940	1208

Figures 5.19(a) and (b) further show the damping loop under 10Hz harmonic force excitation with different external resistance load, namely open circuit, 100  $\Omega$ , 40  $\Omega$ , 10  $\Omega$  and short circuit. When it is short-circuit, the prototype LETs will provide 387Ns/m and 940Ns/m damping coefficient, however no energy is harvested. When shunt with 40  $\Omega$ , maximum harvesting power is achieved while providing 213Ns/m and 571Ns/m damping coefficient. Shunt with 10  $\Omega$ , 308Ns/m and 798Ns/m damping is obtained. The detailed result is also summarized in Table 5.3. By switching the resistive load connected to vibration energy harvester, the damping coefficient

can be changed accordingly, which mean the harvester can be implemented with different semi-active damping control algorithms to achieve better vibration mitigation performance.

## 6.2 Cubic Linear Energy Harvester

### 6.2.1 Concept and Design

Another electromagnetic vibration energy harvester prototype with alternating magnetic fields was developed, the schematic view of which is shown in Figure 5.20. A total of twenty 1"x2"x0.5" permanent magnets (Neodymium Iron Boron grade N35) are arranged as an array. The pole direction of magnets in each row is arranged alternatively, forming a magnetic loop with small reluctance. Four slots of ¼" width exist between the rows to allow the motion of the four coil plates. Two pieces of soft iron are set in the back of the first and last rows of the magnets to reduce the reluctance of magnetic loops. Three sets of wound coils are installed inside a plastic frame, forming a coil plate. Four of such coil plates move in the perpendicular direction of the magnetic flux and generate electricity. The dimension of the whole vibration energy harvester is about 142x140x86 mm<sup>3</sup>, including the soft iron in the back of magnets. It also should be noted that this configuration was also studied by the authors by Zuo *et al.*(2011), for the eddy current damper applications.

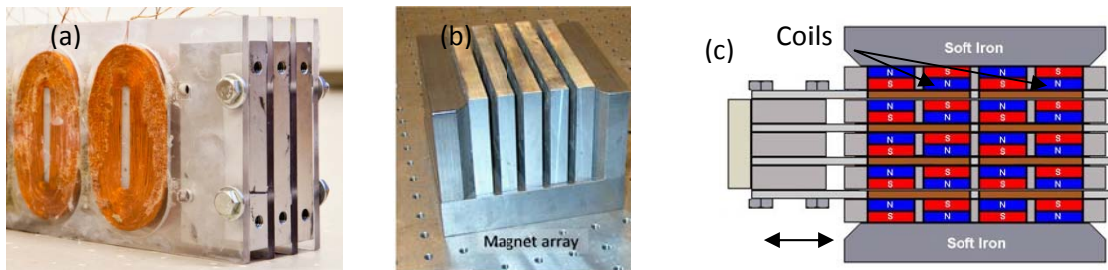


Figure 6.20 Design of a new type of electromagnetic vibration harvester: (a) assembly of coil array, (b) assembly of magnets, (c) top view of whole vibration energy harvester.

The configuration can provide very large effective magnetic flux density. Figure 5.21(a) shows a top view of 3-D finite element magnetic field in the magnetic loops composed of the magnets, air, and iron. The streamlines represent the magnetic flux density. Figure 5.21(b) shows the magnetic intensity  $B_p$  perpendicular to the coil plate. As we can see from the figure, the magnetic flux density is up to 0.9T in the air gap, where the coil plating is moving back and forth.

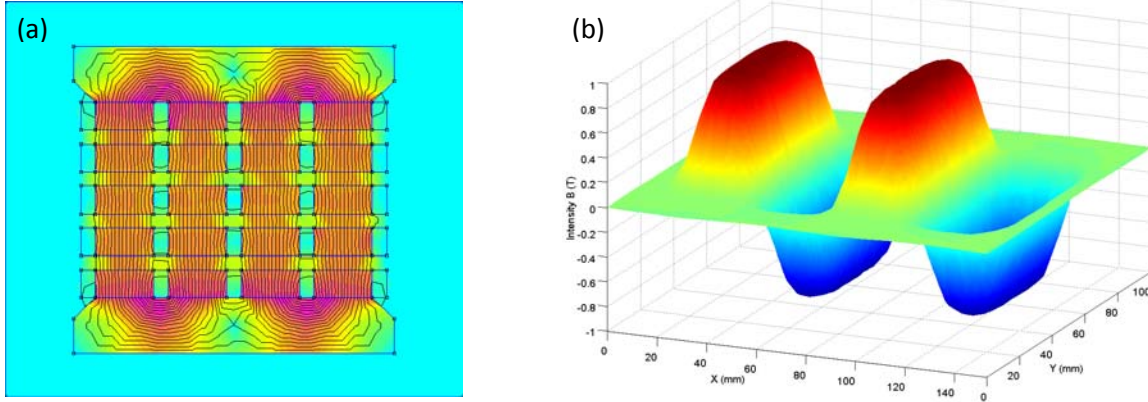


Figure 6.21 Finite element analysis of magnetic field, (a) Top view of magnetic flux loops. (b) Magnetic flux density  $B_p$  distributed on the coil plate.

The following is a first-order analysis about the power harvesting and the key parameters. The EMF voltage  $V$  [V] generated by a conductor of length  $l_e$  [m] moving in a constant magnetic field  $B$  [T], at a constant velocity  $v$  [m/s] is given by

$$V = Bv l_e \quad (5.8)$$

The maximum current,  $I$  [A], generated by the device with short circuit can be expressed by:

$$I = \sigma B_p v_r A_w \frac{l_e}{l_f} \quad (5.9)$$

where  $\sigma$  is the electrical conductivity [ $\Omega/m$ ] of the conductor,  $B_p$  is the magnetic field intensity in the perpendicular direction of the coil plate,  $v_r$  is the constant relative velocity [m/s] of the conductor in the axial direction moving in the magnetic field, and  $A_w$  is the cross-sectional area [ $m^2$ ] of the wire,  $l_e$  is the effective length of coil moving in the magnetic field and  $l_f$  is the full length of the coil including the part that is not in the magnetic field. The peak power,  $P$ , is calculated by combining Equations (5.8) and (5.9):

$$P = VI = B_p^2 v_r^2 \sigma A_w \frac{l_e^2}{l_f} \quad (5.10)$$

Equation (5.10) shows the importance of magnetic flux density. A double increase in  $B_r$  results in a quadratic increase in  $P$ . Therefore, the energy harvester is designed to have high magnetic flux by effectively using permanent magnets with high magnetically permeable materials.

The coil assembly consists of a support plastic frame and multiple coil windings. The frame is made of plastic with high electrical resistance, to eliminate eddy current energy loss. The shape and winding of the coil is also design to follow the eddy current loop showing in Figure 5.22, in order to achieve the shortest loop for the current with minimum resistance. The width of one coil equals to the width of two magnets. As a first-order approximation, it is assumed  $L_c$  is in the field, and  $R_c$  is not. The total number of coils is 8. The coil thickness is 4.76mm, which was determined by the gap between the magnets. A copper coil with gauge of 10AWG was used based on Equation (5.8) and denoting  $l_e$  and  $l_f$  as

$$\begin{cases} l_e = 2NL_c \\ l_f = 2N(\pi R_c + L_c) \end{cases} \quad (5.11)$$

where  $R_c$  is the parameters shown in Figure 5.23, and  $N$  is the number of turns which is defined as

$$N = \frac{\pi}{2\sqrt{3}} \frac{A_c}{A_w} = \frac{\pi}{2\sqrt{3}} \frac{4A_c}{\pi d^2} = \frac{2T_m W_m}{\sqrt{3}d^2} \quad (5.12)$$

where  $d$  is the diameter of the wire,  $A_c$  and  $A_w$  are the cross-sectional area of the coil and wire and  $T_m$  is the thickness of the coil. Thus,

$$V = \frac{4B_r v_z T_m W_m L_c}{\sqrt{3}d^2} \quad (5.13)$$

$$P = \frac{\pi \sigma B_r^2 v_z^2 T_m W_m L_c^2}{\sqrt{3}(\pi R_c + L_c)} \quad (5.14)$$

The peak output voltage is inversely proportional to the square of the wire diameter, and the peak power will only depend on the total volume of conducting material in the coils. We can also see that the power is proportional to the square of the magnetic flux density  $B_p$ , so it is critical to have a large flux density  $B_p$ , which is achieve by choosing high-intensity rare-earth magnets and by designing low reluctance magnetic loops.



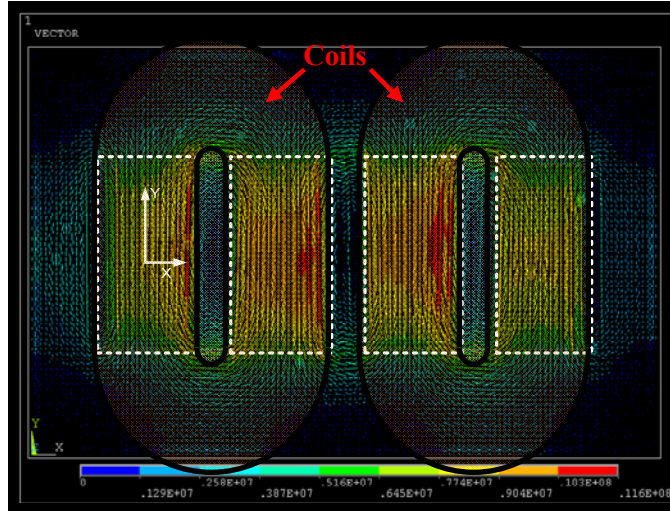


Figure 6.22 The coils are designed to follow the main eddy current loops.

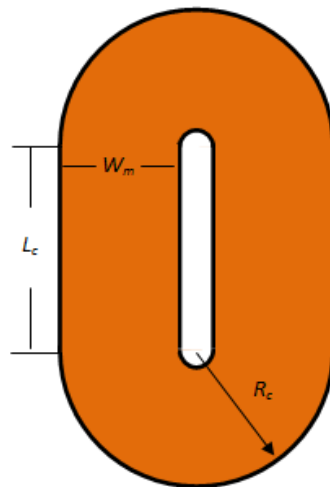


Figure 6.23 Dimensions of the coil and magnets.

## 6.2.2 Experimental Characterization of Linear Energy Harvesters

In this experiment, the actual magnetic flux density inside the coil plate is measured to verify the FEA result. Magnetic flux densities in both the horizontal and vertical directions are measured using a Teslameter (Lake Shore 410), the results of which are shown in Figure 5.24, as well as the FEA result for comparison. From Figure 5.24, it can be seen that measurement and FEA result matches very well and a very strong magnetic flux density up to 0.9T are obtained.

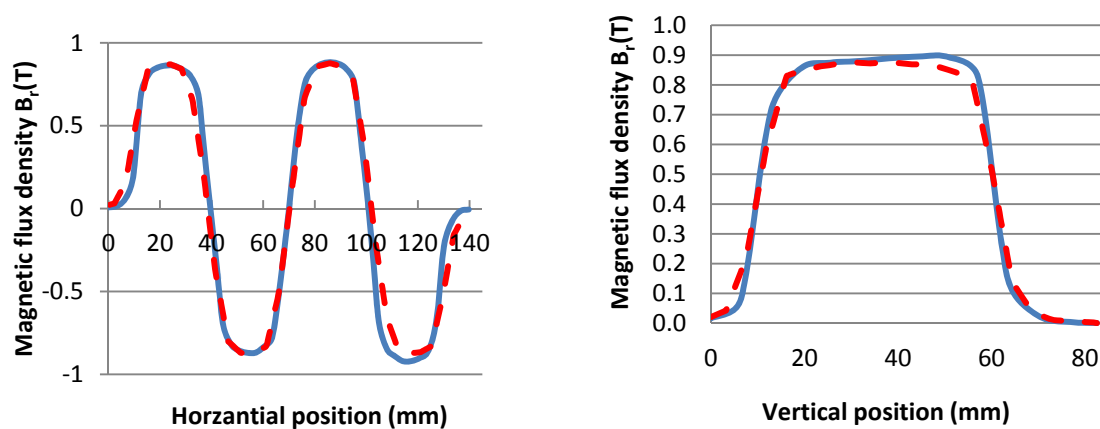


Figure 6.24 Measured (solid) and calculated (dashed) magnetic flux density  $B_p$  along the center of the coil plate in the horizontal and vertical directions.

Figure 5.25 shows the time response of the vibration energy harvester under 10Hz harmonic force excitation. Since the electromagnetic harvester has  $70 \Omega$  internal resistance, the harvester are shunt with  $70 \Omega$  external resistor to achieve maximum power. It should be noted that the energy harvesting circuit can be modeled as a resistive load. So different resistor are used to estimate the power and damping capacity of the harvester. Under the 2.54mm peak-to-peak harmonic vibration, the harvester can generate 18.5V peak-to-peak voltage and 116N peak-to-peak damping force. The peak power harvested is 1.24W, the total power dissipated by the vibration energy harvester is 2.48W. The corresponding damping coefficient of this set-up is 727.3 Ns/m and 425 kNs/m<sup>4</sup>damping density.

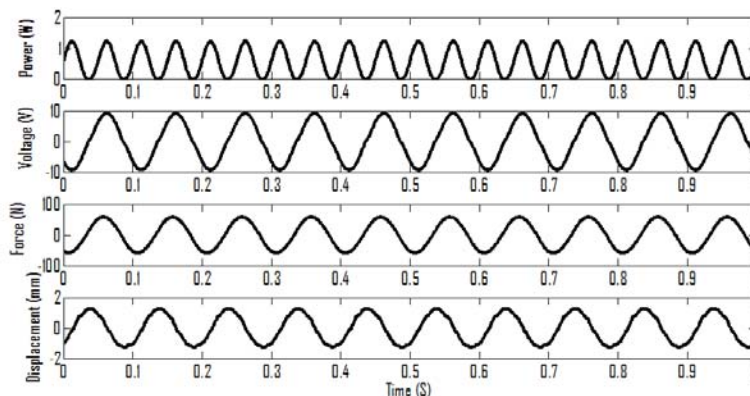


Figure 6.25 Time response of the vibration energy harvester under 10Hz excitation.

Figure 5.26 shows the RMS voltage and power harvested at different harmonic force driving amplitude at 10Hz. In this figure, the harvester is also shunted with a 70  $\Omega$  resistor. About 15 RMS voltage and 3.2W power can be generated at obtained at 6mm peak-to-peak amplitude, which is corresponding to 0.27m/s RMS velocity.

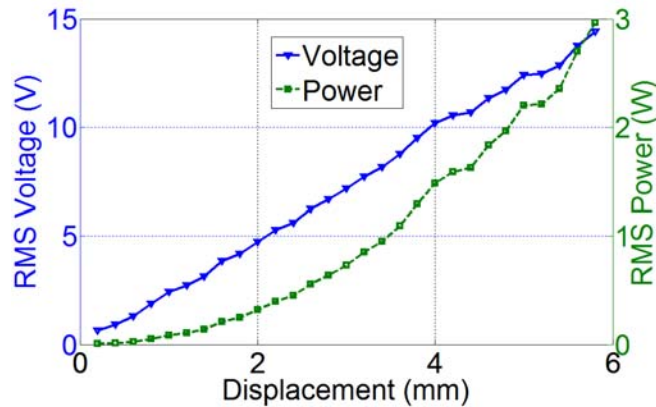


Figure 6.26 RMS voltage under 10Hz harmonic excitation with different amplitudes.

Figure 5.27(b) further show the damping loop under 10Hz force harmonic excitation with different external resistance load. namely open circuit, 200  $\Omega$ , 70  $\Omega$ , 20  $\Omega$  and short circuit. When it is open-circuit, the system still has damping due to the grease applied between the coil plate and magnets array. When it is short-circuit, the harvester will provide 1091 damping coefficient, however no energy is harvested. When shunt with 70  $\Omega$ , maximum harvesting power is achieved while providing 727.3 Ns/m damping to the system. Shunt with 200  $\Omega$ , 0.45W power is harvested and 633Ns/m is obtained. Shunt with 20  $\Omega$ , 0.38W power is harvested and 890Ns/m is obtained. The detailed result is also summarized in Table 4.4. By switching the resistive load connected to vibration energy harvester, the damping coefficient can be changed accordingly, which mean the harvester can be implemented with different semi-active vibration control algorithms to achieve better vibration mitigation performance. Figure 5.27(a) and (c) further show the damping loop under 5Hz and 10Hz force harmonic excitation with different external resistance loads.

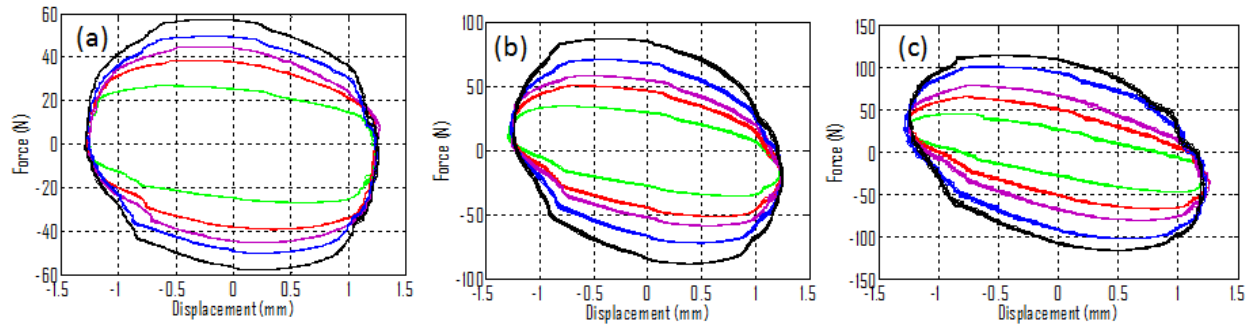


Figure 6.27 Damping loop under harmonic excitation with different external resistor, namely open circuit (green curve), 200  $\Omega$  (red curve), 70  $\Omega$  (purple curve), 20  $\Omega$  (blue curve) and short circuit (black curve): (a)5Hz, (b)10Hz, (b)15Hz.

Table 6.4 Damping achieved and power harvested with different external restive load

	Damping Coefficient (Ns/m)	Damping Density (kNs/m <sup>4</sup> )	Power Harvested (W)	Power Density ( $\mu$ W/cm <sup>3</sup> )
Open circuit	438	256	N/A	N/A
200 $\Omega$	633	370	0.45	263
70 $\Omega$	727	425	0.58	339
20 $\Omega$	890	521	0.38	222
Short circuit	1091	638	N/A	N/A

To explore how much the maximum damping coefficient we can achieve with this magnetic configuration, we also designed an eddy current with high damping density by replacing the coil plate with the copper plate, as shown in Figure 5.28. When the copper plate moves in a magnetic field, eddy currents will be induced in copper plates and a magnetic drag force damping force will be generated, which will also dissipate the kinetic energy into heat. We choose copper as the conductor materials because of high electrical conductivity ( $\sigma=5.8e7$  / $\Omega$ m). The size of the copper plate is 6"x4"x0.187" (153mm  $\times$  100mm  $\times$  t=4.75mm). The effective area of the magnets is 0.051m<sup>2</sup>, close to 1/3 of the total area of the conductor plate. The eddy current loop is shown in Figure 5.22, and detailed discussion on this eddy current damper can be found in (Zuo *et al.*, 2009). The damping loop of the eddy current with 5Hz harmonic force excitation is shown in Figure 5.29. The equivalent damping coefficient is about 2500Ns/m, which is corresponding to

1462 kN/m<sup>4</sup> damper density. It is about 5 times more than the typical eddy current dampers (Zuo *et al.*, 2009)). The damping density is comparable to the oil dampers. It should be noted the damping coefficient is dependent on the excitation frequency as well (Zuo *et al.*, 2009).



Figure 6.28 Copper plate of the eddy current damper.

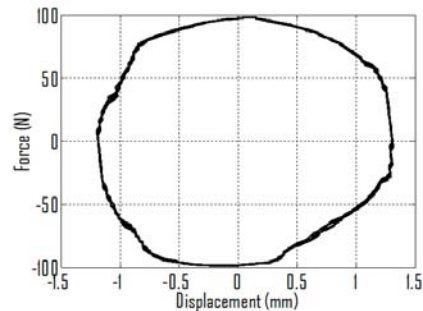


Figure 6.29 Damping loop under 5Hz harmonic excitation.

### 6.3 Harvester Using Rotation Motor and Rack-Pinion Mechanism

As we discussed in this chapter, by proposing new configurations or optimized the parameters, the magnetic flux density and power density of the linear electromagnetic harvester can be improved. Although linear electromagnetic motors have the advantage of being easily and reliably integrated into most existing vibration systems without the requirement for transmission mechanism, their efficiency is relative low and their size is still large, because of the relative low vibration velocity. Hence, another vibration energy harvester using a rotational brushed DC motor and rack-pinion mechanism, as shown in Figure 5.30, is developed and installed in a three-story building for the experimental study in the next chapter. The TMD mass is supported by a two flexible beam structures, which can provide large stiffness in vertical direction to support the gravity load and smooth motion in the horizontal direction with very little friction. The spring

was tuned to have the optimal stiffness. A rack-pinion mechanism is used to transfer the linear motion to the rotation of a geared motor.

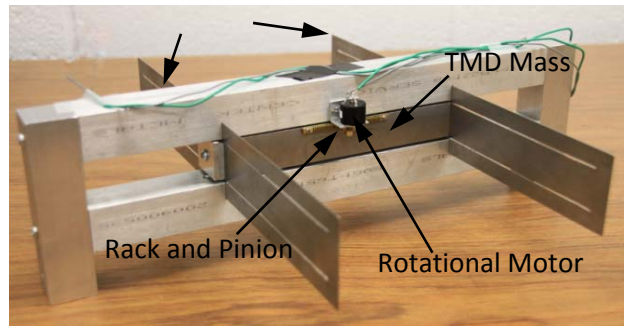


Figure 6.30 regenerative TMD using a rotational brushed DC motor and rack-pinion mechanism.

## 6.4 Summary

In this Chapter, we improve the power densities of linear electromagnetic transducers (LETs) for vibration energy harvesting by optimizing the key parameters and designing new configurations. The parameters of LETs with traditional configurations using FEA are studied, where the results show the power density of the optimized LET can be increased to 3.8 times, compared with the previous design (Zuo *et al.*, 2011). New configurations using double-layer configurations and a combination of axial and radial magnets are also proposed, and it is found that radial magnets made significant improvement to the power density. The double-layer configuration with axial and radial magnets can dramatically increase high radial magnetic flux density and power density. The average magnetic flux density is up to 1.01T, the peak magnetic flux density is over 1.51 T. The power density is  $27.2 \times 10^4 \text{ W/m}^3$  at 0.25m/s RMS velocity, and the damping density is improved to  $4357 \text{ kN}\cdot\text{s/m}^4$  (with short circuit), which is close to the oil dampers currently used in the engineering practice. With high energy density, the proposed LETs have promising applications in large-scale energy harvesting from civil structures. A prototype of 2.5 inches (63.5mm) overall diameter and 12 inches (305mm) compressed length was built and tested at different excitation conditions. It can provide up to 940Ns/m damping coefficient and harvest 2.8W power at 0.11m/s relative velocity. It is predicted based experiments that an electrical power 20.8W can be harvested on a matching external load at 0.25 m/s velocity for a single-layer LET of 3" out diameter and 12" compressed length with axial magnets, and the corresponding damping coefficient is 1354 Nm/s. Average 26W and 33W electrical power can be harvested for

the single-layer and double-layer LETs with combined axial and radial magnets at 0.25 m/s velocity, and the responding damping coefficients are 1680 and 2142 Ns/m. A cubic linear energy harvesting with very high power density is also designed and analyzed in this chapter. The alternating magnets direction configuration and the short magnetic flux loop make the magnetic flux density up to 0.9T. Power density up to  $725 \mu\text{W}/\text{cm}^3$  at 15HZ harmonic force excitation of 2.54mm peak-to-peak amplitude and damping density up to  $638 \text{ kNs}/\text{m}^4$  are achieved. To further explore the maximum damping capacity of this magnets configuration, an eddy current is designed and high damping coefficient of 2500Ns/m and  $1462 \text{ kNs}/\text{m}^4$  damping density is achieved although no power is harvested. Through the investigation in this chapter, we can conclude that the electromagnetic linear energy harvester is the solution to convert the vibration energy into electricity and control the vibration at the same time.

## Chapter 6

# Simultaneous Vibration Control Energy Harvesting

In this chapter, different vibration control algorithms, namely, semi-active, self-powered active vibration control algorithms will be presented with simulation results. Besides, the passive-matching regenerative control is demonstrated by the experimental result on a three-storey building prototype. The results show that the advanced vibration control algorithms will provide better vibration mitigation performances when compared with the passive TMDs. In addition to the better vibration reduction, the control algorithm also enables simultaneous energy harvesting from the structure.

### 7.1 Energy Harvesting Circuit

In energy harvesting system, the power electronic circuits have four main functions: (1). to regulate the AC harvested power to DC with a voltage suitable for the load or energy storage device; (2). to enhance the harvesting efficiency. In most situations, the vibration level is always varying, resulting in the low efficiency of circuit with fixed parameters optimized for certain vibration level. Power electronic circuits with controllable parameters are able to improve the energy efficiency by adaptively changing certain parameters according to the vibration level or external load (Ottman *et al.*, 2002, 2003). (3), to control the vibration, which is a special issue when active control is adopted. (4). to manage the power flow.

Typically, the power electronic circuits in vibration energy harvesting consist of rectifier, DC-DC converter, and energy storage device or grid tie inverters, as shown in Figure 6.1. The



different circuit corresponding to different vibration control algorithms will be discussed in the following section.

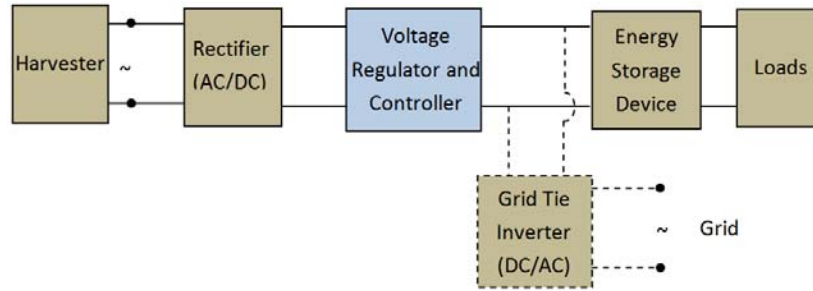


Figure 7.1 Typical power electronic circuit in vibration energy harvesting.

## 7.2 Vibration Control Algorithms

### 7.2.1 Active TMD and Series TMD using LQG control design

In this chapter, further studies and comparison of classic TMD and series TMDs are carried out in not only passive, but also active and semi-active configurations.

Traditional active TMD usually requires very large actuation force. For example, the two active TMDs installed in the Applause Tower (161m height) require two 5 tons actuation forces (Sun *et al.*, 1995). We will see that the proposed active series TMDs reduced the actuation force significantly while providing the same performance as the active classic TMD.

As we discussed Chapter 3, for the optimal series two TMDs with optimal mass distribution, the damping coefficient of  $c_1$  is always zero. Hence, only one actuator is used to replace the damper  $c_2$ . The configurations of active TMD and active series TMDs are shown in Figure 6.2. The primary structure is subjected to the wind load disturbance  $F$ . The actuation force is  $u_a$ . Both the system dynamics equations can be written in the form of:

$$M\ddot{x}(t) + Kx(t) + C\dot{x}(t) = GF(t) + Hu_a(t) \quad (6.1)$$

which can be further written in the state space form:

$$\dot{q}(t) = Aq(t) + B_f F + B_u u_a \quad (6.2)$$

where  $A = \begin{bmatrix} 0 & I \\ -M^{-1}K & -M^{-1}C \end{bmatrix}$ ,  $B_f = \begin{bmatrix} 0 \\ M^{-1}G \end{bmatrix}$ ,  $B_u = \begin{bmatrix} 0 \\ M^{-1}H \end{bmatrix}$ .

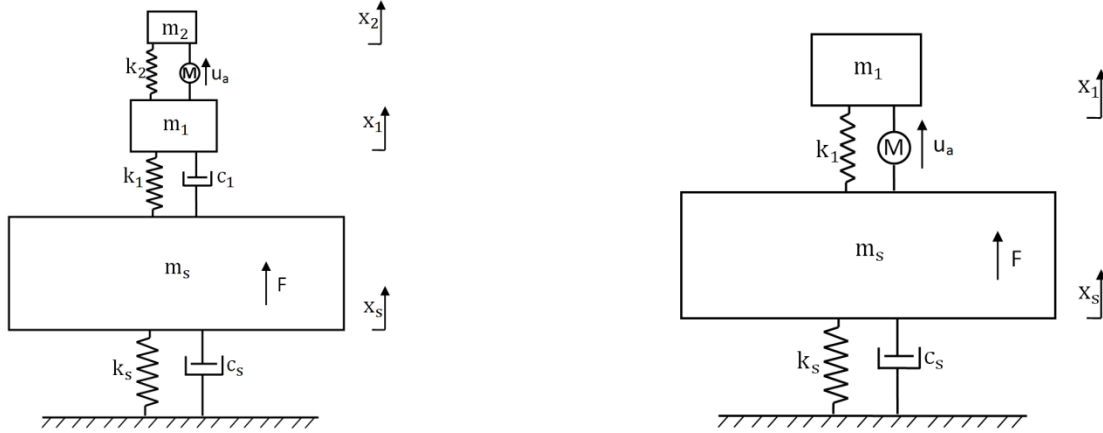


Figure 7.2 Active series TMDs and active classic TMD.

Tall buildings are usually subjected to tremendous wind load disturbance, which counts as the main reason for the overall vibration of the building (Kareem *et al.*, 1999). The amplitude of dynamic wind load on the structures can be calculated by the following equation (Rao, 2003):

$$\mathbf{F} = \frac{1}{2} \rho A V^2 C_d \quad (6.3)$$

where  $\rho$  is the air density,  $V$  is the wind speed, and  $A$  is the projected area perpendicular to the wind velocity,  $C_d$  is the object's drag coefficient, which depends on the shape of the object (usually about 1 for a cylinder). The wind force is usually very large, for example, using Equation (6.3), the dynamic load of breeze at the speed of 12 MPH on a high-rise building of 1440ft height and slenderness (height to width) ratio 9 is estimated to be 400kN, or 40 tons. For simplification we assume the wind load is of Gaussian white noise. In this case, it is more suitable to use LQG or  $H_2$  control as the optimal control strategy. The feedback measurements we choose are the accelerations of the main structure and auxiliary masses. The procedures for active controller design of classic TMD and series TMDs are quite similar. Hence, they are discussed in a general form as follows.

The RMS value is used as the performance index to evaluate the output performance. The performance can be accelerations, displacement, velocity or the combination of those three. Hence the performance index is chosen as:

$$\mathbf{J} = \int_0^{\infty} (\mathbf{q}^T \mathbf{Q} \mathbf{q} + \mathbf{r} u_a^2) dt \quad (6.4)$$

where  $\mathbf{Q}$  and  $\mathbf{r}$  are time invariant weights of the state and control force to be chosen. By minimizing the quadratic cost, we can minimize the response to Gaussian white noise input.

The optimal control law is expressed:

$$\mathbf{u}_a = \mathbf{u}_{des} = -\mathbf{r}^{-1}\mathbf{B}_u^T\mathbf{S}\mathbf{q}(t) = -\mathbf{K}\mathbf{q}(t) \quad (6.5)$$

where S is the solution of the algebraic Riccati Equation (ARE):

$$\mathbf{A}^T\mathbf{S} + \mathbf{S}\mathbf{A} - \mathbf{S}\mathbf{B}_u\mathbf{r}^{-1}\mathbf{B}_u^T\mathbf{S} + \mathbf{Q} = \mathbf{0} \quad (6.6)$$

Since we use acceleration feedback, not all the states are available. Linear-quadratic-Gaussian (LQG) state-estimator is employed to estimate the state vector  $\mathbf{q}(t)$ . The feedback measurement  $\mathbf{y}(t)$  can be expressed in the form of

$$\mathbf{y}(t) = \mathbf{C}_1\mathbf{q}(t) + \mathbf{D}_{12}\mathbf{F} + \mathbf{D}_{11}\mathbf{u} \quad (6.7)$$

This LQG state-estimator is so called Kalman filter, the equation of which can be expressed as:

$$\dot{\tilde{\mathbf{q}}}(t) = \mathbf{A}\tilde{\mathbf{q}}(t) + \mathbf{B}_u\mathbf{u}_a + \mathbf{L}(\mathbf{y}(t) - \mathbf{C}_1\tilde{\mathbf{q}}(t) - \mathbf{D}_{12}\mathbf{u}_a) \quad (6.8)$$

where  $\tilde{\mathbf{q}}(t)$  is the estimated state vector. The observer gain matrix L is obtained as:

$$\mathbf{L} = \mathbf{P}\mathbf{C}_1^T\mathbf{V}^{-1} \quad (6.9)$$

where V is the covariance matrix of the measurement noise, and P is the solution of ARE:

$$\mathbf{A}\mathbf{P} + \mathbf{P}\mathbf{A}^T + \mathbf{B}_f\mathbf{Q}_N\mathbf{B}_f^T - \mathbf{P}\mathbf{C}_1^T\mathbf{V}^{-1}\mathbf{C}_1\mathbf{P} = \mathbf{0} \quad (6.10)$$

where  $\mathbf{Q}_N$  is the covariance matrix of the process noise.

Figure 6.3 shows the frequency response of active TMD and series TMDs of a building with 730 tons TMD, 0.146 Hz natural frequency, 0.78% modal mass ratio, where the output performances of the two kinds of TMDs are designed to be the same by adjust the weightings r. With the same output performance, the active series TMDs requires much smaller actuation force. The force ratio (actuation force/input force) in frequency domain is shown in Figure 6.4. As we can see from Figure 6.4, in the whole frequency range, the active series TMDs require much smaller force than the one of active TMD. Besides, the maximum force of active series TMDs is only 26% of the one of active TMD.

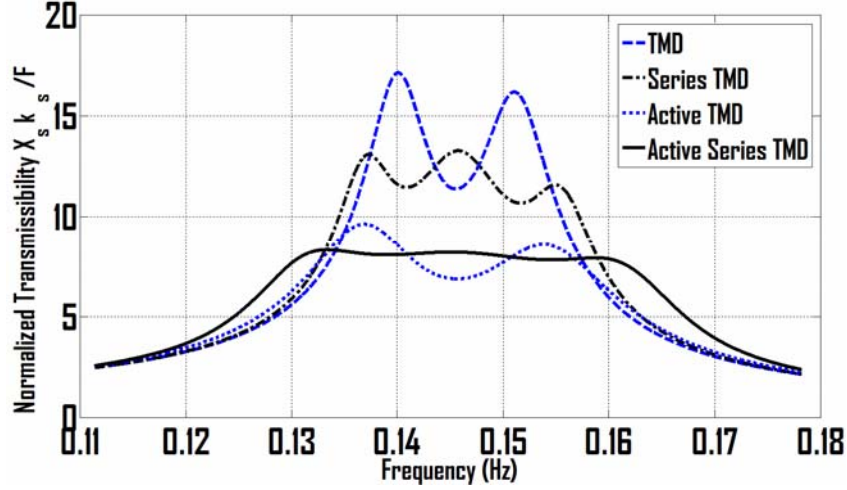


Figure 7.3 Frequency responses of structures with active series TMDs and active classic TMD.

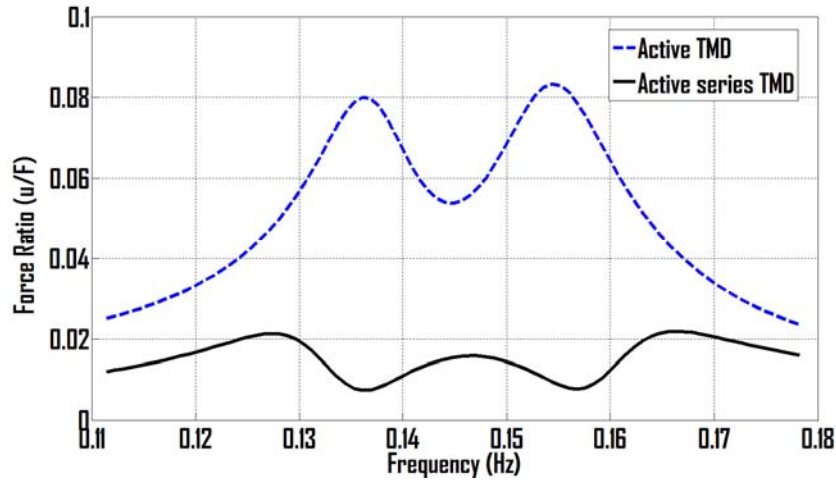


Figure 7.4 Force requirements of active TMD and series TMDs in the frequency domain to achieve comparable vibration suppressions.

### 7.2.2 Regenerative-Passive

The relative motion between the stator and mover of the motor can induce a voltage  $e_m$  in the coils, which is proportional to the relative velocity of stator and mover  $v$

$$e_m = k_e v \quad (6.11)$$

where  $k_e$  is the back electromotive voltage coefficient of the electromagnetic motor. Meanwhile, the current flow inside of the motor coil will induce a force proportional to the current, which serves as the damping force for the mechanical system:

$$f_d = k_t i \quad (6.12)$$

where  $k_t$  is thrust constant of electromagnetic motor.

The electromagnetic motor can be modeled as voltage source in series with the inherent inductance and resistor of the motor. If the inductor  $L_m$  of the motor is small and the two electrodes of the electromagnetic motor are shunted with a resistor  $R$ , the electromotive force will appear as an ideal viscous damping force:

$$f_d = \frac{k_e k_t}{R + R_m} v \quad (6.13)$$

where  $R_m$  is the resistance of coils of the electromagnetic motor. And in this case, the electrical energy is dissipated by the resistor into heat waste (Palomera, 2005). Pure resistance load also provides a method to measure and estimate the potential amount of energy in the energy harvesting system (Gupta *et al.*, 2006), although the practical loads are not always pure resistive. From equation (6.13), we can conclude the vibration can be controlled by adjust the electric load.

Motion magnification mechanism can be used to increase the efficiency of the electromagnetic motor based energy harvesting system. It may have the same effect as increasing the motor constant  $k_e$  and  $k_t$ , since when a magnification mechanism with the ratio of  $M$  is adopted, the induced electric voltage will be  $M$  times:

$$e_m = -M k_e v \quad (6.14)$$

At the same time, the force will be  $M$  times compared with the one without mechanism:

$$F_d = -M k_t i \quad (6.15)$$

From Equations (6.14) and (6.15), we can find the motion magnification  $M$  has influence on both the induced voltage and dynamics.

If the inductor  $L_m$  of the motor is small and the two electrodes of the electromagnetic motor are shunted with a resistor  $R$ , the maximum viscous damping coefficient that can be achieved will be:

$$c_m^{\max} = \frac{M^2 k_t k_e}{R_m} \quad (6.16)$$

### 7.2.3 Semi-active TMD and Series TMD

Although active TMD can provide better vibration mitigation performance than the passive one, at the cost of large amount energy, it is more complex and costly, which limits its practical implementations. Hence, semi-active TMDs are proposed to provide better vibration mitigation performance than the passive one without the drawbacks of active TMDs. In this section, a semi-active algorithm using clipped optimal control is applied both on classic TMD and series TMDs in order to compare their performance.

The optimal force obtained in Equation (6.5) cannot be fully implemented using semi-active force. However, the instantaneous force can be classified into two categories: active and passive. Here, we denote the active force  $u_a$  obtained in Section 5.2.1 as  $u_{des}$ . When the force  $u_{des}$  has the same direction as the relative velocity between the two masses  $v = \dot{x}_2 - \dot{x}_1$  in active series TMDs ( $v = \dot{x}_1 - \dot{x}_s$  in active classic TMD), the desired force  $u_{des}$  is active. When two directions are opposite, the force is essentially passive.

Therefore, the optimal desired force is clipped into two scenarios. 1). When the desired force  $u_{des}$  has the same direction as the relative velocity between the two masses, the actual force is set to be as small as possible. It can be realized by setting the electromagnetic motor into open circuit, then the damping force  $f_{min}$  will be just friction and eddy current damping force. 2). On the opposite, when the desired force and relative velocity have different directions, the essentially passive force will be realized by the electromagnetic motor, following the desired force obtained by active LQG controller design. Hence, based on the above three scenarios, the semi-active control law can be summarized as Equation (6.17):

$$\mathbf{u}_{semi} = \begin{cases} \mathbf{u}_{des}, & \text{for } |\mathbf{u}_{des}| < |\mathbf{f}_{max}|, \mathbf{u}_{des}\mathbf{v} < \mathbf{0} \\ -\text{sign}(\mathbf{v})\mathbf{f}_{min}, & \text{for } \mathbf{u}_{des}\mathbf{v} > \mathbf{0} \end{cases} \quad (6.17)$$

The final control law of the whole system is implemented by simulations based on the block diagram shown in Figure 6.5.

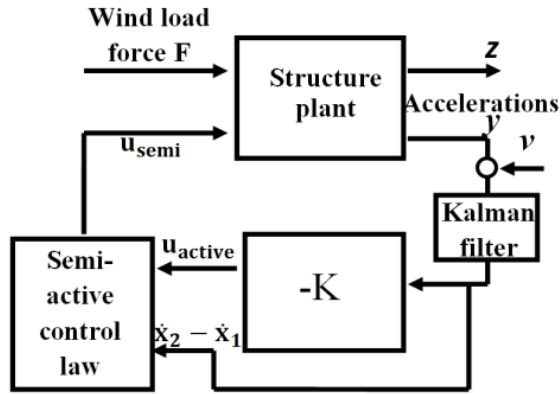


Figure 7.5 Block diagram of the semi-active series TMDs and classic TMD.

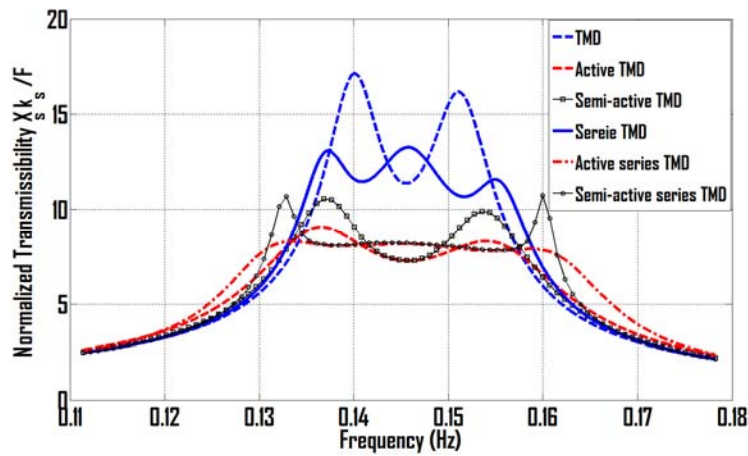


Figure 7.6 Frequency responses of structures with semi-active series TMDs and classic TMD.

Figure 6.6 shows the frequency response of semi-active TMD, where the clipped optimal control law of Equation (6.17) is used. As we can see from Figure 6.6, the performance is still much better than the passive configuration, even the desired is clipped. However, when the semi-active control law is applied on series TMDs, two peaks are introduced in the frequency domain because of the phase relation of the velocities of  $m_1$  and  $m_2$ , as also shown in Figure 6.6. However, in the frequency range from 0.136-0.157Hz, the performance is quite close to the one of active series TMDs.

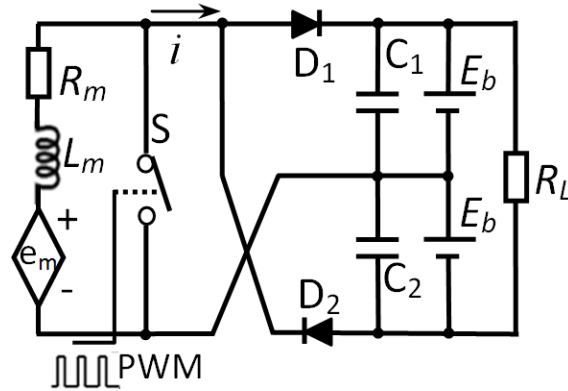


Figure 7.7 Energy harvesting circuit with both vibration damping force control and power regulation capabilities.

Figure 6.7 shows the proposed circuit for the simultaneous vibration control and energy harvesting implementation. The electromagnetic motor has inherent inductor  $L_m$  and resistor  $R_m$  connected in series. The circuit has both vibration damping force control and power regulation capacities. The switch S is controlled using PWM in a frequency that is several orders higher than the first natural frequency of the building. Hence, the vibration induced voltage  $e_m$  can be considered as static from the electrical circuit point of view. When the switch is ON, the electromagnetic motor tends to provide the maximum damping coefficient expressed by equation (6.16).

Meanwhile, the current flow inside the motor will increase to its maximum. When the switch is turned OFF, due to the effect of the inductance of the motor the current continues flowing through to charge the battery even when the voltage generated by the motor is less than the battery voltage  $E_b$ . However, the current will decrease. Such high frequency switching with different duty cycle will result in different mean current in the motor, which is corresponding to different damping forces. Since the switch frequency is several orders higher than the mechanical system, the mean force and current can be controlled in real-time. It should be noted that a similar circuit topology has been used in (Kim and Okada, 2002) for the purpose of eliminating the dead zone when the voltage generated by the motor is lower than the battery voltage and in (Dwari et al., 2008) for boosting the electricity from the low voltage to higher voltage. In this thesis, I will extend its potential to the semi-active force control.



In general, the dark area in Figure 6.8 shows the feasible force region when the damping force is controlled by the circuit in Figure 6.7. A maximum force limitation is applied in order to maintain the mechanical safety of the motor. When the amplitude of the relative velocity  $v_r$  is smaller than  $\frac{E_b}{Mk_e}$ , the minimum force is the 0, when the switch is always OFF. The maximum damping coefficient will be  $\frac{M^2k_tk_e}{R_m}$ , when the switch is always ON (equation 6.16). On the other hand, when the amplitude of  $v_r$  is larger than  $\frac{E_b}{Mk_e}$ , the minimum force will be  $\frac{M^2k_tk_e v_r}{R_m} - \frac{Mk_tE_b}{R_m}$ , when the switch is always OFF.

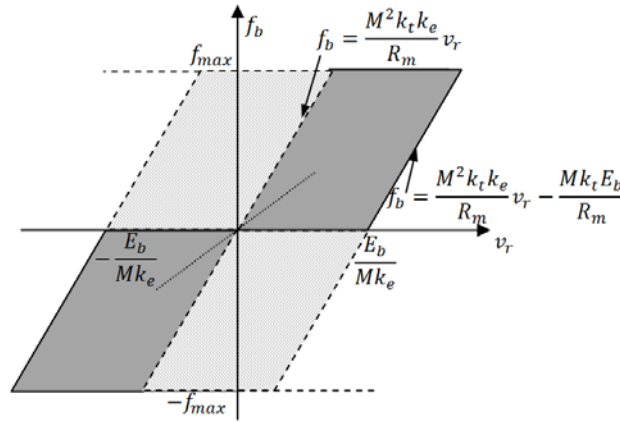


Figure 7.8 Feasible force region.

In fact, the harvested power can be further used for better vibration mitigation performance, resulting in a so-called self-powered active vibration control. In the regenerative semi-active control scheme, the active force is clipped to be zero when the relative velocity and desire force have the same direction. However, it has been shown that the active vibration control system using LQG control strategy is still dissipative in long time (Tang and Zuo, 2010b), which means the accumulated energy extracted from the system is larger than the accumulated energy for active control. Hence, self-powered active vibration control strategy can be developed to further reduce the vibration.

In order to realize the self-powered active vibration control, MOSFET switches are put in parallel with the diodes, where the MOSFET switches can be controlled by two PWM signals, as shown in Figure 6.9. In the energy harvesting mode, the MOSFET switches S1 and S2 remain off and the circuit becomes the same as the one in Figure 6.7. In the active vibration control

mode, the switches are controlled by PWM1 and PWM2. The circuit will serve as a class D amplifier, where the voltage applied on the electromagnetic motor can be controlled by the duty cycle of the two PWM signals to obtain desired driving forces. Positive and negative voltages can be applied on the motor by switching S1 or S2 on, respectively. The duty cycle the PWM controls the voltage amplitude on the electrodes of motor, thus control the driving force. The energy harvesting circuit shown in Figure 6.9 has controllable bidirectional current flow, which further enables the force in the light-dark area in Figure 6.8.

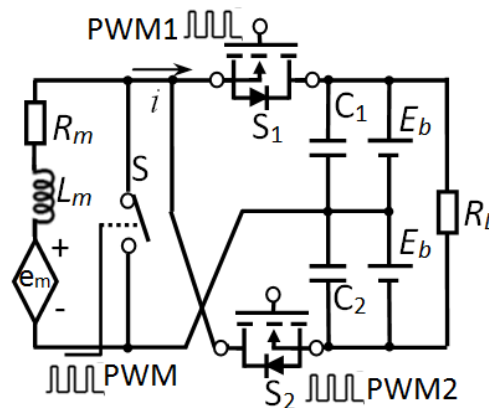


Figure 7.9 Modified energy harvesting circuit with self-powered active control capability.

### 7.2.4 Self-powered Active Vibration Control

In this section, we are discussing the realization of self-powered active TMD, where the harvested power is further used for active vibration control. The control strategies with the switches based circuit will be presented as well, which is capable of bi-directional power flow.

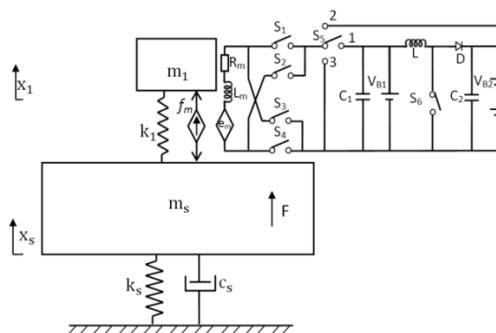


Figure 7.10 Schematic of the self-powered active TMD system.

Figure 6.10 shows the schematic of the self-powered active TMD, with the mechanical system coupled with electric circuit, which is controlled by the switches S1-S6. The electromagnetic

motor is modeling as a voltage source with the inherent conductor  $L_m$  and resistor  $R_m$  connected in series. The relative motion between the two masses can induce a voltage  $e_m$  in the coils, which is proportional to the relative velocity of stator and rotor  $v_r = \dot{x}_1 - \dot{x}_s$ .

The energy is harvested and stored in battery B1 at first with low voltage level and then the voltage is further boosted to charge the battery B2 of high voltage level, which is used to drive the motor when active force is required. The self-powered active TMD works in three different modes: (1). energy harvesting mode. When the desired force has the opposite direction of the relative velocity between the two masses, the desired force is essentially a passive force. In this mode, the electromagnetic motor works in driven mode, acting as energy harvester and the switch  $S_5$  is switched to contact 1. (2). driving mode. When the desired force has the same direction as the relative velocity, the desired force should be realized by active force. The electromagnetic motor works as actuator and  $S_5$  is switched to contact 2. (3). passive mode. The voltage generated by the electromagnetic motor maybe not large enough to overcome the battery voltage  $V_{B1}$ . The electromagnetic motor is set to be closed-circuit by switching  $S_5$  to contact 3. In these three modes, the control schemes of the switches  $S_1$ - $S_6$  are different.

### 7.2.4.1 Energy Harvesting Mode

When the desired force and the relative velocity have the opposite direction and the voltage generated by the electromagnetic mode is larger than the voltage of the first battery  $V_{B1}$ , the system will work in energy harvesting mode. In this mode,  $S_5$  is switched to contact 1. Energy is harvested and stored in battery  $B_1$  and booster DC-DC converter is used to step-up the voltage to further charge the battery  $B_2$  which has high voltage.

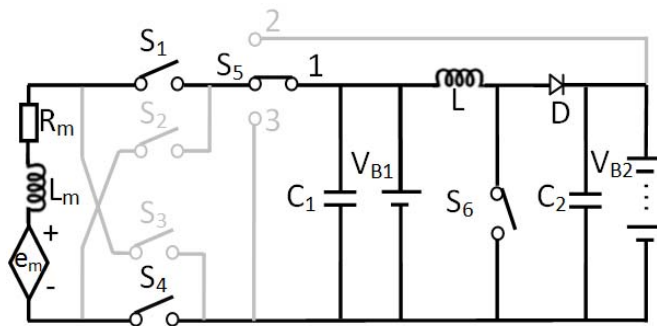


Figure 7.11 Energy harvesting mode ( $e_m > 0$ ).

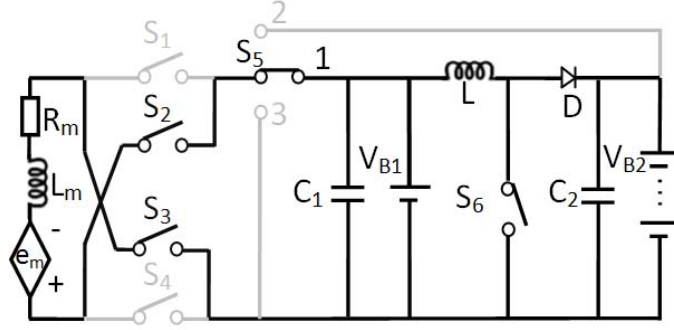


Figure 7.12 Energy harvesting mode ( $e_m < 0$ ).

Figures 6.11 and 6.12 show the circuit in this mode. Either switch pair  $S_1$  and  $S_4$ , or  $S_2$  and  $S_3$  is involved, since the direction of the relative velocity varies. In this way, the two switch pairs serve as synchronous rectifier. The corresponding passive force can be expressed as follows, when the inductance  $L_m$  is negligible:

$$f_m = -\mathbf{sign}(v_r) \frac{Mk_t(Mk_e|v_r| - V_{B1})}{R_m} \quad (6.18)$$

where  $\mathbf{sign}()$  is the signum function. In energy harvesting mode the passive force is composed of a viscous damping component  $-M^2k_t k_e v_r / R_m$  and a force  $\mathbf{sign}(v_r) V_{B1} / R_m$  due to the battery  $B_1$ . Vibration mitigation performance can be further improved, if the actual force can be controlled to follow the desired force, by applying Pulse-Width Modulation (PWM) to the switch pairs. Hence, the force provided by the electromagnetic motor can be controlled by adjusting the duty cycle of the switch pair  $S_1$  and  $S_4$ , or  $S_2$  and  $S_3$ . The work principle is similar to the switching amplifier. Hence the force can be expressed as:

$$f_m = -\mathbf{sign}(v_r) \frac{Mk_t(DMk_e|v_r| - V_{B1})}{R_m} \quad (6.19)$$

The duty cycle corresponding to the desired force  $u_{des}$  can be expressed as:

$$D = \frac{|u_{des}| R_m}{M^2 k_e k_t |v_r|} + \frac{V_{B1}}{Mk_t} \quad (6.10)$$

The passive damping force can be provided in this mode is limited due to the fact that  $D$  should be smaller than one. The damping force is set to be maximum ( $D=1$ ) when it is out of the limitation:

$$f_{mmax} = -\mathbf{sign}(v_r) \frac{Mk_t(Mk_e|v_r| - V_{B1})}{R_m} \quad (6.11)$$

### 7.2.4.2 Driving Mode

When the desired force and the relative velocity have the same direction, the self-powered active TMD will work in driving mode, where the electromagnetic motor acts as actuator. The circuit involved in this mode is actually class-D amplifier, where the direction and amplitude of the voltage applied on the electromagnetic motor can be controlled.

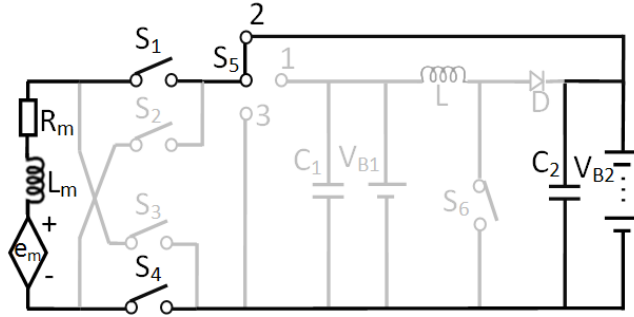


Figure 7.13 Driving mode ( $f_m > 0$ ).

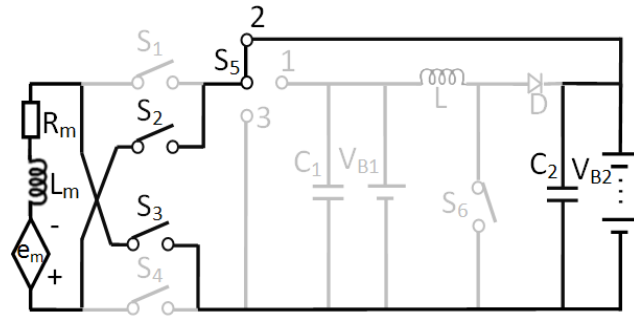


Figure 7.14 Driving mode ( $f_m < 0$ ).

As shown in Figures 6.13 and 6.14, the direction of the voltage is controlled by switching the two pairs of switches. The voltage amplitude is controlled by the duty cycle of the PWM applied on the switch pair. The circuit is class-D amplifier, the output voltage of which is proportional to the duty cycle. Hence, the output active force of the electromagnetic motor is:

$$f_m = \frac{Mk_t(DV_{B2} - Mk_e|v_r|)}{R_m} \quad (6.12)$$

The duty cycle provided by the controller in order to follow the corresponding desired force  $u_{des}$  can be expressed as:

$$D = \frac{|u_{des}|R_m}{Mk_tV_{B2}} + \frac{Mk_e|v_r|}{V_{B2}} \quad (6.13)$$

### 7.2.4.3 Passive Mode

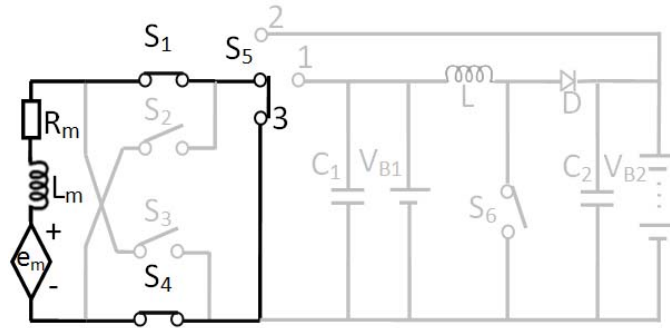


Figure 7.15 Passive mode.

When the desired force and the relative velocity have the opposite direction, however, the voltage generated by the electromagnetic motor is not large enough to overcome the voltage of the first battery  $V_{B1}$ , the system will work in this mode. In this mode, the switch  $S_1$  and  $S_4$  is switched on and  $S_5$  is switched to contact 3. In the passive mode, the electromotive force will appear to be an ideal viscous damping force:

$$f_m = \frac{M^2 k_t k_e v_r}{R_m} \quad (6.14)$$

### 7.2.4.4 Numerical Simulations

The simulations are carried out based on a building with 730 tons TMD, 0.146 Hz natural frequency, 0.78% modal mass ratio. And the damping ratio of the primary system is assumed to be 1% . For the electromagnetic motor, the thrust constant  $k_t$ , Back-EMF constant  $k_e$  and the resistance  $R_m$  are the inherent parameters of the electromagnetic motor. From the specification data of commercialized *IC44 series* linear electromagnetic motors manufactured by Kollmorgen ,  $k_t$  ranges from 72.7N/A to 1210 N/A,  $k_e$  ranges from 59.3V·s/m to 988 V·s/m,  $R_m$  ranges from 0.37Ω to 38.6Ω. Hence, in this simulation  $k_t$  and  $k_e$  are chosen to be 700N/A and 700V·s/m.  $R_m$  is 20 Ω and the motion magnification mechanism  $M$  is set to be 2. Figure 6.16 compares the transient response of the structure's acceleration when subjected to the random wind disturbance with the power spectral density of  $S_0=4.0 \times 10^{14} \text{ N}^2\text{s}$ . And the RMS of the output for structures with different TMDs is shown in Table 5.1. It should be noted that a low-pass filter is utilized when plotting Figure 6.16.

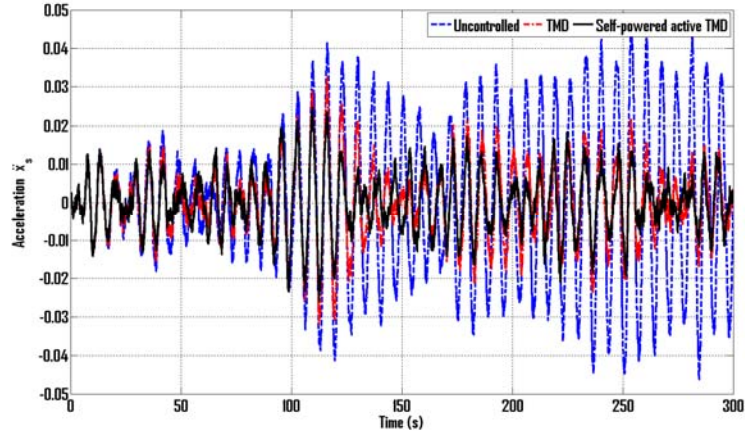


Figure 7.16 Transient acceleration response under random excitation.

Table 7.1 RMS acceleration of the building under random wind load excitation with the power spectral density of  $S_0=4.0 \times 10^{14} \text{ N}^2/\text{s}$

TMD type	RMS acceleration ( $\text{m/s}^2$ )	Normalized acceleration
Uncontrolled	0.018903	100%
TMD	0.008267	43.7%
Active TMD	0.006805	36.0%
Self-powered active TMD	0.007345	38.9%

Figure 6.17 shows the transient force response of self-powered TMD and the active TMD. As we can see from the figure, there are three types of forces expressed by Equations (6.19), (6.22), (6.24), corresponding to the three working modes: harvesting, driving, and passive.

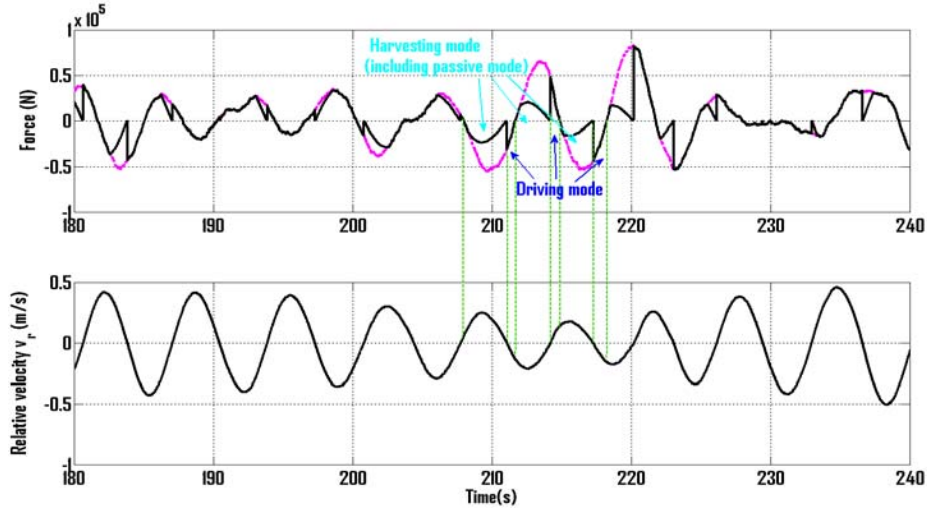


Figure 7.17 Transient force response under random excitation. (Passive mode is a small segment marked in the harvesting mode in this figure when the relative velocity  $|v_r|$  is less than  $Mk_e V_{B1}/R_m$ ).

Because of the nonlinearity of self-powered active control law, the system is no longer linear. However, we find that the excitation amplitude has little effect on the frequency response of transmissibility ratio, when the wind load disturbance is large. Figure 6.18 shows the transient response of the primary system subjected to harmonic excitation with a frequency of 0.146 Hz (natural frequency of the building) and amplitude of 250kN. As seen from Figure 6.19, the transient response of the self-powered active TMD can go into steady state after a few periods. This figure also indicates that at this frequency the self-powered active TMDs can reduce the vibration to 56.6% over the passive TMD. For this reason, we compare the frequency responses of transmissibility ratios of different TMDs. Figure 6.19 shows the frequency response of the self-powered TMD, compared with the passive and active TMD.



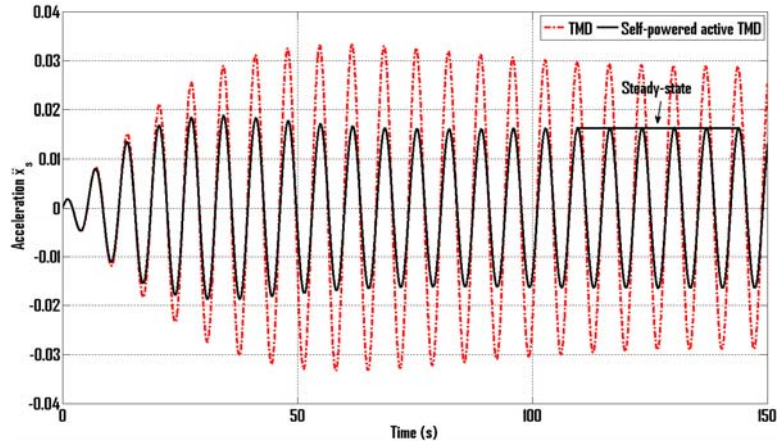


Figure 7.18 Transient response under harmonic excitation.

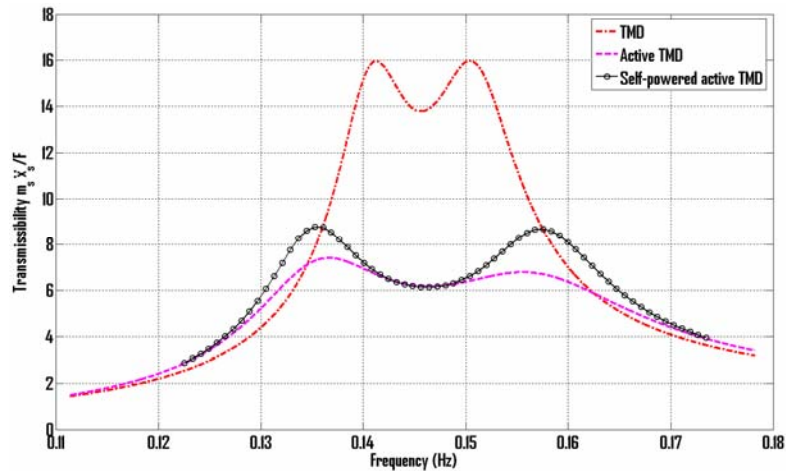


Figure 7.19 Frequency responses of transmissibility ratio.

The circuit is actually classic D amplifier in driving mode. The classic D amplifier has very high power conversion efficiency, usually  $>90\%$ . In the energy harvesting mode, the booster DC-DC converter has a typical efficiency of 78%, accounting for the main power loss. With taking both the self-powered active control law and parasitic power loss into account, we plotted the instant power and accumulated energy of the system in Figure 6.20 shows that the self-powered active control is still feasible when subjected to random disturbance with the power spectral density of  $S_0=4.0 \times 10^{14} \text{N}^2/\text{s}$ . The system can harvest more energy than needed for the active control part.

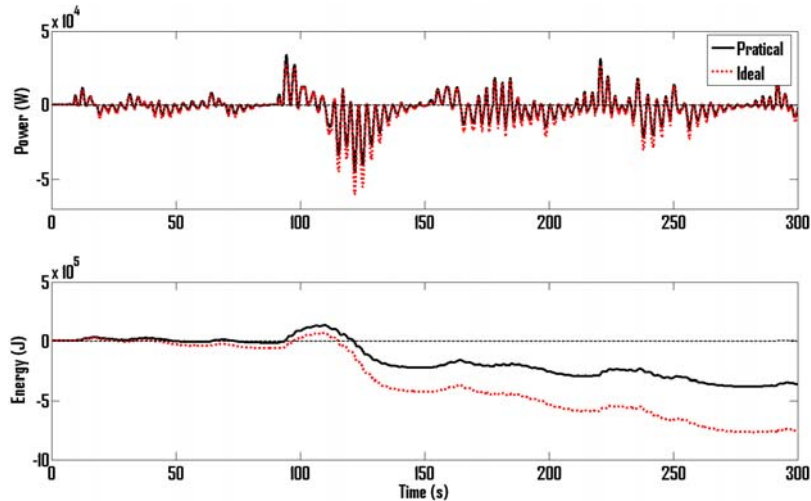


Figure 7.20 Power and energy transient response. The ideal case is the one doesn't consider the any power loss, while the practical take the efficiency of both harvesting and driving circuit into account.

## 7.2.5 Simulation and Experimental Results on a Three-story Building Prototype

### 7.2.5.1 Description of Building Prototype

A three-stories building prototype with regenerative TMD is built for demonstrating the feasibility of simultaneous energy harvesting and vibration control, as shown in Figure 6.21. The building prototype is 1.9m tall. It is supported by 4 beams with mass blocks located on the second, third and roof floor, respectively. It is built with aluminum, which totally weights 24kg.

The frequency response of the building without TMD is shown in Figure 6.22, which is measured using sweep sine excitations. It indicates the first three natural frequencies are 3.32 Hz, 10.66Hz and 16.29Hz, respectively.

The electromagnetic TMD system is shown in Figure 6.20 (b) and (c). The TMD mass is supported by a two flexible beam structures, which can provide large stiffness in vertical direction to support the gravity load and smooth motion in the horizontal direction with very little friction. A rack pinion mechanism is used to transfer the linear motion to the rotation of a geared motor.

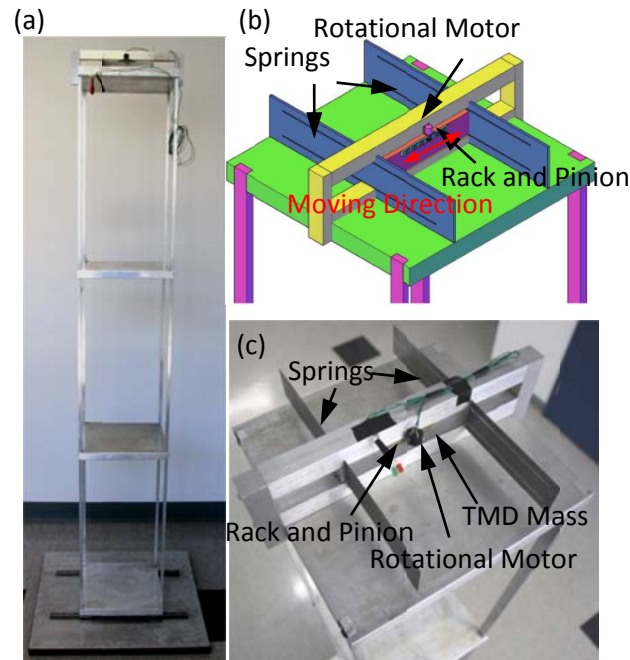


Figure 7.21 A 3-story building prototype with regenerative TMD: a), the whole view of the building; b), the 3-D drawing of the regenerative TMD, c), a close-up view of the TMD prototype.

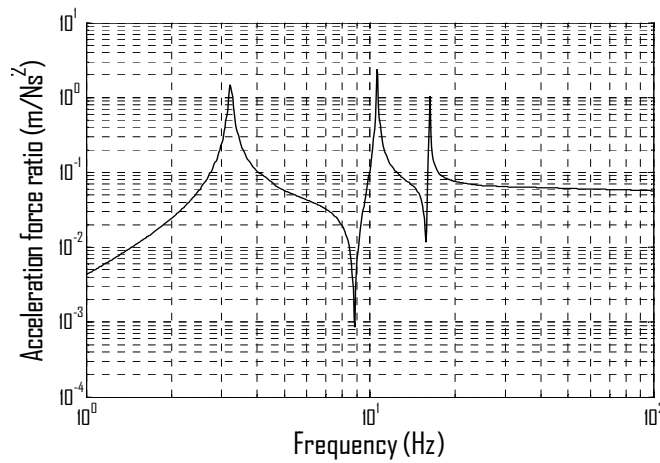


Figure 7.22 Measured frequency response of the 3-story building prototype without TMD.

### 7.2.5.2 Simulation Results of the Circuit

The circuits shown in Figure 6.7 have two main functions. One is controlling the input current in order to control the damping force provide by the motor (vibration mitigation). The other

function is regulating the voltage to charge the battery (energy harvesting). The simulations in this sub-section are to show the feasibility of the simultaneous damping force control and power regulation. The parameters of building prototype used for these simulations are listed in Table 6.2.

Table 7.2 Parameters used for simulation

Parameters	
EMF coefficient $k_e$	0.484mV/rpm
Thrust constant $k_t$	4.65mN/mA
Resistance of the motor $R_m$	54.7 $\Omega$
Inductance of motor $L_m$	1557 $\mu$ H
Gear ratio of motor $M$	13:1
Battery voltage $E_b$	3V
Modal mass of the building $m_s$	13.08
Mass ratio $\mu$	5.2%
Magnitude of wind force $F$	25N
First natural frequency of building	3.32Hz
Switching Frequency $f_s$	10kHz

The ability of damping force control can be demonstrated by the relation between the duty cycle and the current flow in the motor, as shown in Figure 6.23. It should be noted that the current is normalized by  $(L_m f_s + R_m)/E_b$  and the input voltage is normalized by  $E_b$ . The figure shows that the circuit is capable of controlling the current flow of the electromagnetic motor, which is corresponding to controlling the damping force. When the voltage generated by the electromagnetic motor is larger than the battery voltage (3V), the current/damping force changes linearly with the duty cycle, because the circuit always works in continuous mode. While the voltage is lower than the battery voltage, the current/damping force and duty cycle have different relations, because the circuit can work in both continuous and discontinuous modes. Similar conclusion about the relations of power harvested by the electromagnetic motor and duty cycle can be drawn from Figure 6.24.

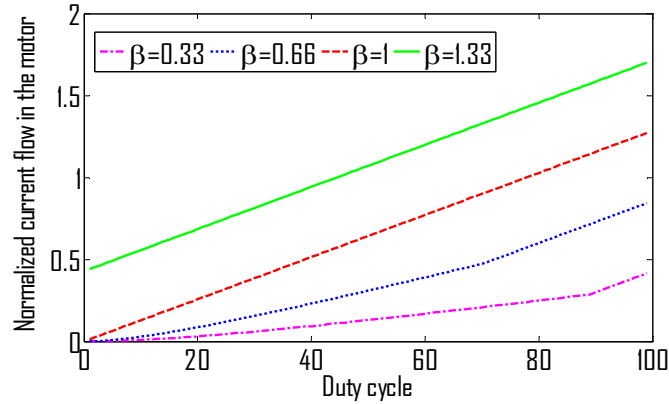


Figure 7.23 Current flow of the electromagnetic motor at different duty cycles.

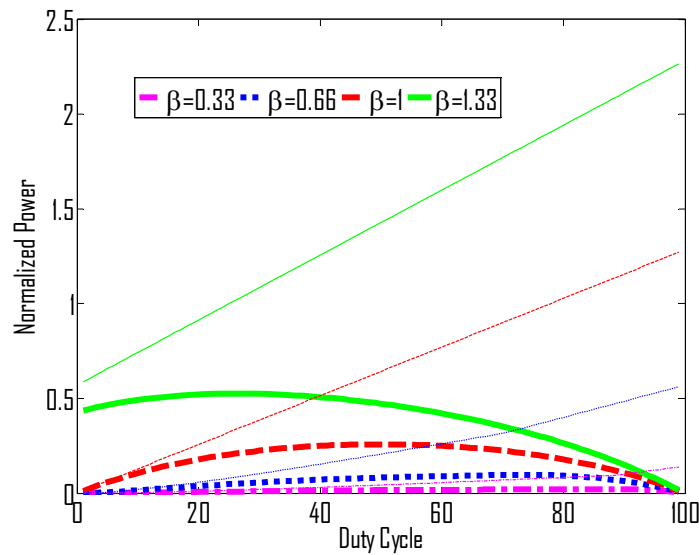


Figure 7.24. Power harvested by the motor (thinner lines) and stored in the battery (thicker lines) at different duty cycles.

Although the power extracted from the building by the electromagnetic motor increases with the duty cycle, the actual power harvested and stored by the battery doesn't follow this relationship. As shown by Figure 6.24, the power that charges the battery increases with the duty cycle at first then decreases with it. It should be noted the power is normalized by  $(L_m f_s + R_m)/E_b^2$ . There is an optimal duty cycle from the harvested power point of view. This may be useful for vibration energy harvesting where the vibration performance of the main structure itself is not concerned. Since the vibration mitigation is the priority for buildings, the duty cycle is determined by the desire force rather than harvesting power or power efficiency.

Figure 6.25 shows the efficiency of the energy harvesting circuit at different duty cycles. The efficiency decreases very quickly with the increase of duty cycle. It should be noted that the main power lost is the power dissipated by the inherent motor resistor. However, when working in low duty cycle condition the circuit still has higher efficiency than it is shunted with pure resistive load, which has 50% maximum efficiency. When the regenerated voltage is lower than the battery voltage, there is an optimal efficiency for the circuit. Similarly, this conclusion may be useful for the energy harvesting application where the vibration performance is not a concern and energy harvesting rate and energy efficiency is the priority. There is actually some theoretical analysis on deriving the optimal duty cycle for energy harvesting rate or energy efficiency (Ottman *et al.*, 2003; Zuo and Tang, 2009). It is also noted that the optimal duty cycle for maximum energy harvesting rate and maximum energy efficiency are different in this circuit.

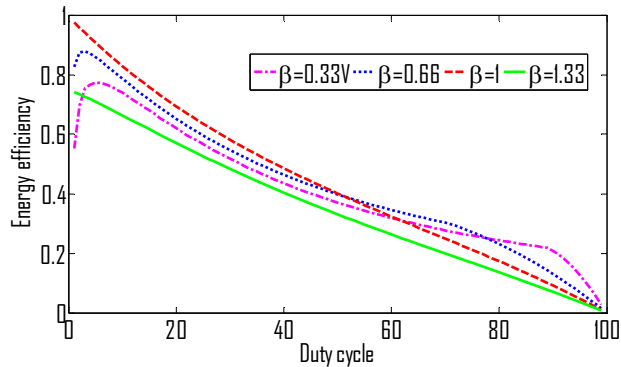


Figure 7.25 Efficiency of the energy harvesting circuit at different duty cycles.

### 7.2.5.3 Simulation Results of TMD with Clipped LQG Semi-active and Self-powered Controls

In this sub-section, simulations are carried out to show the effectiveness of semi-active and self-powered active control strategies designed based on clipped LQG method on the vibration mitigate performance. It should be noted that the steady state responses of the semi-active system subjected to a harmonic excitation without damping or force maximum limit are also periodic of the same frequency, which means the system is piecewise linear and the frequency response of the system can be plotted (Hac and Youn, 1992; Pinkaew and Fujino, 2001). However, the force constraints like Figure 6.8 will introduce nonlinearity to the system (Tang and Zuo, 2010a, 2010b). Yet, the frequency response can still be used to reasonably illustrate the effectiveness semi-active TMD, though not strictly.

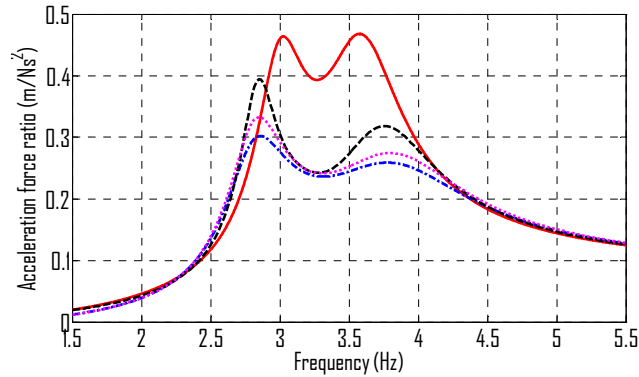


Figure 7.26 Frequency response of passive, electricity-generating and active TMDs. ( — passive TMD, - - - regenerative semi-active TMD, ..... self-powered active TMD, - . - active TMD).

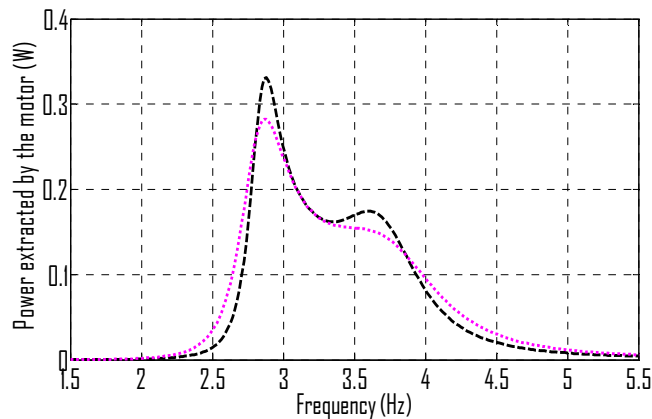


Figure 7.27 Power harvested by the motor in different control strategies. ( - - - regenerative semi-active TMD, ..... self-powered active TMD).

It can be seen from Figure 6.26, regenerative semi-active TMD can provide much better vibration mitigation performance than the optimal passive TMD. The performance of semi-active TMD is as good as the active TMDs. However, it can harvest energy rather than consuming energy. The self-powered active control strategy can provide better vibration mitigation performance than semi-active TMD in the sacrifice of partial harvested energy as shown by Figure 6.27. It should be noted that in the LQG controller design,  $\mathbf{Q}$  is defined such that the acceleration of the primary system as the performance index,  $r$  is defined to limit the maximum control force. In the simulation with self-powered active control, the active force has maximum limitation of 3.315N which is due to the limited 3V voltage battery.

#### 7.2.5.4 Experiments of Electricity-generating TMD

Experimental study is carried out to demonstrate the simultaneous energy harvesting and vibration control, based on the passive-matching regenerative TMD. To design the optimal tuning, we need to obtain the mass ratio  $\mu$ , which is the mass of the TMD over the first modal mass of the building. Generally the modal mass is not known exactly. We proposed a simple and yet effective engineering method to obtain the modal mass by experiment. Firstly, the mass of TMD is removed from the building prototype, and the systems natural frequency is measured  $\omega_1$  (3.32Hz for the prototype building). Then, by adding the TMD mass to the building and locking the TMD together with the building, we can obtain a new natural frequency of the building with additional TMD mass  $\omega_{12}$  (3.237Hz for the prototype building). By using the two measured frequencies, the mass ratio can be calculated using Equation (6.25).

$$\frac{\omega_1^2}{\omega_{12}^2} = \frac{\frac{k_1}{m_1}}{\frac{k_1}{m_1+m_2}} = 1 + \mu \quad (6.15)$$

Then three steps are taken to tuning the TMD: 1). Obtaining the mass ratio; 2). Tuning the frequency ratio by adjusting the mass; 3). Tuning the damping ratio via adjusting the duty cycle of the proposed energy harvesting circuit.

The mass of the TMD is 0.68kg. The mass ratio is calculated to be 5.2% and hence the actual modal mass of the building is 13.08Kg.

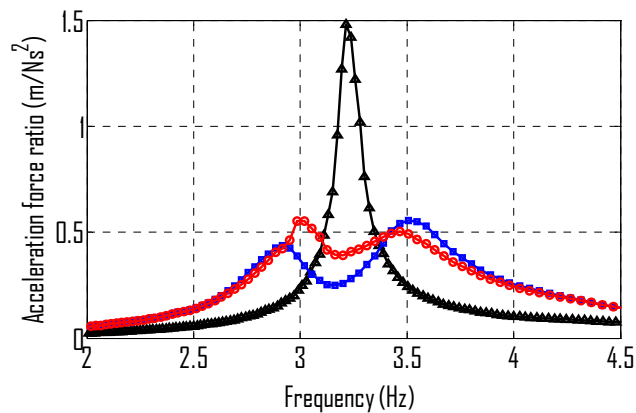



Figure 7.28 Measured frequency response of the prototype building. ( $\blacktriangle$  Frequency response of building without TMD,  $\ominus$  Frequency response of building with TMD tuned using resistor of



360Ω,  Frequency response of building with TMD tuned using the circuit shown in Figure 5.7, where the duty cycle of the switch is 10%).

The frequency response of the building prototype with TMD tuning by the switch circuit in Figure 6.7 is shown in Figure 6.28 with a fixed duty cycle 10%. The vibration is significantly reduced compared with the one without TMD. Figure 6.29 shows transient current flow in diode D1 with a duty cycle of 10% and the excitation is 15N harmonic force of 3.3Hz, where the effect of switch can be obviously seen. The mean value of the current over one vibration period is about 0.02A. The battery we used has 3V voltage. Hence the average power harvested is about 60mW, which means  $11.5 \times 10^{-3}$  normalized power when normalized to  $\frac{m_1}{\omega_s \sqrt{\mu}} |\ddot{x}_s|^2$ . It should be noted the peak acceleration of the building when the TMD is tuned using fix 10% duty cycle is  $5.19 \text{m/s}^2$ .

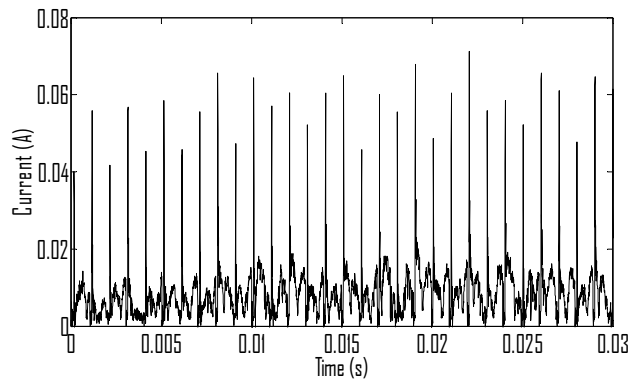


Figure 7.29 Measured instant electrical current that flows through the diode D1 to charge the battery.

As a comparison, we also directly tuned the damping by shunt the motor with the resistor, chosen as 360Ω by trial and error. The frequency response of building is also plotted and compared in Figure 6.30. As we can see from Figure 6.30, the vibration control effect of the TMD with electrical charging circuit is close to the one tuned by a resistor. There is still some difference, and the reason is because the switch circuit is essentially nonlinear and ideally the duty cycle should be controlled with feedback or feed-forward of the regenerated voltage  $e_m$  instead of being kept as a constant value.

In addition to the steady frequency response, we also experimentally studied the transient response of building with electricity-generating TMD. We pull the building to an initial position and release it. The transient vibrations are shown in Figure 6.31, from which we can see that the vibration is reduced very quickly in the case when TMD is tuned with resistor and duty cycle control respectively. After 1.5 second the higher mode vibration continues and lasts for longer time because TMD is designed for the first vibration mode only.

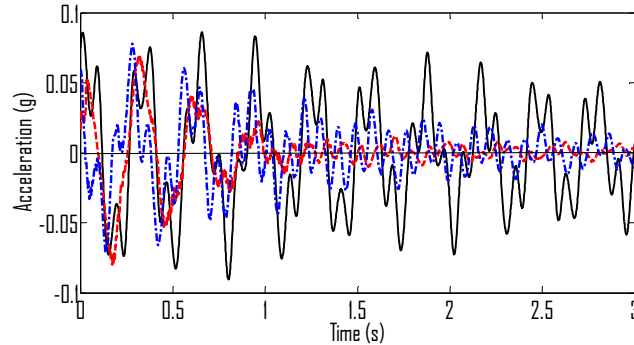


Figure 7.30 Measured transient acceleration response of the building. ( — Without TMD, - - With TMD tuned with optimal resistor, - . - With TMD tuned by duty cycle).

Figure 6.31 shows the voltage of the tuning resistor which is  $360\Omega$ . The electricity of up to 2 V voltage is generated while mitigating the vibration.

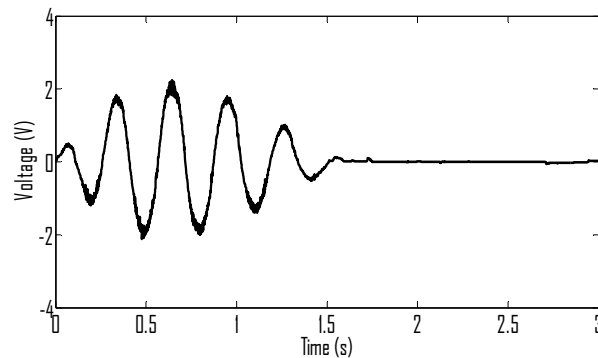


Figure 7.31 Measured voltage on the  $360\Omega$  resistor generated by the electromagnetic TMD.

Figure 6.32 shows the electrical current that charges the two 3V batteries in the transient response. Since the instant current charges the battery has very high frequency due to the effect of switching (as in Figure 6. 28), in Figure 6.32 we use the average current of time period 0.01s. About 5.85mJ energy charges the battery in this free vibration. Also from Figures 6.31 and 6.32,

we can find that almost no power is dissipated by the resistor or harvested after 1.5 second. This suggests that the relative motion between the TMD and building is stopped due to the static friction of the rack-pinion at low vibration amplitude. The vibration is then mitigated slowly by the inherent damping of the building prototype.

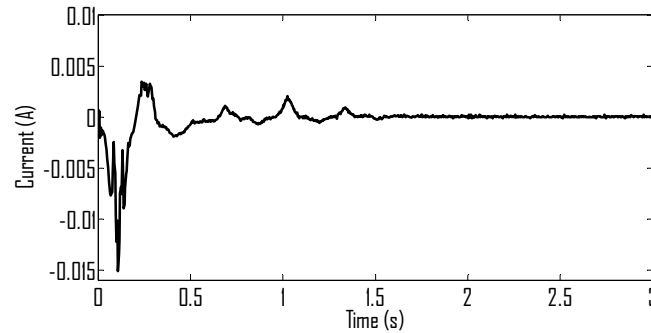


Figure 7.32 Measured transient average current  $i$  that charges the battery of the energy-generating TMD controlled by duty cycle.

### 7.3 Summary

This chapter investigated different control strategies for simultaneous energy harvesting and vibration control. First of all, performance of classic TMD and series TMD when implemented with active control algorithms are compared, the conclusion of which is that the series TMD would require smaller actuation force and large stroke than the classic one. The feasibility and realization of self-powered active control without consuming external energy, are proved in simulation. The proposed self-powered active TMD can provide better vibration mitigation performance compared with the passive TMD. Switch based circuits with capability of bi-directional power flow are presented for the implementation of self-powered active TMD. The power balance is analyzed with taking the efficiency of circuit and parasitic power loss into account. It also should be noted that a pre-charged energy reservoir may be used to jump-start the system before the system maintains the performance itself, but this pre-charged energy reservoir is not necessary. The regenerative semi-active control algorithm is also investigated in this chapter, using clipped LQG optimal control. The desired active force is first obtained and then clipped according to the constraints of semi-active control with force or damping coefficient limitation. Both the transient response to Gaussian white noise and harmonic excitation are

analyzed, and frequency response is plotted by extensive simulations. Significant vibration mitigation improvement has been found compared with classic TMD and series TMD. Moreover, large amount of energy can be harvested while we control the vibration. In addition, this chapter experimentally demonstrated the feasibility of simultaneous vibration control and energy harvesting from the building structure using regenerative electromagnetic TMD, where the desired damping is controlled using the proposed circuit with dual functions of force control and power regulation. 60mW energy is harvested when the prototype building is excited by a harmonic force with amplitude of 15N at 3.3Hz.

# Chapter7

## Conclusions and Future Work

In this thesis, I have presented the simultaneous vibration control and energy harvesting of tall buildings using electricity-generating TMD, with both simulation and experimental results.

### 8.1 Conclusions

I proposed and optimized several TMDs with novel configurations, namely electromagnetic TMD, series TMD and electromagnetic series TMD. The electromagnetic TMD can realize the effectiveness of classic TMD without adding auxiliary mass while harvesting energy. The series TMD and electromagnetic series TMD are more robust than the classic TMD. Their parameters are optimized either analytically or using decentralized control method.

Furthermore, the dynamics and energy analysis of structural vibration different TMD were carried out, the result of which shows that up to 300KW peak power is available in typical civil structures. I also designed and optimized electromagnetic harvesters with high power density, which has the potential for retrofit design. New configurations using double-layer configurations and a combination of axial and radial magnets are proposed, and it is found that radial magnets made significant improvement to the power density.

Different vibration control strategies namely, semi-active, self-powered active, and passive-matching regenerative are investigated, based on the proposed switching energy harvesting circuits, where better vibration mitigation performance has been observed compared with TMD using viscous dampers. The effectiveness of regenerative semi-active and self-powered active

control is shown by simulation where the controller is designed based on the clipped LQG method with practical force constraints. The regenerative semi-active control and self-powered active control can provide better vibration mitigation than the passive one. The simultaneous vibration control and energy harvesting is experimentally demonstrated using a three-story building prototype with electricity-generating TMD, where the desired damping is controlled by the proposed circuit with dual functions of force control and power regulation.

## **8.2 Future Work**

A three-story building and an energy harvesting circuit has been built in this thesis to show the feasibility of the simultaneous energy harvesting and vibration control. Significant efficiency improvement has been achieved by optimizing the vibration energy transducers in Chapter 5. Although, the current charging the battery and the power harvested is calculated, the efficiency of the transducer as well as the energy harvesting circuit is not analyzed. One important power loss is parasitic voltage-drops or the inherent resistances of the electronic components, or the power consumption by the controller. Techniques to reduce this voltage drop and the parasitic power consumption can be further investigated.

In this thesis, adjusting the duty cycle of the DC-DC converter is proved to be one way to control the actuation force in the semi-active and self-powered active control strategies. State-averaging method was used to model the DC-DC converter where the nonlinear dynamics of the converter is simplified. Further research on the more precise modeling of DC-DC booster converter can be investigated, as well as relevant control algorithms.

This thesis has optimized several different TMDs for better vibration mitigation performance. Since, energy harvesting is another task of this project, optimization for energy harvesting rate can be conducted in the future. The trade-off between energy harvesting rate and vibration mitigation performance can be considered as well.

In addition, vibration control is another particular challenge associated with large-scale energy harvesting. Quite different from the small-scale energy harvesting where the vibration of the host structure is not a concern, the priority in most large scale vibration harvesting is the protection of the mechanical systems and the human occupants or passengers during the vibration. I have studied the semi-active and self-powered active vibration control in Chapter 6. In the future, the

feasibility of putting energy harvesting rate and vibration mitigation as the performance index at the same time for a multi-objective control problem can be investigated and analyzed. Due to the energy loss in the circuit and energy consumption for control, optimal strategy for energy harvesting may not yield optimal vibration suppression. Model Predictive Control (MPC) where the system with constraints can be modeled into a hybrid system with logic state can be one effective method to design regenerative vibration control algorithms. In addition, the system-level controller design can be conducted in the future where the dynamics of the energy harvesting circuit, dynamics of building with TMD and the wind modeling are taken into consideration all at the same time.

## Publications Based On the Dissertations

### Journal Papers:

- [1] Xiudong Tang, Lei Zuo, Wen Cui, Jinwoo Park, Analytical solutions to  $H_2$  and  $H_\infty$  optimization of resonant shunt electromagnetic tuned mass damper and vibration energy harvester, *Journal of Sound and Vibration*, in review, 2013.
- [2] Lei Zuo and Xiudong Tang, Large-scale Vibration Energy Harvesting, *Journal of Intelligent Material Systems and Structures*, in print, 2013.
- [3] Xiudong Tang, Teng Lin and Lei Zuo, Design and Optimization of Tubular Linear Electromagnetic Vibration Energy Harvesters, the *IEEE/ASME Transactions on Mechatronics*, in print, 2013.
- [4] T-B. Xu, E. Siochi, J-H Kang, L. Zuo, W. Zhou, Xiudong Tang and X. Jiang, Energy Harvesting Using a PZT Ceramic Multilayer Stack , *Smart Materials and Structures*, accepted, 2013.
- [5] Xiudong Tang and Lei Zuo, Simultaneous Energy Harvesting and Vibration Control of Structures with Tuned Mass Damper, *Journal of Intelligent Material Systems and Structures*, 23(18), 2117-2127, 2012.
- [6] Xiudong Tang and Lei Zuo, Vibration Energy Harvesting from Random Force and Motion Excitations, *Smart Materials and Structures*, 21(7), 075025, 2012.
- [7] Xiudong Tang and Lei Zuo, Enhanced Vibration Energy Harvesting Using Dual-mass System, *Journal of Sound and Vibration*. Vol. 330, Issue 21, pp 5199-5209, 2011.

### Conference Papers:

- [1] Xiudong Tang, Wen Cui and Lei Zuo, Closed-form Optimization of Resonant Shunted Electromagnetic Tuned Mass Dampers for Vibration Control and Energy Harvesting, *ASME IDETC/CIE 2013*, in review, 2013.
- [2] Wen Cui, Xiudong Tang and Lei Zuo,  $H_2$  Optimization of Electricity-Generating Tuned Mass Dampers for Simultaneous Vibration Control and Energy Harvesting, *SPIE Conferences on Smart Structures and Materials*, San Diego, CA, 2013.



- [3] Xiudong Tang, Teng Lin and Lei Zuo, Electromagnetic Vibration Energy Harvesting with High Power Density using a Magnet Array, *Smart Structures and Materials: Proceedings of SPIE*, San Diego, California, March 2012.
- [4] Xiudong Tang, Lei Zuo, Teng Lin and Peisheng Zhang, Improved Design of Linear Electromagnetic Transducers for Large-Scale Vibration Energy Harvesting, *Smart Structures and Materials: Proceedings of SPIE*, San Diego, 2011.
- [5] Xiudong Tang and Lei Zuo, Simulation and Experiment Validation of Simultaneous Vibration Control and Energy Harvesting from Buildings via Tuned Mass Dampers (invited paper), *America Control Conference*, California, 2011.
- [6] Xiudong Tang and Lei Zuo, Enhanced Design of Vibration Energy Harvesting using Dual-Masses, *2011 ASME Design Engineering Technical Conferences*, Washington DC, Aug 28-31, 2011.
- [7] T. Xu, J. Kang , E. Siochi, L. Zuo, W. Zhou, Xiudong Tang and X Jiang, A Piezoelectric Ceramic Multilayer Stack for Energy Harvesting under Dynamic Forces, *ASME Design Engineering Technical Conferences*, Washington DC, 2011.
- [8] Xiudong Tang and Lei Zuo, Regenerative Semi-Active Control of Tall Building Vibration with Series TMDs, *Proceeding of America Control Conference*, Baltimore, MD, June 30 - July 2, 2010.
- [9] Xiudong Tang and Lei Zuo, Passive, Active and Semi-active Series Tuned Mass Dampers, *Proceedings of SPIE- Active and Passive Smart Structures and Integrated Systems*, San Diego, March 2010.
- [10] Xiudong Tang and Lei Zuo, Self-powered Active Control of Structures with TMDs, *IMAC XXVIII Conference and Exposition on Structural Dynamics: Structural Dynamics and Renewable Energy*, Jacksonville, Florida, 2010.
- [11] Xiudong Tang and Lei Zuo, Towards MESO And Macro Scale Energy Harvesting of Vibration, *Proceedings of the 2009 ASME International Mechanical Engineering Congress and Exposition*, Florida, 2009.
- [12] Lei Zuo and Xiudong Tang, Circuit Optimization and Vibration Analysis of Electromagnetic Energy Harvesting Systems, *Proceedings of the 2009 ASME Design Engineering Technical*

*Conference*, San Diego, 2009.

### **Posters and Technical Reports:**

- [1] Xiudong Tang, Teng Lin and Lei Zuo, Vibration Energy Harvester with High Power Density using a Magnet Array, *Student Poster Symposium*, Stony Brook, New York, 2012.
- [2] Xiudong Tang, Teng Lin and Lei Zuo, Design of Linear Electromagnetic Vibration Energy Harvester with High Power Density, *Student Poster Symposium*, Stony Brook, New York, 2011.
- [3] Lei Zuo, Xiudong Tang and Tao Ni, Vibration Control of Tall Buildings using Electricity-Harvesting Tuned Mass Dampers, *NSF CMMI Research and Innovation Conference*, Atlanta, GA, 2011.
- [4] Xiudong Tang and Lei Zuo, Simultaneous Energy Harvesting and Vibration Control of Civil Structures, *2011 Sigma XI Northeastern Research Symposium*, New York, 2011.
- [5] Tao Ni, Xiudong Tang, Lei Zuo, Wind Modeling and Energy Harvesting from Tall Building, *2011 Sigma XI Northeastern Research Symposium*, New York, 2011.
- [6] Xiudong Tang, Teng Lin, Zak Brindak, Peisheng Zhang and Lei Zuo, Retrofit Design of Electromagnetic Energy Harvesters for Vehicle Suspensions, *Advanced Energy Conference 2010*, New York, 2010.
- [7] Lei Zuo, Pei Sheng Zhang, Xiudong Tang, Energy Assessment of Regenerative Vehicle Suspension, *Interim Report* for New York State Energy Research and Development Authority, Albany, 2010.
- [8] Xiudong Tang, Min Chen, Zhu Jian Liu, Ethan Li, Vibration Energy Harvesting from Tall Buildings-Feasibility Study Based on a Building Prototype, *Student Poster Symposium*, Stony Brook, New York, 2010.
- [9] Xiudong Tang, Teng Lin and Lei Zuo, Towards Meso and Macro Scale Vibration Energy Harvesting, *Advanced Energy Conference 2009*, New York, 2009.

## References

- Ali, M.M. and Moon, K.S. 2007. "Structural Developments in Tall Buildings: Current Trends and Future Prospects", *Architectural Science Review*, Vol 50 n3, pp 205-223.
- Antaki, J. F., Bertocci, G. E., Green, E. C. Nadeem, A. Rintoul, T., Kormos, R. and Griffith, B.. 1995. "A gait-powered autologous battery charging system for artificial organs," *ASAIO Journal*, 41(3): M588–M595.
- Asami, T., Nishihara, O. and Baz, A.M. 2002. "Analytical Solutions to  $H_{\infty}$  and  $H_2$  Optimization of Dynamic Vibration Absorber Attached to Damped Linear Systems," *Journal of Vibration and Acoustics*, 124, pp. 67–78.
- Badel, A., Benayad, A., Lefevre, E., Lebrun, L., Richard, C., and Guyomar, D. 2006. "Single crystals and nonlinear process for outstanding vibration-powered electrical generators," *IEEE Transaction on Ultrasonics. Ferroelectrics and Frequency Control*, 53:673–84.
- Bahrain World Trade Center: World's First Building Integrated Wind Turbines Inaugurated. 2013. <http://www.bahrainwtc.com/>
- Behrens, S., Fleming, A.J., and Moheimani, S., 2003. "Electromagnetic Shunt Damping", *Proceedings of the IEEE/ASME International Conference on Advanced Intelligent Mechatronics*, pp. 1145–1150.
- Behrens, S., Fleming, A.J., and Moheimani, S., 2006. "Passive Vibration Control via Electromagnetic Shunt Damping", *IEEE/ASME Transactions*, vol.10, 1, pp.118-122.
- Bertsekas, D.P. 1995, *Nonlinear Programming*, Athena Scientific, Belmont, MA.
- Cassidy, I. L., Scruggs, J. T., and Behrens, S. 2011. "Design of electromagnetic energy harvesters for large-scale structural vibration applications," *Proc. SPIE 7977*, 79770P (2011).
- Chalasan, S., and Conrad, J. M. 2008. "A survey of energy harvesting sources for embedded systems," *Proceeding of IEEE Southeastcon*, 442-447.
- Chen, C., Islam, R. A., and Priya, S. 2006. "Electric energy generator," *IEEE transactions on ultrasonics, ferroelectrics, and frequency control*, 53(3). 656-661

- Chen, X. and Kareem, A., 2001. "Aeroelastic Analysis of Bridges under Multicorrelated Winds: Integrated State-Space Approach", *Journal of Engineering Mechanics*, Vol. 127, No. 11.
- Chey, M., Chase, J., Mander, J. and Carr, A. 2010. "Semi-active tuned mass damper building systems: Design", *Earthquake Engineering and Structural Dynamics*, Vol. 39, 2, pp. 119-139.
- Choi, S., Seong, M., and Kim, K. 2009. "Vibration control of an electrorheological fluid-based suspension system with an energy regenerative mechanism" *Journal of Automobile Engineering*, 223(4):459-469.
- CIS "Solar Tower" Case Study, 2013. <http://www.solarcentury.com/Commercial-developers/>
- Collins, L. 2006. "Harvesting for the world: energy harvesting techniques," *IEEE Power Engineer*, 20:34-37.
- Davenport, A. G. 1967. "Gust loading factor.", *ASCE Journal of Structures Division*, 93(3),11-34
- Den Hartog, J. P. 1947, "Mechanical Vibration", McGraw-Hill, New York.
- DIFC, 2013, Dubai International Financial Centre launches DIFC Lighthouse Tower, [http://www.difc.ae/press\\_centre/](http://www.difc.ae/press_centre/)
- Denoon, R., Kwok, K., Full-scale measurements of wind-induced response of an 84 m high concrete control tower, *Journal of Wind Engineering and Industrial Aerodynamics* 60 (1996) 155-165
- Donelan J.M., Li, Q., Naing, V., Hoffer, J.A., Weber, D.J., and Kuo, A.D., 2008, "Biomechanical Energy Harvesting: Generating Electricity During Walking with Minimal User Effort", *Science*: Vol. 319 no. 5864 pp. 807-810
- Dutton and Isyumov, 1990. "Reduction of Tall Building Motion by Aerodynamic Treatments", *Journal of Wind Engineering and Industrial Aerodynamics*, v: 36.
- Dwari, S., and Parsa, L. 2010. "An efficient AC–DC step-up converter for low-voltage energy harvesting," *Power Electronics*, 25(8):2188 - 2199.

- Dyke, S. J., Spencer, B. F., Sain, M. K. and Carlson, J. D. 1996, "Modeling and control of magnetorheological dampers for seismic response reduction", *Smart Mater. Struct.* 5 pp. 565-575.
- East Japan Railway Company. 2008. "Demonstration Experiment of the 'Power-Generating Floor' at Tokyo Station."
- Ebrahimi, B., Khamesee, M. B. and Golnaraghi, M.F. 2008. "Design and modeling of a magnetic shock absorber based on eddy current damping effect," *Journal of Sound and Vibration*, 315(4-5). 875-889.
- Energy Information Administration, Department of Energy, <http://tonto.eia.doe.gov/>
- Forward, R.L., 1979. "Electronic damping of vibrations in optical structures", *Applied Optics*. 18, 690-697.
- Frahm, H. 1911, "Device for Damping Vibrations of Bodies," U.S. Patent No.989, 958.
- Fujino Y., Soong, T.T. and Spencer, B. F. 1996. "Structural Control: Basic Concepts and Applications", the Proceedings of the 1996 ASCE Structures Congress
- Galhardi, M. A., Guilherme, T. H., and Junior, V. L. 2008. "A review of power harvesting from vibration using piezoelectric materials and applications," The 7th Brazilian Conference on Dynamics, Control and Applications.
- Gamble, S., Robinson, J.K., Alkhatib, R., Smith, A., Haskett, T., Burns, J, and McLean, D., 1995. "Performance-Based Design for Motion Control of a Supertall Tower", Proceedings of the 2009 Structures Congress.
- Giorgetti, N., Bemporad, A., Tseng, H.E. and Hrovat, D. 2006. Hybrid model predictive control application towards optimal semi-active suspension, *International Journal of Control*, Vol. 79, Issue 5, pp 521-533.
- Granstrom, J., Feenstra, J., Sodano, H. A., and Farinholt, K. 2007. "Energy harvesting from a backpack instrumented with piezoelectric shoulder straps," *Smart Materials and Structures*, 16:810-1820.

- Gupta, A., Jendrzejczyk, J. A., Mulcahy, T. M., and Hull, J. R. 2006. "Design of electromagnetic shock absorbers," *International Journal of Mechanics and Materials in Design*, 3(3). 285-291.
- Guyomar, D., Badel, A., Lefeuvre, E. and Richard, C., 2005, "Toward energy harvesting using active materials and conversion improvement by nonlinear processing", *IEEE transaction on ultrasonics, ferroelectrics and frequency control*, vol.52, pp.584-595.
- Hac, A. and Youn, I, Optimal Semi-Active Suspension with Preview Based on a Quarter Car Mode, *Journal of Vibration and Acoustic*. V114,pp 84-92, 1992.
- Hagood, N.W. and Flotow, A., 1991. "Damping of structural vibrations with piezoelectric materials and passive electrical networks", *Journal of Sound and Vibration*, 146, Issue 2, , pp. 243–268,.
- Haskett, T., Breukelman, B., Robinson, J., and Kottelenberg, J. 2004. "Tuned-mass damper under excessive structural excitation," Report of the Motioneering Inc., Guelph, Ontario, Canada
- Higashino, M. and Aizawa, S., "The Application of Active Mass Damper System in Actual Buildings, International Workshop on Structural Control", Honolulu, Hawaii: 82-93, 1993.
- Holmes, J. D. 2001, *Wind Loading of Structures*, Spon Press, New York.
- Housner, G.W., Bergman, L.A., Caughey, T.K., Chassiakos, A.G., Claus, R.O., Masri, S.F., Skelton, R.E., Soong, T.T., Spencer, B.F., Yao, J.T.P. 1997 "Structural Control: Past, Present, and Future, *Journal*
- Hrovat, D., Barak, P. and Rabins, M. 1983, "Semi-Active versus Passive or Active Tuned Mass Dampers for Structural Control", *Journal of Engineering Mechanics*, Vol. 109, No. 3, pp. 691-705.
- Huang, K., Yu, F. and Zhang, Y. 2011. Active controller design for an electromagnetic energy-regenerative suspension, *International Journal of Automotive Technology*, Vol. 12, No. 6, pp 877-885.

- International Organization for Standardization. 1997. "Mechanical vibration and shock—evaluation of human exposure to whole body vibration – part 1: general requirements," ISO 2631-1:1997.
- International Standard Organization, Bases for design of structures -Serviceability of buildings and walkways against vibrations, ISO 10137, 2007
- Inoue, T., Ishida, Y. and Sumi, M., 2008. "Vibration Suppression Using Electromagnetic Resonant Shunt Damper", *ASME Journal of Vibration and Acoustics*, 130, Issue 4, 041003 (8 pages).
- Irwin, P. 2008. "Wind and tall building: negatives and positives", *Struct. Design Tall Spec. Build.* 17, 915–928.
- Jolly, M. R., and Margolis, D. L. 1997. "Regenerative systems for vibration control," *Journal of Vibration and Acoustics*, 119:208–215.
- Kareem, A. 1984 "Model for Prediction of the Acrosswind Response of Buildings," *Engineering Structures* ,6(2) 136-141.
- Kareem, A. 2008. "Numerical simulation of wind effects: A probabilistic perspective." *Journal of Wind Engineering and Industrial Aerodynamics*, 96, 1472-1497.
- Kareem, A., Kijewski, T. and Tamura, Y. 1999. "Mitigation of Motions of Tall Buildings with Specific Examples of Recent Applications", *Wind and Structures*, Vol 2, n3, pp 201-251.
- Karnopp, D. 1995, "Active and Semi-Active Vibration Isolation", *Journal of Mechanical Design*, Volume 117, pp. 177-186.
- Kawamoto, Y., Suda, Y., Inoue, H., and Kondo, T. 2007. "Modeling of Electromagnetic Damper for Automobile Suspension," *Journal of System Design and Dynamics*, 1(3):524-535.
- Kawamoto, Y., Suda, Y., Inoue, H., and Kondo, T. 2008. "Electro-mechanical suspension system considering energy consumption and vehicle maneuver," *Vehicle System Dynamics*, 46:1053 -1063.

- Kerschen, G., Kowtko, J., McFarland, D. M., Bergman, L. A. and Vakakis, A. F. 2007. "Theoretical and experimental study of multimodal targeted energy transfer in a system of coupled oscillators", *Nonlinear Dynamics*, vol. 47, pp. 285-309, 2007.
- Kim, H., Kim, J.H. and Kim, J, 2011 "A review of piezoelectric energy harvesting based on vibration", *International Journal of Precision Engineering and Manufacturing*, Volume 12, Issue 6, pp 1129-1141.
- Kim, S. and Okada, Y. 2002. "Variable resistance type energy regenerative damper using pulse width modulated step-up chopper," *Journal of Vibration and Acoustics*, 124:110–115.
- Kornbluh, R. D. et al.. 2002. "Electroelastomers: applications of dielectric elastomer transducers for actuation, generation, and smart structures," *Proc. SPIE*, 4698:254–70.
- Koshika, N., Sakamoto, M., Sasaki, K., Ikeda, Y., and Kobori, T. 1992, "Control effect of active mass driver system during earthquakes and winds", Proc 1st MOVIC Conf, Yokohama, Japan.
- Kwok, K.C.S., Samali, B. 1995 "Performance of tuned mass dampers under wind loads", *Engineering Structures*, Vol. 17, No. 9, pp. 655~67.
- Lefevre, E., Audigier, D., Richard, C. and Guyomar, D., 2007. "Buck-Boost Converter for Sensorless Power Optimization of Piezoelectric Energy Harvester, *IEEE Transaction on Power Electronics*", Vol 22, n5, pp2018-2025.
- Lesieutre, G. A., 1998. "Vibration damping and control using shunted piezoelectric materials", *The Shock and Vibration Digest*, vol. 30, no3, pp. 187-195.
- Lewandowski, R. and Grazymislawska, J. 2003, "Dynamic behavior of composite mass damper for control of wind-excited vibration", AMAS Workshop on Smart Materials and Structures.
- Li, P. and Zuo, L. 2013 "Assessment of Vehicle Performances with Energy-Harvesting Shock Absorbers", SAE 2013 World Congress, April 16-18, 2013, Detroit, Michigan
- Li, Z., Zuo, L., Kuang, J. and Luhrs, G. 2012 "A motion rectifier based energy harvesting shock absorbers", 2012 ASME Design Engineering Conference, Chicago, IL, Aug 12-15.



- Mitcheson, P. D. et al.. 2004. "MEMS electrostatic micro-power generator for low frequency operation," *Sensors Actuators*, 115:523–9.
- Mirzaeifar, R., Bahai, H., and Shahab, S. 2008. "Active control of natural frequencies of FGM plates by piezoelectric sensor/actuator pairs," *Smart Material and Structure*, 17(4):045003(8pp).
- Moheimani, S.O.R., 2003. "A survey of recent innovations in vibration damping and control using shunted piezoelectric transducers", *IEEE Transactions on Control Systems Technology*, vol 11 Issue 4, pp 482 - 494.
- Morgan, T.A. and Mahin, S.A. 2006. "Development of a Design Methodology for Seismic Isolated Buildings Considering a Range of Performance Objectives", Proceedings, 4th International Conference on Earthquake Engineering, NCREE, Taipei, Taiwan
- Nakano, K., Suda, Y., and Nakadai, S. 2003. "Self-powered active vibration control using a single electric actuator," *Journal of Sound and Vibration*, 260:213–235.
- Nakano, K., and Suda, Y. 2004. "Combined type self-powered active vibration control of truck cabins," *Vehicle System Dynamics*, 41:449-473.
- NatHaz Modeling Laboratory, 2007, NatHaz On-line Wind Simulator, [http://windsim.ce.nd.edu/int\\_winsim.html](http://windsim.ce.nd.edu/int_winsim.html)
- Ni, T., Zuo, L., and Kareem, A. 2011. "Assessment of energy potential and vibration mitigation of regenerative tuned mass dampers on wind excited tall buildings" *2011 ASME Design Engineering Technical Conferences, Washing DC, VA.*
- Nishihara, O. and Asami, T. 2002. "Closed-form solutions to the exact optimization of dynamic vibration absorbers", *ASME Journal of Vibration and Acoustics*, 124, 576-582).
- Ottman, G., Bhatt, A. C., Hofmann, H. F., and Lesieutre, G. A. 2002. "Adaptive piezoelectric energy harvesting circuit for wireless remote power supply," *IEEE Trans. Power Electron*, 17:669–676.

- Ottman, G., Hofmann, H. F., and Lesieutre, G. A. 2003. "Optimized piezoelectric energy harvesting circuit using step-down converter in discontinuous conduction mode," *IEEE Trans. Power Electron.* 18:696–703.
- Palomera-Arias, R. 2005. "Passive electromagnetic damping device for motion control of building structures," Ph. D. Thesis, Massachusetts Institute of Technology, Cambridge, MA.
- Paradiso, J., and Starner, T. 2005. "Energy scavenging for mobile and wireless electronics," *IEEE Pervasive Computing*, 4:18-26.
- Park, G., Rosing, T., Todd, M. D., Farrar, C. R., and Hodgkiss, W. 2008. "Energy harvesting for structural health monitoring sensor networks," *ASCE Journal of Infrastructure Systems*, 14:64-79.
- Pinkaew, T. and Fujino, Y. 2001, "Effectiveness of semi-active tuned mass dampers under harmonic excitation", *Engineering Structures*, Volume 23, Issue 7, pp. 850-856.
- Rasmussen, E., "Dampers Hold Sway", *Civil Engineering—ASCE*, Vol. 67, No. 3, March 1997, pp. 40-43
- Rani, S. 2005. "Bose breakthrough: electromagnetic auto suspension," *Siliconeer*.
- RERL Wind Data, University of Massachusetts Renewable Energy Research Laboratory, [http://www.ceere.org/rerl/publications/resource\\_data/index.html](http://www.ceere.org/rerl/publications/resource_data/index.html)
- Rome, L. C., Flynn, L., Goldman, E. M., and Yoo, T. D. 2005. "Generating electricity while walking with loads," *Science*, 309:1725–1728.
- Saadon, S., and Sidek, O., 2011, "A review of vibration-based MEMS piezoelectric energy harvesters", *Energy Conversion and Management*, Volume 52, Issue 1, January 2011, Pages 500-504
- Samali, B., Kwok, K. C. S., Wood, G.S. and Yang, J.N., 2004. "Wind Tunnel Tests for Wind-Excited Benchmark Building", *Journal of Engineering Mechanics*, Vol. 130, No.4.
- Savaresi, S.M., Poussot-Vassal, C., Spelta, C. and Sename, O. 2010. Semi-active suspension control design for vehicles.
- Schwartz, T.A. 2001. "When Bad Things Happen to Good Buildings", *Architecture Week*.

- Scott, R. 2001. "In the Wake of Tacoma: Suspension Bridges and the Quest for Aerodynamic Stability", ASCE Press.
- Scruggs, J. T. 1999a. "Active, regenerative control of civil structure," Master Thesis, Virginia Polytechnic Institute and State University, Blacksburg, VA.
- Scruggs, J., and Linder, D. K. 1999b. "Active energy control in civil structures," *Proc. SPIE*, Newport Beach, CA.
- Scruggs, J. T. 2004. "Structure control using regenerative force actuation networks," Ph. D. Thesis, California Institute of Technology, Pasadena, CA.
- Scruggs, J. T. 2007. "Multi-Objective Optimization of Regenerative Damping in Vibrating Structures." *Proceedings of the 27th American Control Conference*, New York, NY, July 2007.
- Scruggs, J. T. 2010. "Multi-Objective Nonlinear Control of Semiactive and Regenerative Systems." *Proceedings of the 30th American Control Conference*, June, 2010.
- Scruggs, J.T., Cassidy, I.L., and Behrens S. 2012, "Multi-Objective Optimal Control of Vibratory Energy Harvesting Systems." *Journal of Intelligent Material Systems and Structures*. Accepted.
- Setareh, M., Ritchey, JK, Baxter, AJ. and Murray, TM. 2006. "Pendulum tuned mass dampers for floor vibration control". *J Perf Constr Fac* 20(1): 64–73, 2006
- Shenck, N., and Paradiso, J. 2001. "Energy scavenging with shoe-mounted piezoelectrics," *IEEE Micro*, 21(3):30–42.
- Snowdon, J. 1974 "Dynamic Vibration Absorbers That Have Increased Effectiveness," *ASME J. Eng. Ind.*, 96, pp. 940–945.
- Sodano, H. A., and Inman, D. J. 2004. "A review of power harvesting from vibration using piezoelectric materials," *The Shock and Vibration Digest*, 36:197–205.
- Soong, T.T. and Spencer, B.F. 2002. "Supplemental energy dissipation: state-of-the-art and state-of-the practice, *Engineering Structures*", vol 24, pp 243–259.

- Spencer, B.F. and Sain, M.K. 1997 “Controlling buildings: a new frontier in feedback, IEEE Control Systems Magazine”, Vol. 17, No. 6, pp. 19–35.
- Starner, T., and Paradiso, J. 2004. “Human generated power for mobile electronics,” *Low Power Electronics Design*, 45:1-35.
- Stephen, N.G. 2006. “On energy harvesting from ambient vibration,” *Journal of Sound and Vibration*, vol. 293, pp. 409-425.
- Suda, Y., Suematsu, K., Nakano, K., and Shiiba, T. 2000. “Study on electromagnetic suspension for automobiles simulation and experiments of performance,” *Proc. of the 5th International Symposium on Advanced, Vehicle Control*, 699–704.
- Suda, Y., Shiiba, T., Hio, K., Kawamoto, Y., Kondo, T., and Yamagata, H. 2004. “Study on electromagnetic damper for automobiles with nonlinear damping force characteristics road test and theoretical analysis,” *Proc. of the 18th IAVSD Symposium, Veh. Syst. Dyn. Suppl.*, 41:637–646.
- Sun, J.Q., Jolly, M.R. and Norris, M.A. 1995. “Passive, Adaptive and Active Tuned Vibration Absorbers—A Survey”, *Journal of Vibration and Acoustics*, Vol 117, Issue B, pp 234-243.
- Symans, M.D., Charney, F.A., Whittaker, A.S., Constantiou, M.C., Kircher, C.A., Johnson, M.W. and McNamara, R.J. 2008 “Energy Dissipation Systems for Seismic Applications: Current Practice and Recent Development”, *Journal of Structural Engineering*, 134(1), pp. 3-21.
- Tanaka, T., Yamamoto, M., Katayama, T., Nakahira, K., Yamane, K., Shimano, Y., Hirayama, K. 2003. “Recent Applications of Structural Control Systems to High-Rise Buildings, Earthquake Engineering and Engineering Seismology”, Vol. 4, No. 1, pp 75-93.
- Xiudong Tang, Teng Lin and Lei Zuo, Design and Optimization of Tubular Linear Electromagnetic Vibration Energy Harvesters, the *IEEE/ASME Transactions on Mechatronics*, in print, 2013.
- Tang, X. and Zuo, L., 2009. “Towards MESO and Macro scale energy harvesting of vibration”, Proceedings of the 2009 ASME International Mechanical Engineering Congress and Exposition, Florida.

- Tang, X. and Zuo, L. 2010a, “Regenerative semi-active control of tall building vibration with series TMDs”, American Control Conference (ACC2010), Baltimore, MD, USA.
- Tang, X. and Zuo, L. 2010b, “Self-powered active control of structures with TMDs”, IMAC XXVIII Conference and Exposition on Structural Dynamics: Structural Dynamics and Renewable Energy, Jacksonville, Florida, Feb 1-4.
- Tang, X., and Zuo, L. 2011a. “Simulation and experiment validation of simultaneous vibration control and energy harvesting from buildings via tuned mass dampers,” *Proceeding of America Control Conference*, San Francisco, CA.
- Tang, X., and Zuo, L. 2011b, “Enhanced Vibration Energy Harvesting using Dual-Mass Systems”, *Journal of Sound and Vibration*, Vol 330, pp5199–5209.
- Tang, X. and Zuo L., 2012. “Vibration Energy Harvesting from Random Force and Motion Excitations”, *Smart Material and Structures*, Vol. 21, 7, pp075025.
- Taylor, D.P., “History, design and applications of fluid dampers in structural engineering”, Taylor device Inc.
- Tomoo, S. and Keiji, S.. (1998), “Dynamic Characteristics of a Triangular-Plan High-Rise Building and Its Active Vibration Control System”, Proceedings of Structural Engineers World Congress, San Francisco, CD-ROM: T198-5.
- Tschanz, T. and Davenport, A.G. 1983. “The Base Balance Technique for the Determination of Dynamic Wind Loads”, *Journal of Wind Engineering and Industrial Aerodynamics*, 13 (1983) 429-439.
- Wang, J.J., Penamalli, G.P. and Zuo, L. 2012. “Electromagnetic energy harvesting from train induced railway track vibrations”, IEEE/ASME International Conference on Mechatronics and Embedded Systems and Applications (MESA), pp.39-34.
- Yamaguchi, H. and Hampornchai, N. 1993 “Fundamental Characteristics of Multiple Tuned Mass Dampers for Suppressing Harmonically Forced Oscillations,” *Earthquake Eng. Struct. Dyn.*, 22, pp. 51–62.

- Zheng, X., Yu, F., and Zhang, Y. 2008. "A novel energy-regenerative active suspension for vehicles," *Journal of Shanghai Jiaotong University (Science)*, 13(2):184-188.
- Zhou, K., Doyle, J. C. and Glover, K., 1995. "Robust and Optimal Control", Prentice-Hall, Englewood Cliffs, NJ, 1995.
- Zhou, Y. and Kareem, A. 2001 "Gust Loading Factor: A New Model," *Journal of Structural Engineering*, ASCE, Vol. 127, No. 2, 2001, pp. 168-175.
- Zhou, Y., Kijewski, T. and Kareem, A. 2002, "Along-wind Load Effects on Tall Buildings: Comparative Study of Major International Codes and Standards", *Structural Engineering*, Vol.128, No. 6, June 1.
- Zuo, L. and Nayfeh, S. 2002. "Design of Multi-Degree-of-Freedom Tuned-Mass Dampers: A Minimax Approach," *Structural Dynamics, and Materials Conference*, AIAA Paper No.2002-1283.
- Zuo, L. and Tang, X., 2009. "Circuit optimization and vibration analysis of electromagnetic energy harvesting systems", *Proceedings of the 2009 ASME Design Engineering Technical Conference*, San Diago.
- Zuo, L. 2009. "Effective and Robust Vibration Control Using Series Multiple Tuned-Mass Dampers," *Journal of Vibration and Acoustics*, Volume 131, Issue 3.
- Zuo, L., Scully, B., Shestani, J., and Zhou, Y. 2011. "Design and characterization of an electromagnetic energy harvester for vehicle suspensions," *Smart Materials and Structures*, 19(4).
- Zuo, L., Chen, X. and Nayfeh, S. 2011. "A new type of eddy current damper with increased energy density". *Journal of Vibration and Acoustics*.133.
- Zuo, L. and Cui, W. 2012. "Dual functional energy harvesting and vibration control: An electromagnetic realization of series tuned mass dampers", *ASME Journal of Vibration and Acoustics*, accepted.

Zuo, L., Tang, X. and Zhang, P. 2010, "Regenerative shock absorber", U.S. and international provisional patent application # 61/368.846, filed on July 29, 2010.